Characterization of Li doped, magnetron sputtered Cu$_2$O thin films.

Kjetil Karlsen

Thesis submitted for the degree of
Master in Materials Science and Nanotechnology
60 credits

Department of Chemistry
Faculty of mathematics and natural sciences

UNIVERSITY OF OSLO

Spring 2019

Characterization of Li doped, magnetron sputtered Cu_2O thin films.

Kjetil Karlsen

UNIVERSITAS OSLOENSIS
MDCCCXI

Characterization of Li doped, magnetron sputtered Cu_2O thin films.

http://www.duo.uio.no/

Printed: Reprosentralen, University of Oslo

Abstract

Cuprous oxide (Cu_2O) is a natural p-type semiconductor with high absorption and a direct bandgap of 2.1 eV. Abundance of Cu, non-toxicity and low costs, in conjunction with a theoretical solar cell conversion efficiency of ~ 20% for a single junction solar cell, makes it an attractive candidate for next generation tandem solar cells. Investigation of electrically active defects and impurities is essential to improve the electronic properties of the material and enabling high efficient Cu_2O based solar cells.

The effect of Li doping in magnetron sputtered Cu_2O thin films has been investigated by electrical and structural characterization methods. Both metallic Cu and ceramic Cu_2O targets for sample manufacturing were utilized. Lithium concentrations between $10^{18} - 10^{21}$ cm^{-3} were achieved, introduced by co-sputtering with Li doped Cu targets. Rectifying junctions for samples deposited on n-Si substrates were realized, with ideality factors <2.1 and current rectification up to 5.8 orders of magnitude between -1:1 V. Li doping was found to have no effect on neither IV and CV results, while thermal admittance capacitance (TAS) revealed a shallow state at $E_v + 100 \pm 30$ meV and capture cross section of between $10^{-17} - 10^{-16}$ cm^2 in most samples. It is presumed to be attributed to nitrogen situated on an oxygen site. This state is also identified by temperature dependent hall (TDH) measurements for samples with [Li]$\geq$ 10^{20} cm^{-3}. Hall measurements additionally show a decrease in hole concentration when a Li doping of ~ 10^{18} cm^{-2} is introduced. Further doping results in an increase of carrier concentration, speculated to be related to reduction in compensating donor concentrations. TDH also indicate an acceptor state between $E_v + 200$ and $E_v + 300$ in all samples. TAS measurement show a decrease in both activation energy and capture cross section for measurements obtained four months after the initial results. It is speculated that hydrogen, behaving as an amphoteric impurity in Cu_2O, can play an important role in the electronic properties of the material.

Acknowledgments

I would like to thank my supervisor Prof. Eduard Monakhov for many discussions and, despite a busy schedule, always having an open door. Throughout the thesis you have patiently helped me focus on the basics, despite my attempts at making things overly complicated. My second supervisor Kristin Bergum has provided invaluable experimental inputs and good discussions, for which I am very grateful. While Kristin Bergum were on maternity leave, Heine Nygard Riise stepped in and helped with discussions. I am especially grateful to my day-to-day supervisor Martin Nyborg for including me in his project. Not only has he spent weeks optimizing most of the samples used in this thesis and providing training on several techniques, but also been available for countless discussions.

Dr. Alexander Azarov and Christoph Seiffert has performed SIMS measurements. Ilia Kolevatov has in addition to the necessary training to work in the E-lab, been a great help in analyzing, proof reading and understanding the theory of TAS. I am also very thankful to *MiNaLab* and its staff, which has provided instruments and technical knowhow for this thesis. The help of Viktor Bobal and Christoff Seiffert in particular has been invaluable, quickly fixing issues with the instruments.

The staff and students at the *Light and Emitting Novel Semiconductor* group has helped create a fun and stimulating work environment, especially my fellow master students. A special thanks to Fredrik Stulen for his friendship and table tennis enthusiasm and Vilde Mari Reinertsen for deep conversations and having an excellent listening ear for both frustrations and victories. Finally I would express my deepest gratitude to my family for all the support, encouragements, challenges and love you have given me all my life.

Contents

1 Introduction

The goals set by the 2015 Paris agreement requires a near zero CO_2 emission from power generation by 2050 and a shift towards electricity as the main energy carrier [1]. In 2017 solar power accounted for 38% of the net new power capacity [2] and total installed photovoltaic (PV) capacity in the world increased over 4300 % between 2007 and 2017 [3]. Electricity generated from PV plants is already the cheapest source of energy in many markets, but Bloomberg New Energy Finance expects a further 71% reduction in costs. Simultaneously, $8.4 trillion of investments in wind and solar power are expected between 2018 and 2050 [4].

Silicon based solar cells are the dominating PV technology on the market today, accounting for about 95% of the 2017 market [5]. Currently the record for conversion efficiency is 26.1% [6], out of a theoretical limit of 32%. However, silicon production is both capital and energy intensive, especially for high efficiency cells. Technologies aimed at increasing the efficiency and reducing costs of PVs at a global scale should be highly reliable and scalable, together with effective use of non-toxic materials in order to be sustainable at a large scale.

Thin film solar cells is potentially a more cost effective technology, due to its significantly lower material consumption. The current leaders in this segment is cadmium telluride (CdTe) and copper indium gallium selenide (CIGS) solar cells with an demonstrated efficiency of 21.5% and 21.7% respectively. Neither of these technologies are sustainable at a large scale, as they rely on toxic and scarce materials. Perovskite solar cells have seen a rapid growth in efficiency over the last years. Recently a perovskite tandem solar cell with silicon as a bottom cell achieved 28% efficiency [7]. However, poor stability and lifetime amount to a major barrier which currently prevent widespread commercialization [8].

A promising material for solar cell applications is cuprous oxide, Cu_2O. It is an abundant, non-toxic and low cost semiconductor, showing natural p-type conductivity and high absorption [9], [10]. A direct bandgap of 2.1 eV makes it a promising candidate for a tandem solar cell with silicon [11], with a theoretical efficiency above 40% [12]. In recent years the reported efficiencies of Cu_2O-based hetereojunction solar cells has increase from 2% [13] to 8.1% [14]. The record efficiencies were obtained on thermal oxidized copper sheets in oxygen ambient, a technique not suitable for thin film production. Alternatively, electrodeposition and magnetron sputtering have been employed to produce thin films, albeit with poorer conductive properties and lower efficiencies [11]. Efficiencies higher than 1% are difficult to achieve for thin film Cu_2O based solar cells, with a record of 4% [15].

The natural p-type conductivity is believed to originate from copper vacancies [16], [17]. Typically, the high efficiency thermal oxidized Cu_2O solar cells sheets have a hole concentration of $10^{13} - 10^{14}\ cm^{-3}$ [18], while thin film Cu_2O generally has hole concentrations around $10^{15}\ cm^{-3}$. Controlling defects and carrier concentrations in Cu_2O thin films is therefore of paramount importance to achieve an efficient tandem solar cell. A theoretical study from 2013 suggest that doping with alkali and alkaline earth metals could suppress the formation of copper vacancies, pointing to Li as the metal with highest potential to reduce hole concentration [19].

2 Theory

2.1 Crystal structure

This section is based on Streetman [20] and Tilley [21]. Solids are made up of atoms and/or molecules held together by strong bonds, such as covalent, ionic or metal bonds. If the atoms are arranged in a periodic manner, the solid is classified as a crystalline material. These materials are either a single crystal or polycrystalline, which contains several regions of individual single crystals. The structure of a material is important in order to predict and understand material parameters.

In order to describe a crystal structure, both a lattice describing the possible atomic coordinates and a set of every non-equivalent atom called the basis is required. Mathematically, all lattice points can be described with a set of linearly independent basis vectors $\mathbf{a}$, $\mathbf{b}$, $\mathbf{c}$ with an arbitrary lattice point as origin by:

$$\mathbf{P}(u,v,w) = u\mathbf{a} + v\mathbf{b} + w\mathbf{c} \tag{2.1}$$

where u, v, w are integers. The smallest possible volume spanned by the basis vectors describing the geometry of the crystal is the primitive unit cell. However, the structure is often described by slightly larger conventional unit cell which may be easier to visualize. There exist only seven different primitive unit cell geometries spanned by $\mathbf{P}$, but including different placement of atoms within the conventional unit cell gives rise to a total of 14 different Bravais lattices. Some structures, like Cu_2O can be described by two different unit cells, based on either Cu or O. A more comprehensive method of describing structural symmetry is with space groups. This combines the symmetry of all atoms in the unit cell with the lattice symmetry, resulting in 230 different patterns.

A consequence of the periodicity of the crystal structure is the appearance of different crystal planes. These are described by the Miller indices *h,k,l*, which defines a specific set of parallel planes (hkl). The point where these planes intercepts the basis vectors of the unit cell is used to determine the value of (hkl), by taking the reciprocal value of this point. The plane (120) intercepts for instance at $1\mathbf{a}$, $\frac{1}{2}\mathbf{b}$ and $\mathbf{c}$ at infinity $\frac{1}{\infty} = 0$, expressing that the plane is parallel to $\mathbf{c}$.

2.2 Crystal defects

Although the perfect structure is useful for classifying and describing idealized structures it does not adequately describe the physics and chemistry of real materials. Structural defects and impurities strongly affects both electronic and structural properties. Intentionally introduced impurities in semiconductors are crucial for controlling the electronic properties, which will be discussed in section 2.3. For the following discussion an ionic structure will be assumed. Tilley [21] and Nordby [22] has provided the foundation for this section.

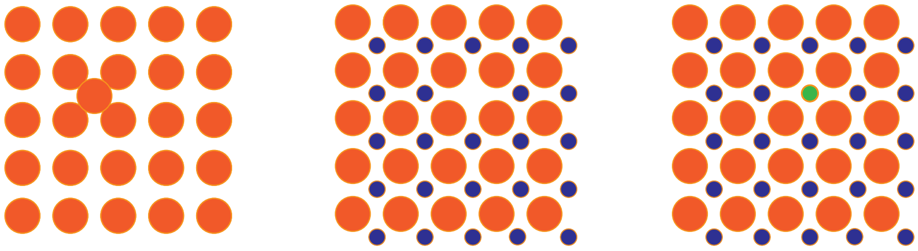

(a) Self interstitial. (b) M vacancy. (c) Metal substitutional.

Figure 2.2.1: Illustration of point defects, in both an elemental (a) and binary MO structure (b,c).

In order to classify defects it is common to divide them into four groups based on the dimensionality of their spatial distribution. The smallest defects are related to a single point in the lattice, commonly called a point defect. The other groups of defects are larger and occupy space in either 1D, 2D or 3D, often made up by an aggregation of point defects. The void left in the structure when an atom is vacant from its lattice position, is called a vacancy. However, if an atom occupy a position in the structure which is normally empty, it is termed an interstitial. In order to describe different vacancies, the Kröger Vink notation is widely used. The defect identity is stated in normal letters, while the structural position is referenced in the subscript and charge in the superscript. For instance, the substitutional and neutral defect N located on a position originally assigned to M in figure 2.2.1c is named N_M^x, while the neutral self interstitial of figure 2.2.1a is E_i^x.

2.2.1 Intrinsic defects

The purely theoretical construct of an intrinsic crystal is not exempt from defects. The concentration of native defects like self-interstitals and vacancies are governed by the minimization of Gibbs free energy at a given temperature:

$$\Delta G = \Delta H - T\Delta S \tag{2.2}$$

Structures free from defects are thus impossible at any T>0K. A defect represents an increased entropy S, which is only balanced at equilibrium by the enthalpy H .

Some defects are easy to ionize and will attain effective charge. However, at equilibrium other defects need to be present to achieve charge neutrality. An effective charge is created when the charge of a defect differs from the charge of the ion originally occupying the lattice position. In the case of an effective charge of -2 on the vacancy in 2.2.1b this $v_M^{//}$ defect could be neutralized by an equal concentration of positively effective charged oxygen defects $v_O^{\cdot\cdot}$, creating a Schottky defect. Alternatively, $v_M^{//}$ could be balanced by an interstitial $M_i^{\cdot\cdot}$, which constitutes a Frenkel defect pair.

2.2.2 Extrinsic defects

In real materials, foreign atoms will always be present. An extrinsic defect can occupy an interstitial lattice position. On the other hand, if it occupies a lattice point intended for a host atom, a substitutional defect is created as shown in figure 2.2.1c. These impurities can obtain an effective charge if it has a different valence than the host atom. Keeping the requirement of charge neutrality in mind, extrinsic impurities can therefore enhance concentrations of charged intrinsic defects. Although several charged defects can neutralize this impurity, typically only the most stable defect at a given temperature and atmosphere will dominate.

A common method of controlling the electrical properties in semiconductors is to intentionally introduce defects, a phenomena called doping. These defects are easily ionized and compensated by the excitation of electrons or holes. Whether a given impurity is behaving as a donor or acceptor is determined by the physics of the host material. Interestingly, Hydrogen has been shown to be amphoteric in certain structures, ionizing both as an donor and acceptor depending on the carrier concentrations in the material.

2.2.3 Nonstochiometric defects

In a nonstochiometric material at least one species is either in deficit or excess, which effects the defect chemistry of the structure. In order to obtain charge balance in the case of charged defects, electronic defects play an important role. If the predominant defect is a metal vacancy, as is believed to be the case for Cu_2O, holes can act as a charge balance of the acceptor metal vacancy according to the following chemical equation:

$$\frac{1}{2}\mathrm{O}_2 = O_O^X + v_{Cu}^{/} + h^{\cdot} \tag{2.3}$$

2.3 Semiconductor physics

Semiconductor physics is the study of semi-insulating materials, providing the foundation for many technologies. Throughout this discussion a periodic, ideal structure will be assumed unless otherwise stated. This review is based on Streetman [20], Kittel [23], Smets et.al [24] and Nelson [25].

2.3.1 Energy Bands

One of the basic postulations of quantum physics, The Pauli exclusion principle, states that two electrons can not occupy the same quantum mechanical state. Two orbitals are consequently forbidden from overlapping, resulting in the formation of new orbitals when atoms combine to form molecules. These orbitals are also energetically degenerate. As solids consists of a plethora of tightly packed atoms, the density of states can on the other hand be very high in certain energy intervals. These semi-continuous energy intervals are called bands, allowing for fast transport of carriers. On the other hand, there also exist regions with no states, which are forbidden for electrons to occupy.

In order to investigate the electronic properties of solids, it is necessary to solve the Schrödinger equation with an appropriate potential. A common assumption is to assume an infinite and perfect crystal, which can only be described by a periodic potential. The Bloch theorem states that the eigenfunctions of the Scrhödinger equation with this potential must be a product of (i) a simple plane wave on the form $\exp(i\mathbf{k}\cdot\mathbf{r})$ and (ii) a periodic function $u_k(\mathbf{r})$:

$$\psi_k(\mathbf{r}) = u_k(\mathbf{r})\exp(i\mathbf{k}\cdot\mathbf{r}) \tag{2.4}$$

where $u_k(\mathbf{r}) = u_k(\mathbf{r}+\mathbf{T})$ and $\mathbf{T}$ is the lattice translation vector. The wave vector is proportional to the crystal momentum of the electron and describes its energy. Associated to $\psi_k(\mathbf{r})$ are the discrete eigenvalues $E_n(\mathbf{k})$, describing the energy for a band with index n=1,2,3... A mapping of the dispersion relation $E_n(\mathbf{k})$ results in a band diagram as in figure 2.3.1, showing an overview of the different states available in the reciprocal **k**-space.

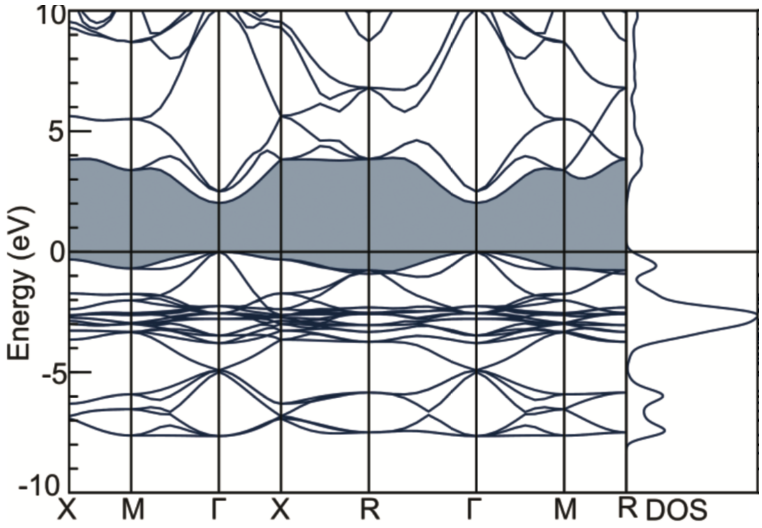

Figure 2.3.1: $E(k)$ of Cu$_2$O from *ab inito* calculations using Density Functional Theory (DFT) with the HSE06 hybrid functional [26].

The number of valence electrons per atom in the unit cell determines the degree to which the band is filled. Of particular interest are the highest occupied and lowest unoccupied bands, named the valence (VB) and conduction band (CB). If spin is considered, each cell contribute two values of **k** per band index n, giving a total of 2N possible states per $E_n(\mathbf{k})$. The valence band will be half filled in the case of 1 valence electron per atom per unit cell, while 2 valence electrons results in a filled valence band. It the valence band is partially filled or overlaps with the conduction band, as is characteristic for metals, the high density of states results in negligible excitation energy from a bound to free state. This results in turn to high conductivity of electrons and heat . Isolators and semiconductors are on the other hand characterized by a filled valence band seperated from the conduction band by a considerable energy gap E_G.

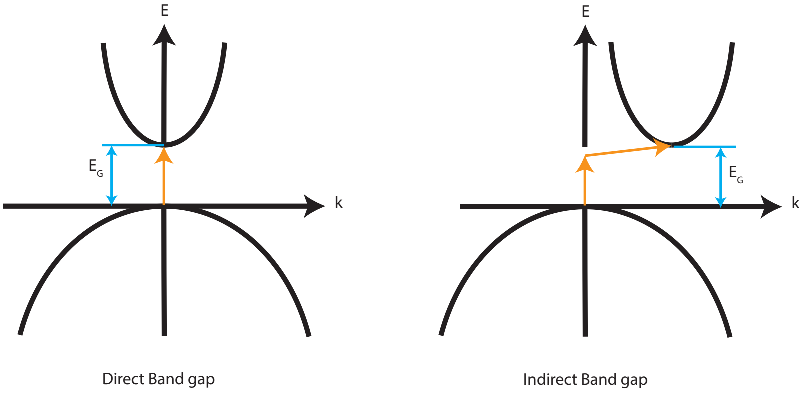

Figure 2.3.2: Illustration of direct and indirect band to band transitions. A trap state located within the indirect bandgap can assist, making the excitation a two-step process.

Figure 2.3.2 shows two different types of band to band transistions: direct and indirect. If the minimum and maximum of two bands appear for the same value of k, the band gap is said to be direct. This is not the case for indirect band gaps. During a direct absorption process of a photon with energy higher or equal to E_G, the photon wave vector $\mathbf{k}_{photon}$ is sufficient to excite an electron from VB to CB. For the case of indirect band to band transition an additional requirement of momentum change is demanded by conservation laws. At sufficiently high temperatures, this additional momentum can be delivered from phonons so that $\Delta p = \hbar(\mathbf{k}_{photon} - \mathbf{k}_{phonon})$. A direct band gap material will thus generally show higher optical absorption coefficients than indirect band gaps. However, several band gaps with different energies and k-values exists in any material Hence it is possible to have both indirect and direct transitions in the same material. .

Apart from the constraints from the periodic potential, the excited electrons behave as free electrons. Efficient masses are useful to provide for a more intuitive understanding of the physics behind the charge carriers, including information about the interactions with the periodic lattice potential. The effective mass for an electron or hole can be shown to depend on the curvature of $E(\mathbf{k})$:

$$m^* = \frac{\hbar^2}{d^2E/d\mathbf{k}^2} \tag{2.5}$$

The fermi energy ϵ_F describes the energy of the highest occupied state at absolute zero, relative to the vacuum level.

2.3.2 Charge carriers

In a semiconductor, any electron in the valence band is strongly bound to the host atom and does not respond to any external electric field. Electrons excited to the conduction band are on the other hand mobile. As the electron is excited, it creates an unoccupied and positively charged state in the VB called a hole. As holes are located in the valence bands, their effective masses are negative. For simplicity, holes are commonly viewed as a quasi-particle with positive charge and positive effective mass. As the process of exciting an electron from VB creates an electron-hole-pair (EHP), the concentration of free electrons (n) and holes (p) in an intrinsic semiconductor must be equal, $n_i = n = p$.

By doping materials, this balance equality is no longer true. An acceptor dopant has fewer valence electrons than the host atom and will introduce a vacant state at energy E_a in the bandgap, close to the VB maximum. The difference between E_a and the valence band maximum, E_v, is so small that thermal energy at room temperature is enough to excite electrons from the valence band to the acceptor states. This results in a negatively ionized acceptor atom and a free hole in the valence band. Similarly, donors will excite electrons to the conduction band.

At 0K, all electrons are bound in the valence band. The energy of the highest occupied state is designated the name Fermi energy ϵ_f, a construct which is valid at $T = 0K$. At $T > 0K$ electrons are no longer exclusively in the valence band and are distributed over several energies. Hence a statistical tool that considers the wave nature of electrons and the Pauli exclusion principle are required to describe the distribution of electrons. *Ferm-Dirac* statistics incorporates this and describes the probability an available state with energy E has of being occupied by an electron at thermal equilibrium:

$$f(E) = \frac{1}{1 + \exp(E - E_F/kT)} \tag{2.6}$$

where k is the Boltzmann constant and T is temperature. E_F is the chemical potential of electrons, commonly called the Fermi level. It represent an imaginary state where the probability of occupation is exactly $\frac{1}{2}$ and must not be confused with the Fermi energy. The probability that a state is unoccupied, which is the case when holes are considered, is $1-f(E)$. As temperature increases, the distribution of energy for electrons widens, which can be seen in figure 2.3.3. In the case $E - E_F >> kT$ equation 2.6 predicts a low probability of occupancy at E. This in turn reduces the influence the Pauli exclusion principle has on the electrons occupying the energy E and equation 2.6 can be simplified to Boltzmann statistics,

$$f(E) \simeq \exp(-(E - E_F/kT)) \tag{2.7}$$

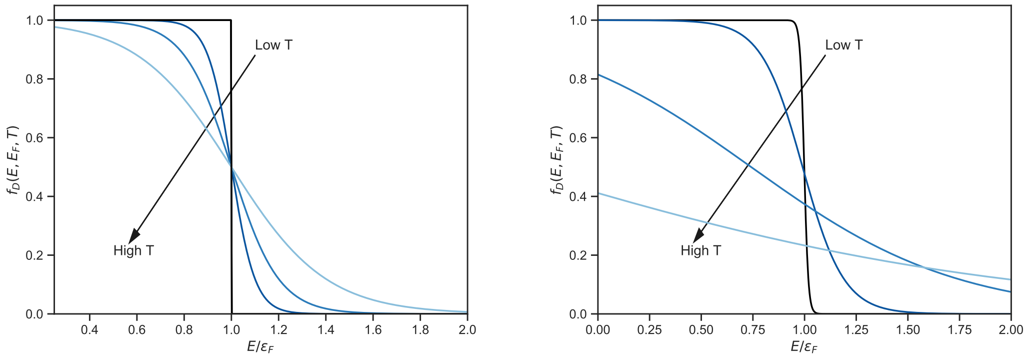

(a) Temperature independent E_F (b) Temperature dependent E_F

Figure 2.3.3: $f(E)$ at varying temperature. Generally E_F is a function of T. However, the temperatures necessary for a significant effect on $f(E)$ are in the range of 10^4K, which is true for the two highest temperatures in figure (b).

By taking into account the variable density of state at each energy, carrier concentrations can be found by integrate relevant energies:

$$n = \int_{E_c}^{\infty} f(E)N(E)dE \tag{2.8}$$

$$p = \int_{0}^{E_v} [1 - f(E)]N(E)dE \tag{2.9}$$

where $N(E)dE$ describes the DOS in the energy range dE. At room temperature the approximation $E - E_F >> kT$ is valid for moderate doping concentrations, allowing fermi-dirac statistics to be substituted by the simpler Bolzmann statistics. Further simplification of equations 2.8 and 2.9 is possible by introducing an effective DOS located at the respective band edges, N_c and N_v.

$$n \simeq N_c f(E_c) \simeq N_c e^{-(E_c - E_F)/kT} \tag{2.10}$$

$$p \simeq N_v[1 - f(E_v)] \simeq N_v e^{(E_v - E_F)/kT} \tag{2.11}$$

For the intrinsic case, the product of carrier concentrations must be a constant at a given temperature as $n = p$, $np = n_i^2$. However, this product is independent of E_F and thus valid for extrinsic semiconductors as well:

$$np = N_c e^{-(E_c - E_F)/kT} N_v e^{(E_v - E_F)/kT} = N_c N_v e^{(E_v - E_c)/kT} = N_c N_v e^{-E_G/kT} = n_i^2 \tag{2.12}$$

Temperature dependency

Many electrical parameters of semiconductors are strongly temperature dependent. The effective DOS in equations 2.10 and 2.11 is proportional to temperature and effective mass $N \propto (m^*_{eff}T)^{3/2}$. However, the temperature dependency in the exponent in equations 2.10 and 2.11 dominates at higher temperatures. This temperature dependency also affects the conductivity of a semiconductor,

$$\sigma = q\left(\mu_n n + \mu_p p\right) \tag{2.13}$$

where q is the elementary charge and the carrier mobility μ is a material parameter given describing the average drift velocity per unit electric field. Mobility is also temperature dependent, being limited by impurity scattering at low temperatures ($\mu \propto T^{3/2}$) and phonon scattering at higher temperatures ($\mu \propto T^{-3/2}$).

2.3.3 Deep states

Deep states in the band gap can severely affect carrier behavior of semiconductors. As previously mentioned, dopants typically have low ionization energies in close proximity to a band edge. However, not all impurity or defect states in the band gap are close enough to a band edge to be completely ionized by thermal energy and are often referred to as deep states. These states might originate from charged impurities, lattice defects or interface states at a material interface.

Carrier interaction with deep states can increase recombination and negatively effect carrier transport, either by trapping or by acting as a recombination center. Trapping of carriers occur when a carrier is captured and retained by the state, while recombination requires trapping of both electrons and holes. In the following discussion, deep states will be referred to as traps and are characterized by a characteristic carrier emission rate e, capture cross section σ and energy level E_t. This review is based on the textbook of Blood and Orton [27].

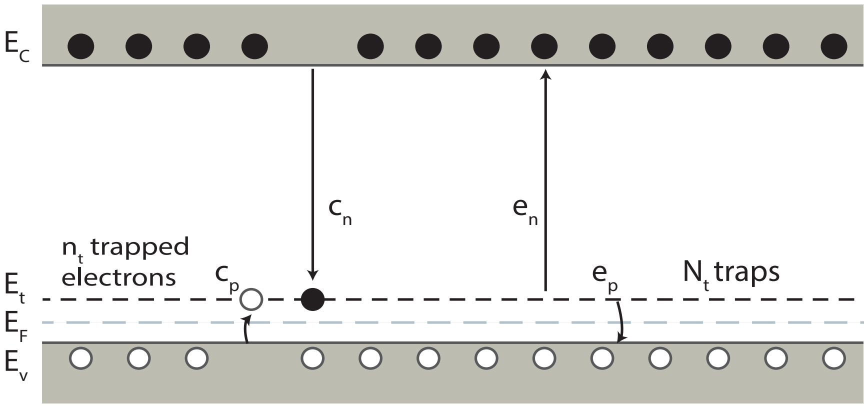

Figure 2.3.4: Illustration of mechanisms for carrier-trap interaction in a p-type semiconductor. Inspired by figure 7.1 in Blood and Orton [27].

Carrier-trap interaction

Figure 2.3.4 illustrates the four different mechanisms of trap interaction with charge carriers: emission and capture of holes and electrons. At any given moment, n_t electrons occupy the N_t available trap states. From the n_t occupied states electrons are emitted and holes captured. The remaining $N_t - n_t$ states are free to capture electrons and emit holes. Therefore, the net rate of change of electron occupancy in the trap is given by:

$$\frac{\mathrm{d}n_t}{\mathrm{d}t} = (c_n + e_p)(N_t - n_t) - (e_n + c_p)n_t \tag{2.14}$$

where $c_{n/p}$ and $e_{n/p}$ are the thermally stimulated capture and emission rates for electrons and holes. At thermal equilibrium must the process obey the principle of detailed balance, not only the steady state requirement $\frac{\mathrm{d}n_t}{\mathrm{d}t} = 0$. Detailed balance states that the rate of a process and its counterpart, i.e. $e_{p/n}$ and $c_{p/n}$, must be equal. If this limitation is not satisfied, a build up of charge could occur in either

CB or VB due to a steady state transfer. The thermal equilibrium concentration $\hat{n}_t$ is through detailed balance simplified from equation 2.14 to

$$e_n \hat{n}_t = c_n (N_t - \hat{n}_t) \tag{2.15}$$

$$c_p \hat{n}_t = e_p (N_t - \hat{n}_t) \tag{2.16}$$

with a thermal equilibrium occupancy of

$$\frac{\hat{n}_t}{N_t} = \frac{c_n}{c_n + e_n} = \frac{e_p}{e_p + c_p} \tag{2.17}$$

The relation $\frac{\hat{n}_t}{N_t}$ can also be expressed with fermi-dirac statistics by including the degeneracy of the state when unoccupied and occupied by electrons, respectively g_0 and g_1. Combined with equations 2.15 and 2.16 this yields a relationship between emission and capture rates determined by E_F and E_t:

$$\frac{e_n}{c_n} = \frac{g_0}{g_1} \exp\left(\frac{E_t - E_F}{kT}\right) \tag{2.18}$$

$$\frac{e_p}{c_p} = \frac{g_1}{g_0} \exp\left(\frac{E_F - E_t}{kT}\right) \tag{2.19}$$

These equations show that in the case of figure 2.3.4 where $E_t > E_F$, e_n and c_p are the dominant rates for electrons and holes resulting in a depletion of the states. In order to increase electron occupancy of the trap state, the Fermi level must be larger than the trap energy, $E_F > E_t$. The ratio $\frac{g_0}{g_1}$ is close to unity and therefore excluded in the rest of the discussion.

Capture rates

The reason for the dependency of E_F in equations 2.18 and 2.19 is that capture rates are strongly dependent on the free carrier concentrations given by equations 2.10 and 2.11. Capturing the same amount of carriers with low density is slower than if the concentration was high. At any moment a trap is subjected to a flux of carriers given by the rms average velocity and hole concentration $\langle v_p \rangle p$. Assuming a p-type material and acceptor type trap, the capture of these carriers is determined by the concentration of free hole states n_t in the trap and its capture cross section σ. The concept of capture cross section can be understood as the quantum mechanical version of the size of a net, in the way that a large cross section captures a larger quantity. A positively charged defect will repel positive charges and thus have a smaller capture cross section for holes than electrons. The capture rate of holes per occupied states then becomes:

$$c_p = \frac{\Delta(N_t - n_t)/\Delta t}{n_t} = \sigma_p \langle v_p \rangle p \tag{2.20}$$

Emission rates

Emission rates are intrinsic properties of a trap state, as it is independent of E_F. However, it shows a strong temperature dependency which is exploited in techniques like Thermal Admittance Spectroscopy described in section 3.6. Combining equations 2.11, 2.19 and 2.20 an expression for e_p can be achieved:

$$e_p(T) = \sigma_p \langle v_p \rangle N_v \exp\left(-\frac{E_t - E_v}{kT}\right) \tag{2.21}$$

Both $\langle v_p \rangle$ and N_v are functions of temperature and effective mass. Unlike the non-exponential temperature dependency of $\langle v_p \rangle$ and N_v, σ can show Arrhenius behavior on the form $\sigma = \sigma_\infty \exp(\frac{-\Delta E_\sigma}{kT})$. By defining the activation energy of the trap as $E_{pa} = (E_t - E_v) + \Delta E_\sigma$, the full temperature dependency of e_p is given as:

$$e_p(T) = \gamma T^2 \sigma_\infty \exp\left(-\frac{E_{pa}}{kT}\right) \tag{2.22}$$

where

$$\gamma = 2\sqrt{3} M_v (2\pi)^{3/2} k^2 m_p^* h^{-3}$$

Comparing equations 2.20 and 2.22 in light of equation 2.11, a p type semiconductor with $E_T > E_F$ will have slower rates for charge emission than capture.

2.4 pn-junctions

A pn-junction is created at the intersection of an n-type and a p-type region. This structure is the fundamental to many characterization techniques, including Current-Voltage 3.4, Capacitance-Voltage 3.5 and Admittance Spectroscopy 3.6. This review is based on Nelson [25], Streetman [20] and Smets et.al. [24] and will assume a perfect interface with no defect states, uniform doping and the simplistic drift-diffusion approximation which excludes effects like hot carriers and tunneling.

2.4.1 Space charge region at equlibrium

The moment a n-type layer is in contact with a p-type layer, net diffusion of majority carriers to the adjacent layer will commence. A deficit in majority carriers results in creation of a net charge in the layer, as the ionized dopants are no longer compensated. The diffusion process will continue, until the electric field ε created by the ionized dopants is strong enough to provide an equally strong drift current in the opposite direction and hence achieving equilibrium.

$$J = J_{diff} - J_{drift} = 0, \tag{2.23}$$

Net zero transport of charge across the interface also requires a constant Fermi energy throughout the structure. As the vacuum ionization energy $E_{vac}(x)$ must be continuous through the structure, a constant Fermi level must generate a slope in the vacuum energy leading to a difference in the work function $\phi(x) = E_{vac}(x) - E_F$. This difference describes the built in potential created by the electric field:

$$qV_0 = (\phi_n - \phi_p) \tag{2.24}$$

where ϕ is collected in the bulk of the layers. This electric field will have a maximum at the pn interface. The region between $-x_p$ and x_n is called the space charge region (SCR) and is assumed to be fully depleted of mobile charge. Additionally, all donors and acceptors in this region are assumed to be ionized with an electric field equal to 0 outside of the SCR. This common approximation is called the *depletion approximation* and is necessary for a simple analytic analysis of the pn-junction.

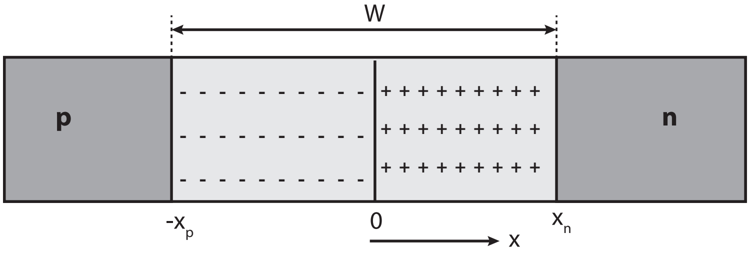

Figure 2.4.1: Space Charge Region of a p-n-diode.

The electric field $\varepsilon = -\nabla V$ must obey the Poisson equation, relating the gradient of electric field to the charge concentration ρ at a given position. As there are no mobile charges in the SCR and only a gradient in the x-direction, the equation simplifies to:

$$\nabla^2 V = \frac{\mathrm{d}^2 V(x)}{\mathrm{d}x^2} = \frac{q}{\epsilon}\rho = \frac{q}{\epsilon}(N_d^+ + N_a^-) \tag{2.25}$$

where q is the elementary charge, $\epsilon = \epsilon_0 \epsilon_r$ is the product of the vacuum permittivity and the specific permittivity of the material. Due to the boundary conditions $\left.\frac{\mathrm{d}V(x)}{\mathrm{d}x}\right|_{x \leq -x_p} = \left.\frac{\mathrm{d}V(x)}{\mathrm{d}x}\right|_{x \geq x_n} = 0$, V_0 can only change within the SCR and $V(x = -x_p) = 0$ and $V(x = x_n) = V_0$. Thus, the equation 2.25 integrates to the following equations:

$$\varepsilon = -\frac{qN_a}{\epsilon}(x + x_p) \qquad -x_p < x < 0 \tag{2.26}$$

$$V = \frac{qN_a}{2\epsilon}(x + x_p)^2 \qquad -x_p < x < 0 \tag{2.27}$$

$$\varepsilon = -\frac{qN_d}{\epsilon}(x - x_n) \qquad 0 < x < x_n \tag{2.28}$$

$$V = \frac{qN_d}{2\epsilon}(x - x_n)^2 + V_0 \qquad 0 < x < x_n \tag{2.29}$$

At the pn junction, both the electric field ε and V must be continuous. This condition allows equations 2.26- 2.29 to be solved for W.

$$W = x_p + x_n = \sqrt{\frac{2\epsilon}{q}\left(\frac{1}{N_d} + \frac{1}{N_a}\right)V_0} \tag{2.30}$$

This result shows that the total length of SCR, W, is intimately related to V_0.

2.4.2 Current flow in a junction

The result in the previous section is applicable at equilibrium conditions. V_0 is dependent on the Fermi level through equation 2.24 and W will thus vary with different doping level. Increasing V_0 results in greater W and a higher energy barrier between the n and p layers. By introducing a quasi Fermi energy which describes the steady state behavior of holes and electrons in a manner similar to E_F does at equilibrium, it is possible to use these results under steady state conditions.

Following from the depletion approximation, both E_v and E_c must be constant outside of the depletion region. Due to V_0, separations of energy bands in the two different layers must occur and are related to the built in potential as $qV_0 = \Delta E$. Under dark conditions and an applied bias V_a, V_0 can be replaced with a total potential of $V = V_0 - V_a$. Figure 2.4.2 illustrates the band bending occurring at both equilibrium and steady state conditions. By applying forward bias to the structure, with the positive electrode to the p-layer and negative to the n-layer, $V_a > 0$ and the band bending is reduced. Connecting the positive electrode to the n-layer to apply reverse bias has the corresponding result of increasing V.

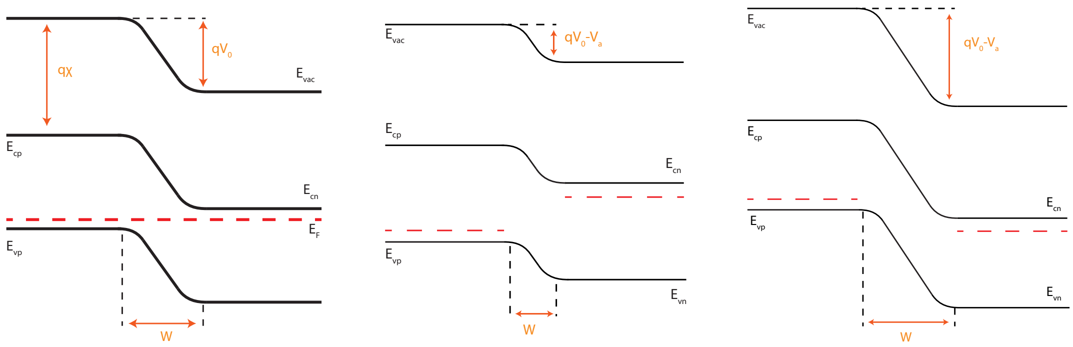

(a) Equilibrium conditions. (b) Forward bias. (c) Reverse bias.

Figure 2.4.2: Band structure of a pn-homojunction under equilibrium (a), forward bias (b) and reverse bias(c). The presence of an external potential influence both the degree of band bending and the depletion layer width.

The diffusion current through a junction is strongly dependent on the barrier, as majority carriers have to surmount the built-in potential. Reducing this barrier can be shown to translate into an exponential increase in current. On the other hand, increasing the barrier quickly quenches the diffusion current through the junction. Intuitively J_{drift} should also be dependent on the barrier. However, it describes drift of minority carriers across the junction and J_{drift} is thus limited by minority carrier generation in the close vicinity of or in the junction, not the electric field strength. It can be shown that current density under steady state conditions behave according to the diode equation:

$$J(V) = J_{diff} - J_{drift} = J_0 \left(e^{qV/kT} - 1 \right) \tag{2.31}$$

J_0 describes the minority carrier concentration fraction close enough to be swept across the junction and is often called the dark reverse current density.

2.4.3 Junction Capacitance

The capacitance of a junction, describing the ability to sustain electrical charge Q under varying voltage, is a key parameter for electrical analysis. It originates from the dipole in the SCR when subjected to a reverse bias. Within the space charge region the stored charge must be equal in both the n-layer and p-layer and is expressed as:

$$|Q| = qAN_dx_n = qAN_px_p \tag{2.32}$$

The total stored charge in either side of the junction is found by inserting equation 2.30 into the above statement:

$$|Q| = A\sqrt{2q\epsilon \frac{N_dN_a}{N_d + N_a} V} \tag{2.33}$$

It is clear that Q is non-linearly dependent on V. Applying the general definition of capacitance $C = \left|\frac{\mathrm{d}Q}{\mathrm{d}V}\right|$ results in the voltage variable capacitance for ideal homojunctions:

$$C = A\sqrt{\frac{q\epsilon}{2(V_0 - V_a)}\frac{N_d N_a}{N_d + N_a}} = \frac{\epsilon A}{W} \tag{2.34}$$

Surprisingly, this result is on the form of two parallel plates spaced by a dielectric material. Unlike a parallel plate capacitor, the charge is distributed throughout W yielding a non-uniform electric field. However, this result does indicate that only the fluctuation of charge at the edge of SCR is responsible for dQ which is consistent with the depletion approximation. This section has assumed an ideal semiconductor and thus excluded influence of defects on the capacitance. This will be addressed in section 3.5

Asymmetrical junctions

CV measurements are only able to provide unambiguous result for doping density, if the measured junction is asymmetrical. The difference in doping is commonly of several orders and the heaviest doped region is often marked with a plus sign. The SCR will extend further into the lightly doped layer compared with the heavy doped, as equation 2.32 indicates. In the case of a p^+n junction, the depletion region will extend almost exclusively into the n layer, resulting in $W \simeq x_n$. Equation 2.34 becomes:

$$C = \frac{A}{2}\sqrt{\frac{2q\epsilon}{V_0 - V_a}N_d} \tag{2.35}$$

2.4.4 Heterojunction

Creating a heterojunction requires two different semiconductors, with different electron affinity $\chi = E_{vac} - E_c$ and E_g. As in section 2.4.1, both the vacuum energy and Fermi level must be continuous in a junction at equilibrium. In contrast to the homojunction, discontinuities will arise at the edges of both the valence and conduction band. This complex band structure in the ideal case can be described by the *Anderson affinity rule*. This states that the offset at the CB minimum is related to the difference in affinity.

$$\Delta E_c = q(\chi_2 - \chi_1) \tag{2.36}$$

$$\Delta E_v = \Delta E_g - \Delta E_c \tag{2.37}$$

Consequently, the barrier for electrons and holes might be substantially different. An example could be a barrier for drifting electrons at the interface, caused by the discontinuity. The depletion region width is nevertheless a result of solving the Poisson equation as earlier, but also includes the different dielectric constants. The resulting expression for junction capacitance is similar to equation2.34:

$$C = A\sqrt{\frac{q\epsilon_0\epsilon_1\epsilon_2 N_{a1}N_{d2}}{2(\epsilon_1 N_{a1} + \epsilon_2 N_{d2})}\frac{1}{(V_0 - V_a)}} \tag{2.38}$$

A challenge for heterojunctions is different crystalline structures, resulting in lattice mismatch and interface defects. At high concentrations these defects may affect Fermi level throughout the material by pinning it at an energy. This deviation from ideal theory, effects both V_0 and the band bending. Band offsets must thus be found experimentally.

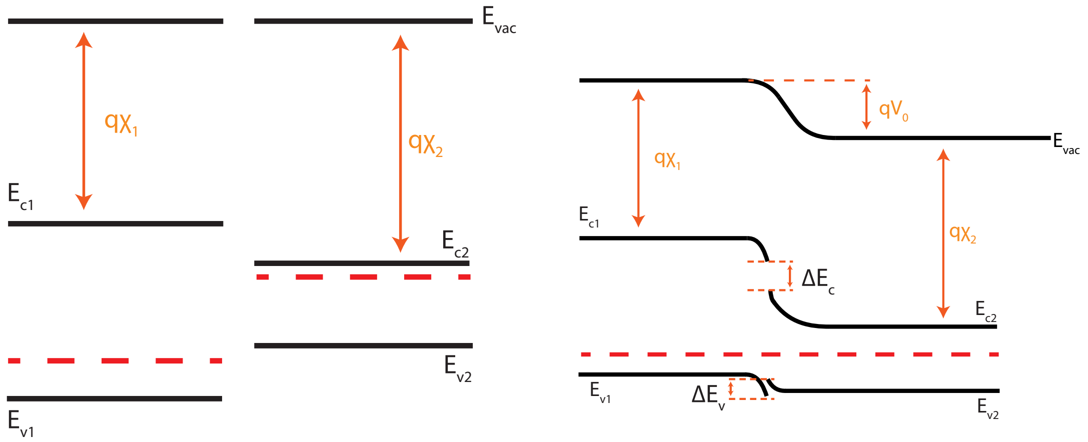

(a) Before junction, showing difference in affinity and band gap for material 1 and 2

(b) pn hetereojunction. Note the discontinuity in both E_V and E_C

Figure 2.4.3: The bandstructure of ideal hetereojunctions depends on electron affinity and band gap, leading to several different bandstructures. This illustrates the Cu_2O:n-Si junction, with material 1 referring to Cu_2O

2.4.5 Metal-semiconductor junction

The requirements of a continuous E_{vac} and constant E_F at equilibrium applies to metal-semiconductor junctions. As the two interfaces with work functions $q\phi_m$ and $q\phi_s$ are brought into contact, charge transfer occurs until the Fermi level is constant. Representing the work needed to remove an electron carrier from a material, the work function ϕ is defined as $\phi = E_{vac} - E_F$. A mismatch between the work functions can result in band discontinuities. In the case of n-type semiconductor and $\phi_m > \phi_s$ the conduction band is not continuable at the junction and a barrier arises for transport of electrons. This discontinuity is called the Schottky barrier and the resulting diode is termed a Schottky diode. Due to a high density of states and absence of band gap in the metal, the SCR extends only into the semiconductor. The junction capacitance for a Schottky diode is then necessarily the same as for a asymmetrical pn-junction.

The Schottky barrier $\phi_B = \phi_m - \chi$, where χ is the semiconductor affinity, retards the injection of electrons from the metal to a n-type semiconductor. Adapting the thermionic emission model and thus excluding tunneling as a transport mechanism, the probability for an electron to be transported across the barrier $q\phi_B$ into semiconductor is described by a Boltzmann factor. An ideal Schottky diode obeys the diode equation 2.31, but with the reverse current described by

$$J_0 = A^* T^2 e^{-q\phi_B/kT} \tag{2.39}$$

where A^* is the material specific Richardson constant. However, defects in the metal-semiconductor interface commonly induce states in the bandgap which affects ϕ_B. At high concentrations these interface states will pin the Fermi level at a fixed position and reduce the influence of $\Delta\phi$ on the band bending

2.5 Solar Cells

Over the course of a full year, the earth receives sunlight with an amount of energy far larger than the world's total energy consumption. Utilizing the photoelectric effect postulated by Einstein in 1905, solar cells represent the most direct way of harvesting this energy for electricity production. A good solar cell must be efficient in the following areas: (i) absorbing photons, (ii) separating the excited charge carriers and (iii) collecting these charges. The most common solar cell technology, the photovoltaic cell, is based on a semiconductor pn-junction and is the focus of the following review. This section is based on Nelson [25] and Smets [24].

Performance of a photovoltaic cell related to point (i) and (ii) is intimately related to the bandgap of the semiconductor, commonly referred to as the Shockley-Queisser limit. Ruhle [28] has shown that the optimal bandgap for any homojunction photovoltaic cell is 1.34 eV, giving a theoretical efficiency of converting 33.7% of the sunlight energy into electricity. The same analysis yields a 32% efficiency for a silicon homojunction, which is by far the most common technology on the market today. Currently the record for Si homojunction solar cells is 26.1% [6].

When photons of energy equal to or higher than E_g are incident on a pn-junction, EHP's are excited. The excited minority carriers inside and in close vicinity of the SCR will be transported across the junction, resulting in an increased current of minority carriers, see figure 2.5.1a. This photocurrent is simply included in the diode equation as:

$$J(v) = J_{dark}(V) - J_{sc} = J_0\left(e^{qV/nkT} - 1\right) - J_{sc} \tag{2.40}$$

where n is the ideality factor, which is >1 for non-ideal diodes. Illuminated photovoltaic cells thus show a non-zero current density J_{sc} at short circuit conditions ($V = 0$), corresponding to the maximum current throughput. Corresponding to the other extreme and equaling the built-in potential V_0 at equilibrium, the open circuit voltage V_{oc} represents the total potential the cell can produce. For most applications the solar cell is operated at a potential to deliver maximum power $P_{mp} = I_{mp}V_{mp}$. Thus the power conversion efficiency η of a photovoltaic-cell is given by

$$\eta = \frac{I_{mp}V_{mp}}{P_s} \tag{2.41}$$

where P_s represent the power received from the solar spectrum, often given by the global standard spectrum AM1.5G.

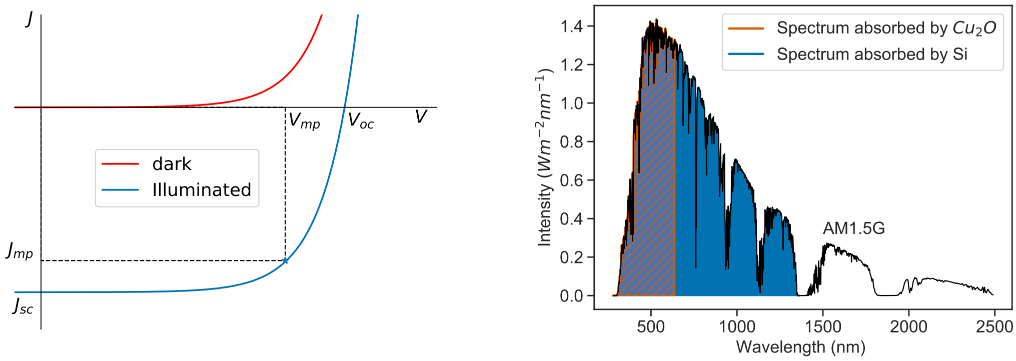

(a) (b)

Figure 2.5.1: Current-Voltage characteristics of a diode subjected to dark and illuminated conditions (a). Absorbed solar spectrum of Cu_2O and Si compared to AM1.5G (b).

2.5.1 Tandem Solar cells

When minority carriers are excited by photons with $E_{ph} > E_g$, they will be excited to an energy higher than E_C. Immediately after the excitation the carrier will loose any excess energy through a thermalization process, producing lattice vibrations. The tandem solar cell represents a solution to this problem, by stacking several layers of pn-junctions with different bandgaps on top of each other. Theoretically, this enables a higher utilization of the energy in the solar spectrum. In most cases hetereojunctions are required to create a tandem solar cell, thus introducing numerous practical challenges related to,among others, interface physics and band mismatch. Possible benefits are higher V_{oc} and J_{sc} and efficiencies above the Schockley-Queisser limit for a single solar cell. An infinte number of these stacks results in a Schockley-Queisser limit of 68% [12].

2.6 Cu_2O

There exist two stable and one metastable phase of oxidized copper. Cuprous oxide (Cu_2O) and cupric oxide (CuO) are both two stable Paramelaconite (Cu_4O_3) is metastable. Together with Se, Cu_2O was the first materials characterized as semiconductors. Much of the fundamental semiconductor physics were discovered and derived from the behavior of Cu_2O devices [29]. However, research and production of high purity and doped Si and Ge grew in the 1950s, taking over the leading role in semiconductor research. The following sections are based on Meyer [30] and Biccari [31].

Oxidizing Cu into Cu_2O requires high temperatures and low oxygen partial pressures, a process typically performed above 1000°C. However, with sputter deposition it is possible to create a pure Cu_2O phase at significantly lower temperatures. Cuprous oxide crystals are also found in nature and single crystals mined in e.g. Namibia show superior crystalline quality compared to man made crystals and are currently used to study excitons [32].

2.6.1 Material properties

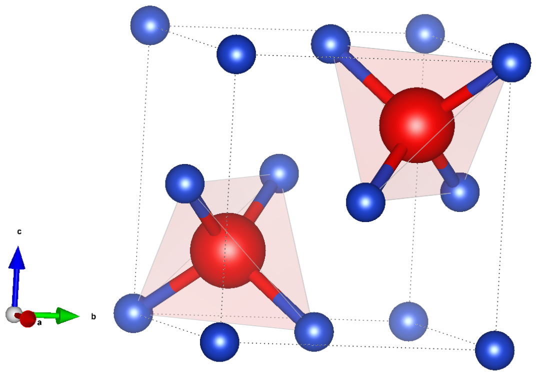

Figure 2.6.1: The blue spheres are Cu^+ ions, while the red are O^{2-} ions. The illustration is acquired through Vesta software [33]

Cuprous oxide crystallize in a simple cubic Bravais lattice with the space group (Pn-3m) describing the symmetry operations of the structure. Another way to view the primitive unit cell structure is as a fcc lattice of 4 Cu atoms and a bcc sub-lattice of 2 O atoms. These O atoms are located within 50 % of the tetrahedron holes in the fcc lattice, which has a lattice constant of a = 4.2696 Å [34].

At room temperature, Cu_2O has a direct bandgap of 2.1eV [35]. It shows natural p-type conductivity, with an effective mass for holes of $m_h^* = 0.66m_0$. The p-type conductivity is believed to originate from copper vacancies, which has been indicated by both experimental [16], [36] and theoretical studies [17], [19], [37]. Electrical properties are also found to vary with fabrication techniques, with the dependency on temperature and partial pressure during deposition expected to influence defects.

The possibility of n-type Cu_2O would enable the creation of a Cu_2O pn-homojunction, hence evading issues like band offsets and interface defects typically experienced by hetereojunctions. However, the formation energy of v_{cu} approaches zero when the fermi level increases into the upper half of the bandgap. This is expected to counteract the donor doping and in extreme cases transform the structure.

2.6.2 Defects

A deficit of cations is expected in oxides that are able to oxidize to a higher oxidation state at low oxygen partial pressures. In this case the more thermodynamical stable CuO. Furthermore, calculations performed by Raebiger et.al. [37] concludes that this deficit in Cu_2O is due to v_{Cu} and not excess of O_i. Copper vacancy concentrations can be as high as $10^{20}\ cm^{-3}$. However, hole concentrations at room temperature are observed to be significantly less than this. The commonly reported activation energy of $E_v + 0.25$ and compensating defects were proposed by Raebiger et.al. as an explanation. Furthermore, several copper vacancies configurations exist in cuprous oxide. It is disputed in literature which contribute the most to p-type conductivity.

As with any semiconductor, defects strongly influence the electrical properties of Cu_2O, some common defects are listed in table 2.6.2a. In 1972 Zouaghi et al reported a defect band attributed to cation vacancies at $E_V + (0.55- > 0.61)eV$ from near infrared absorption and photoconductivity measurements. Nitrogen located on oxygen sites has been found to act as a shallow acceptor and enhance hole concentration [38]. Additionally, sodium, magnesium, chlorine and silicon all behave as acceptors in cuprous oxide [31]. On the other hand, aluminum is a donor when occupying Cu sites.

Hydrogen is an interesting defect in many semiconductors. It has been hypothesized by de Walle [39] that it aligns universally in semiconductors which implies that H is expected to be located at $E_v + 0.84 \pm 0.4eV$ in the bandgap of Cu_2O. According to the theoretical study by Scanlon and Watson [40], hydrogen will always act as a "hole killer" in Cu_2O and diminish solar cell performance. Various trends are also reported on how increased hydrogen concentrations affect Cu_2O. During annealing of N-doped Cu_2O films, hydrogen was found to increase carrier density and reduce hole mobility [41], while incorporating H during the thermal oxidation of thin film Cu has been showed to have the opposite effect [42]. These conflicting trends emphasize the amphoteric nature of H in Cu_2O and are likely due to different ways of incorporating hydrogen, affecting the film morphology and the preferred site of hydrogen [43].

Defect	Energy level (eV)
H_i	Ev + 0.8 ± 0.5 [39]*
N_O	$E_v + 0.14$ [44]
v_{cu}^{split}	$E_V + 0.57$ [19]*
v_{Cu}	$E_V + 0.25$ [36], [45]
v_{Cu}	$E_V + 0.28$ [37]*

(a)

(b)

Figure 2.6.2: Tabulated values (a) of some known defects in cuprous oxide, with asterisks indicating DFT-based calculations. Graphical illustration of the defects (b), with $E_i = E_v + E_g/2$.

2.6.3 Cu$_2$o in solar cells

Cuprous oxide is a good candidate for use in next generation solar cells. High optical absorption [46] results in low material use, abundance of materials ensures scalability, while it is shows good stability and is non-toxic. Recent years has seen major advances with respect to conversion efficiency. Furthermore, it has a theoretical efficiency of $\sim 20\%$.

Due to the inability to dope n-type, research into Cu$_2$O based solar cells has mainly been focused on hetereojunctions with the n-type, conductive oxide ZnO. The improvement in solar cell efficiency of the recent years is in part due to an improvement of interface quality and introduction of new emitter layers [14], [15]. The current record holder, with 8.1% conversion efficiency, is based on a $Zn_{1-x}Ge_xO$ n-type emitter and a Na-doped Cu$_2$O base. However, the efficiency improvement is largely on thermal oxidized Cu sheets. These films are characterized with a mobility around $100 cm/Vs$, noticeable higher than what is obtained for thin films and indicating higher crystalline quality. With thin films it has proven difficult to exceed 1%, but with a gallium oxide buffer layer 4% has been achieved using [15].

Thin film Cu$_2$O enables the production of tandem solar cells. A theoretical structure with a ZnO:Cu$_2$O topcell and Si bottom cell has a theoretical conversion efficiency of $\sim 40\%$ [12], compared to 29.8% for a Si-homojunction [47]. However, care must be taken to avoid Cu diffusion into Si. Copper is both a fast diffusing species and has a detrimental effect on minority carrier lifetime [48].

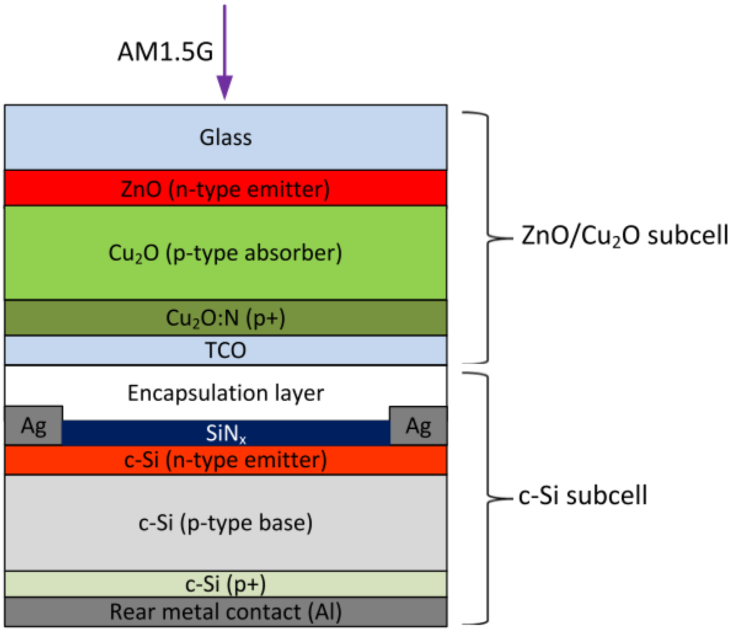

Figure 2.6.3: Proposed implementation of Cu_2O in a tandem solar cell as suggested by [49]. TCO is an abbreviation of Transparent Conductive Oxide

2.6.4 Li doping of Cu2O

Controlling hole concentration in Cu_2O is of major importance for solar cell applications, as a high carrier concentration results in higher minority recombination rates. According to a study conducted by Isseroff [19], Li doping is expected to inhibit the formation of copper split vacancies v_{Cu}^{split}, identified as the vacancy contributing to hole conduction. A split vacancy is described as a simple copper vacancy together with a neighboring Cu atom in a stable intermediate state between the vacancy and its original position.

To the best of my knowledge, there is no published work on the effect of Li doping on electrical performance in Cu_2O. Sodium has on the other hand been used as a dopant in thin filmCu_2O, showing increased carrier concentration with doping [50], [51].

3 Experimental Methods

3.1 Sputtering

Sputtering is a thin film deposition technique combining plasma and ballistic collisions within a target material. The series of collisions results in atoms and molecules being ejected and consequently deposited on a substrate. Campbell [52] together with Frey and Hartmut [53] is the foundation of this review.

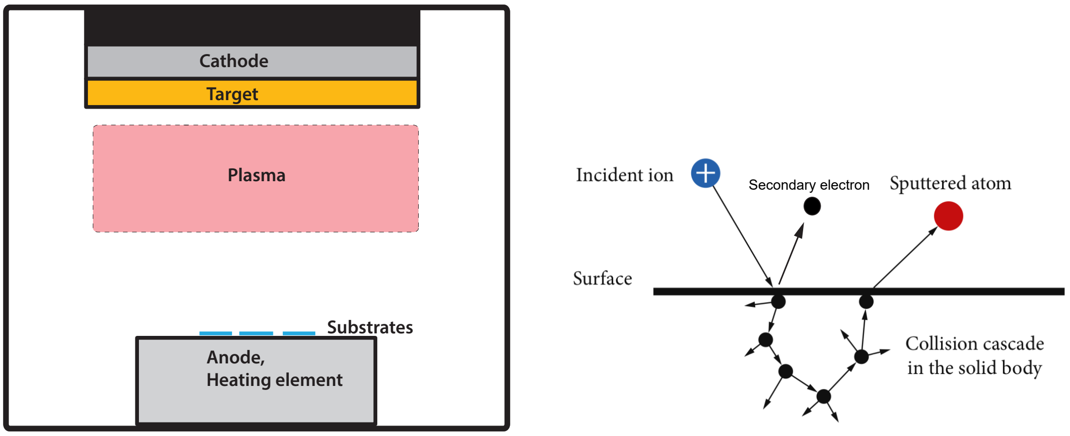

(a) (b)

Figure 3.1.1: Illustration of a simple sputtering chamber (a). Most chambers has the possibility to heat the substrates to allow better surface mobility and morphology. Figure (b) illustrates basic sputtering ballistics, adapted from Frey [53]

3.1.1 Glow discharge

Plasma is commonly referred to as the fourth state of matter and is a partially ionized gas consisting of ionized atoms and molecules, in addition to electrons. In order for gas to be excited into plasma, a large potential is required. This break down voltage is predicted by Paschen's law and is a function of both the gas pressure and distance over which the potential is distributed. Figure 3.1.1a illustrates a simple sputtering chamber. Positive ions from the plasma will be accelerated towards the negative cathode. Upon impact on the target surface, secondary electrons are ejected and accellerated towards the anode. Although the chamber is kept under a vacuum typically around 1e-3 torr, electrons may collide with gaseous species. If the electron energy is less than the ionization potential of the species it will be excited. The following decay might include optical transitions depending on the transferred energy, which will result in a characteristic glow. On the other hand, if the electron energy is larger than the ionization potential, new ions will be created and accelerated towards the cathode and the process will be repeated.

3.1.2 Deposition

When an ion is incident on the target surface with an energy above 10eV, it may penetrate the surface producing a series of collisions within the material. This energy will be deposited as heat, but also as physical rearrangement in the material. For ion energies lower than 5keV most of this energy is absorbed within a few atomic layers and the following collision cascade may result in atoms and molecules being sputtered from the surface. These ejected atoms and molecules escape with energies ranging from 10 to 50 eV, where atoms constitute about 95% of the ejected species. Compared to thermal evaporation, where evaporated species has about 1/100 the energy, this results in higher surface mobility of the adatoms on the substrate surface. Sputtering of alloy or compound targets may result in a stoichiometry that is slightly different from that of the target bulk.

The cathode-anode potential can be supplied in two ways: either by a Direct Current (DC) potential or an alternating potential with high frequency called Radio Frequency (RF). DC produces the highest deposition rate of the two, but requires a conductive target material to avoid charge build up on the target surface and a consequent quenching of the plasma. RF sputtering is used in the cases of insulation targets.

Magnetic confinement of the plasma is a method to increase plasma density and thus the total sputtering yield and is called Magnetron sputtering. As an ion with velocity **v** is subjected to a magnetic field **B** it will experience a Lorentz force perpendicular to both velocity and field:

$$\mathbf{F} = q(\mathbf{v} \times \mathbf{B}) \tag{3.1}$$

Ions will, due to their higher mass, be largely unaffected by this force in a sputtering chamber. Electrons will however be confined to a circular trajectory determined by the field strength and electron velocity. This confinement results in an increasing probability of exciting a neutral gas particle

3.2 X-ray diffraction

This section is based on Birkholz [54] and Leng [55]. X-ray diffraction (XRD) is a non-destructive technique for investigating the structure of crystalline materials. Information about crystal quality, plane directions and hence information about phases can, among other things, be deduced. Incident x-rays are scattered from the sample and the following pattern of constructive and destructive interference is measured.

As photons interacts with matter, energy is exchanged. While inelastic scattering also occurs, only the elastic scattering mechanism called Thompson scarring is utilized in XRD measurements. The electrons starts to oscillate like a Herz dipole ,with the frequency of the incident photon. A photon is in turn emitted with the same wavelength λ as the incident.

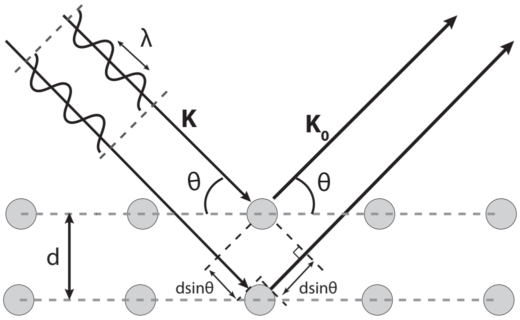

Figure 3.2.1: Illustration of photon interacting elastically with a crystal. When $2d\sin\theta$ is equal to the an integer wavelength of the incident photon, constructive interference is observed.

Figure 3.2.1 illustrates the scattering occurring as a photon with wave vector **K** is incident on a crystal. The net transfer of momentum that occurs from this interaction, where **K** is scattered to $\mathbf{K}_0$, is described by the scattering vector **Q**.

$$\mathbf{Q} = \mathbf{K} - \mathbf{K}_0 \tag{3.2}$$

By analogy to kinetic theory of gases, **Q** can be understood as a momentum transfer vector. The direction of momentum transfer when a molecule collides with a wall is measured as $\Delta\mathbf{P} = \mathbf{P} - \mathbf{P}_0$, analogous to the definition of **Q**. Laue described the conditions for constructive interference, and thus maximum intensity, between a lattice with arbitrary geometry and **Q** . For a simple cubic system with lattice constant a and orthogonal unit vectors $\mathbf{c}_j$, this occurs when:

$$\begin{aligned} a\mathbf{Q}\mathbf{c}_1 &= 2\pi h \\ a\mathbf{Q}\mathbf{c}_2 &= 2\pi k \\ a\mathbf{Q}\mathbf{c}_3 &= 2\pi l \end{aligned} \tag{3.3}$$

where h, k and l are the Miller indices of the plane producing the constructive interference. By solving the equations in 3.3 for **Q**, the condition for maximum intensity becomes:

$$\frac{|\mathbf{Q}|}{2\pi} = \frac{\sqrt{h^2 + k^2 + l^2}}{a} \tag{3.4}$$

It can be shown that $|\mathbf{Q}| = \frac{4\pi}{\lambda}\sin\theta$. By inserting this in equation 3.4 and accounting for the relationship between the interplanar spacing d and a simple cubic lattice, Braggs law is found:

$$2d_{hkl}\sin\theta_B = n\lambda \tag{3.5}$$

where θ_B is the angle θ at which the intensity is at a maximum and is called the Bragg angle. By considering the geometry of figure 3.2.1, $2d_{hkl}\sin\theta_B$ can be described as the additional distance traveled if the scattering occurs one atom layer deeper in the structure. If this equals $n\lambda$, this additional travel does not result in a phase difference of the reflected light.

3.2.1 $\theta/2\theta$ scan

The $\theta/2\theta$ scan is an extensively used method for characterizing poly crystalline materials, measuring intensity as a function of the angle θ. As the angles are varied, both the source and the detector moves in a circular orbit around the substrate, as is illustrated in figure 3.2.2. In order to eradicate variation intensity due to $\mathbf{R}$, the radius of the circle is fixed at $\mathbf{R}$ during the entire scan. The scattering occurs in the plane spanned by the coordinate vectors $\mathbf{s}_1$ and $\mathbf{s}_3$, which is respectively parallel and perpendicular to the sample surface. Consequently $\mathbf{Q}$ is parallel to $\mathbf{s}_3$ and only lattice planes oriented parallel to the surface will give rise to Bragg diffraction.

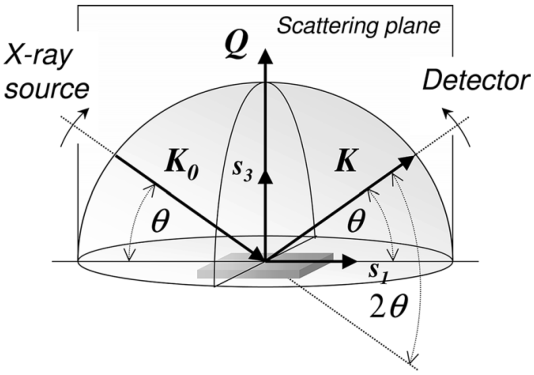

Figure 3.2.2: Illustration of $\theta/2\theta$ scan. The name $\theta/2\theta$ is related to θ being measured relative to the surface plane and not the surface normal, yielding an angular difference between $\mathbf{K}$ and $\mathbf{K}_0$ of2θ.

3.3 Secondary Ion Mass Spectrometry

Secondary Ion Mass Spectrometry (SIMS) is a powerful tool to analyse concentrations of elements in a sample and is capable of detecting relative concentrations as low as 10^{-6}. The ability to measure almost every element in the periodic table and separate between isotopes makes it a popular tool in academic research. Leng [56] has provided the theoretical background and describes two different modes of operation: the non-destructive *static* SIMS which measures the sample surface and the destructive *dynamic* SIMS for depth profiles.

A finely calibrated and focused ion beam consisting typically of either Cs^+, Ar^+, O^+, Ga^+ is accelerated towards a sample. The bombardment of these primary ions results in atoms being sputtered from the sample. Only approximately 1% of these secondary particles are ionized and thus possible to analyse by a mass spectrometer. After being sputtered, the ions are accelerated towards an area with perpendicular magnetic and electric field. The magnetic and electric forces act in opposite directions and the resulting path deflection is dependent on the mass to charge ratio, enabling filtering of various isotopes. Ultra high vacuum is required in order to minimize particle interaction and an undisturbed trajectory for the secondary ions, so that flux recorded by the mass spectrometer is representative.

As SIMS is a very sensitive technique where several aspects may influence the results. The sputtering yield of various elements may vary by several orders of magnitude in the same sample. To deal with this, the primary ion source needs to be selected carefully. Careful aligning of the mass filter described in the previous section is also vital. When every precaution is taken to limit measurement errors, the intensity measured in counts/s must be converted to concentration/depth. This is solved by measuring a sample with known concentration of the impurity in question. Converting time to depth is done by measuring the depth of the crater creating by the sputtering process and assuming a constant erosion rate.

3.4 Current-Voltage

This section is based on Streetman [20] and Nelson [25]. The current-voltage behavior of diodes is not only fundamental for the intended application of the diode, but also electrical characterization techniques like Capacitance - Voltage and Admittance Spectroscopy. The diode equation (2.31) does not adequately describe the plethora of physical mechanisms in a real junction that deviate from the simple theory. This is partially compensated by introducing the *ideality factor* n, which incorporates some of the mechanisms excluded by the depletion approximation. Equation 2.31 then becomes:

$$J(V) = J_0 \left(e^{qV/nkT} - 1 \right) \tag{3.6}$$

Deviations from the ideal equation, i.e. $n > 1$, can be caused by several mechanisms. Recombination in the SCR, for instance through recombination centres, and unwanted interface layer are both linked to $1 < n < 2$ [27], while quantum mechanical tunnelling through an abrubt hetereojunction could lead to $n > 2$ [25]. If a shunt current is present, an additional current $-I_{sh}$ is added to the equation. Several shunt mechanisms are possible, including quantum mechanical tunneling, conduction along grain boundaries or other defects through the junction are all examples. In the ideal case, this current is determined by diffusion of minority carriers across the junction and is thus expected to depend on a barrier in the form of a Arrhenius-like behavior of temperature.

When comparing the current during reverse and forward bias conditions, it is clear that a diode is rectifying. At high forward bias, series resistance in the diode becomes a limiting factor and saturates the current. Poor resistance for leakage current, also called shunt current, will on the other hand result in a higher than ideal reverse current. Effects like quantum mechanical tunneling and conductive grain boundaries, among others, contribute to shunt current. Poor mobility, carrier trapping and scattering are among the mechanisms contributing to increased series resistance.

3.4.1 Forward bias behavior

A plot of $\ln J(V)$ is from equation 2.31 expected to be linear at forward bias. However, at high forward bias series resistance become a major factor and limits the current. Prior to current saturation and assuming $V >> \frac{kT}{q}$ the equation 3.6 can be rearranged as following:

$$\ln J = \frac{q}{nkT}(V_0 - V_a) + \ln J_0 \tag{3.7}$$

The ideality factor n can be found by the derivative $d(\ln J)/dV$ in the ideal region.

3.5 Capacitance - Voltage

At equilibrium and reverse bias, the depletion approximation states that the flux of mobile carriers in the SCR is negligible. As a consequence, Capacitance-Voltage (CV) measurements will reveal the depletion layer width for ideal diodes, from which both the effective doping density and built-in voltage can be deduced. A small AC test signal is superimposed on the DC voltage, enabling a non-zero capacitance for depletion widths fluctuating around the steady state $W(V_{DC})$. Typically, this AC signal has a frequency of 1MHz, ensuring that the measured capacitative admittance is large compared to leakage conductance and that the charges that moves in response to the test signal are free carriers. This section is based on Blood [27], Kimerling [57] and Schroeder [58].

Assuming uniform doping, equation 2.34 and 2.38 predicts a linear line when plotting $\frac{1}{C^2}$ - V, with a slope determined by the doping density. However, doping concentration is not measured directly. Due to the high frequency of the AC test signal, only electrons and holes at the depletion region edge are mobile enough to respond and contribute to C. Therefore, the measured N_{scr} is a combination of ionized states at the SCR edge and diffused free carriers. In the ideal case, the measured ionized charge density N_{scr} is equal to the compensated doping density. Unambiguous values for $N_{scr}(V)$ from dC^{-2}/dV are only possible when considering asymmetrical junctions, as the variation in depletion layer edge in the highly doped layer can be neglected. Under forward bias, an additional capacitance is present due to response of injected minority carrier to the AC signal.

$$\frac{1}{C^2} = \frac{2}{\epsilon_0 \epsilon_r A^2 N_{scr}}(V_0 - V_a) \tag{3.8}$$

Similarly to the diffusion of minority carriers under forward bias, excessive leakage current will affect the capacitance. Even when neglecting the leakage conductance and instrumental accuracy, the accuracy of the depletion layer edge is limited by the Debye length L_D and has a fundamental uncertainty of $\pm L_D$. This describes the screening effect arising when mobile charges diffuses to the fixed charges in the SCR. This also results in a tail of free carriers in the depletion layer.

$$L_D = \sqrt{\frac{kT\epsilon_0\epsilon_r}{q^2(p(x_p) + n(x_n))}} \tag{3.9}$$

3.5.1 Influence of deep states

The presence of deep states is not included in the depletion approximation. At trap concentrations $N_t > 0.1|N_a - N_d|$ these states significantly influence the capacitance of a junction, even at temperatures where the probability of thermal carrier excitation in the bulk is low. As the depletion width varies with the superimposed AC voltage, $W = W_{DC} \pm \Delta_{AC} W$, holes from the quasi neutral region will find themselves in the SCR and be subject to capture and emission processes by the trap. The rate of DC voltage increments, $\frac{\partial}{\partial t}\Delta V_{DC}$, is assumed to be small.

Reviewing the case of acceptor type trap states with $e_t^{th} > \omega_{AC} = 2\pi f_{AC}$, located in the lower half of the band gap as depicted in figure 3.5.1, the trap emission rate is sufficient for the trap occupancy to oscillate in phase with the applied AC voltage. Unlike shallow states, trap occupancy between x_p and x_T is partial and governed by Fermi-Dirac statistics. The actual ionized charge density is thus a function of position, $N_{scr}(x) = N_a^-(x_p) + N_t^-(x_p \leq x \leq x_t)$. Consequently, the measured x_p will be a charge-weighted average of $x_p \leq x < x_T$.

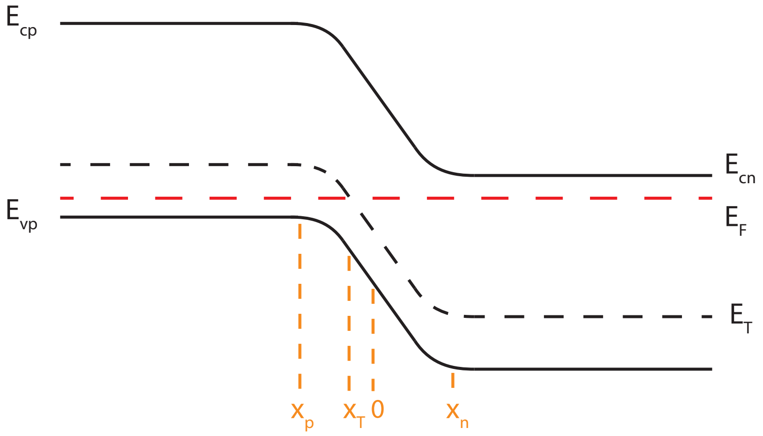

Figure 3.5.1: Illustration of deep states in a pn-homojunction under equilibrium conditions. For simplicity, the presence of shallow donor and acceptor traps is not included in the illustration. If the states at E_T are acceptor type, they will be ionized at $x \geq x_t$, in contrast to donor states which will be electrical neutral in the same interval and ionized for $x \leq x_T$.

In the case of $e^{th} < \omega_{AC}$, trap emission rates are out of phase with ω_{AC}. Consequently defect states between $x_p \leq x < x_t$ are no longer able to contribute to junction capacitance. Assuming on the other hand that $e^{th} > \Delta V_{DC}$, the state is expected to contribute to the capacitance. The total measured $N_{scr}(x_p)$ is thus $N_{scr}(x_p) = N_t(x_t)\frac{x_t}{x_p} + N_a(x_p)$.

3.6 Admittance spectroscopy

Admittance spectroscopy is a majority carrier traps characterization technique, which investigates the trap response to an external and oscillating voltage $V(\omega)$ with angular frequency ω. Key parameters like e^{th}, σ and N_t are studied in light of junction conductance (G) and capacitance (C). Both G and C are dependent on the relationship between ω and emission rate. Trap occupancy oscillate either in or out of phase with the AC signal, at low and high ω, respectively. Contrary to C-V measurements, the DC bias will be fixed while ω and temperature are variables. An absence of interface states is assumed, in addition to abrupt change in trap occupancy ($p_t(x)$) as $E_t(x)$ crosses E_F. In order to discuss modulation of hole concentration $p_t(x,t)$, the *truncated space charge approximation* is employed. It deviates from the depletion approximation by allowing the presence of free carriers in the depletion region. The work of Blood and Orton [27] is the foundation of this discussion and acceptor type traps will be assumed in the discussion.

Complex admittance $Y(\omega)$ is defined in equation 3.10 as the response of current to a oscillating potential on the general form $V(\omega) = V_0 \exp(i\omega t)$.

$$I(\omega) = Y(\omega)V(\omega) = [G(\omega) + i\omega C(\omega)]\,V(\omega) \tag{3.10}$$

$V(\omega)$ modulates the quasi Fermi level and in turn the depletion layer width, $\delta W = \delta x_p + \delta x_n$. This results in charge fluctuation from deep and shallow states as discussed in section 3.5.1. Current is simply the time derivative of charge and equation 3.11 describes the contributions from both shallow and a deep states to $I(t)$ as $V(\omega)$ modulates. At any time, the current depends on change in both the free carrier concentration in SCR $\delta q_a(t)$ and the surplus concentration $\delta p_t(x,t)$ generated by $V(\omega)$. Emission from shallow states is assumed instantaneous and $\delta q_d(t)$ is a function of the variation in depletion layer edge. This assumption is not valid for deep states, where capture and emission rates are strongly position dependent and $\delta q_t(t)$ must therefore be integrated across the entire depletion region.

$$I(t) = \frac{\mathrm{d}}{\mathrm{d}t}\delta q_a(t) + \frac{\mathrm{d}}{\mathrm{d}t}\delta q_t(t) = \frac{\mathrm{d}}{\mathrm{d}t} q N_a(x_p)\delta x_p(t) + \frac{\mathrm{d}}{\mathrm{d}t} q \int_{x=0}^{x_p} \delta p_t(x,t)dx \tag{3.11}$$

Change in trap concentration, $\frac{\partial}{\partial t}\delta p_t(x,t)$, is both dependent on trap emission and the capture of free carriers in the SCR, described by 3.12. The position dependent capture rate inside the SCR, $c_p(x,t)$, is given by $c_p(x,t) = \sigma_p\langle v_p\rangle p(x,t)$.

$$\frac{\partial}{\partial t}\delta p_t(x,t) = c_p(x,t)[N_t - p_t(x,t)] - e_p^{th} p_t(x,t) \tag{3.12}$$

By assuming that the distribution of $\delta p_t(x,t)$ is narrow compared to x_t, it follows that $c_p(x_t) = e_p^{th}$. The stored charge distribution take the form of a square of height $\delta p_t(t)$ and width δx_t. In the special case of low ω and instantaneous trap response, this square has the amplitude of N_t. This allows equation 3.11 to be solved analytically and $\delta q_t(t)$ has the complex form of 3.13:

$$\delta q_t(t) = \frac{g_t}{f_t + i\omega} V_0 \exp(i\omega t) \tag{3.13}$$

$$f_t = 2e_p^{th}\left(1 + \frac{x_t}{x_p}\frac{N_t}{N_a}\right) \tag{3.14}$$

$$g_t = 2e_p^{th}\frac{\epsilon_0\epsilon_r}{x_p}\frac{N_t}{N_a} \tag{3.15}$$

the factor 2 in front of e_p^{th} represents that $c_p(x_t) = e_p^{th}$, while f_t describes the frequency where $C(\omega)$ has an inflection point. This result illustrates that by increasing ω, the phase of $\delta q_t(t)$ is deviating from $V(\omega)$. Combining this result with equation 3.10 and 3.11 for the limits of $\omega << f_t$, the conductance must be zero as $\frac{\mathrm{d}}{\mathrm{d}t}\delta q_d(t) \to 0$. Thus the diode behave like a lossless capacitor with $I(\omega) = i\omega C(\omega)V(\omega)$ and the current phase leading $V(\omega)$by $\frac{\pi}{2}$. This conductance includes both contributions from shallow and deep states.

The picture becomes more complicated as ω increases. $\delta q_t(t)$ becomes increasingly out of phase with the applied voltage fluctuations and conductance from the SCR follows. At higher frequencies, i.e. $f_t \simeq \omega$, e_p^{th} is not able to emit charge fast enough to follow ω. This results in $\delta q_t(t)$ lagging behind $V(\omega)$. The trap will thus emit carriers even when $E_t(x) < E_F$ indicates it should capture carriers, leading to current leaking from the depletion region and $G \neq 0$. At high frequencies the trap is no longer able to respond to the applied bias and C_∞ is given by the charge modulation of only shallow states , while the conductance reaches a high frequency value G_∞. Equations 3.16 and 3.17 describes the transition between the two extreme values for capacitance and conductance.

$$C(\omega) = C_\infty + \frac{\Delta C}{1 + \frac{\omega^2}{f_t^2}} \tag{3.16}$$

$$G(\omega) = \frac{f_t}{1 + \frac{f_t^2}{\omega^2}} \Delta C \tag{3.17}$$

3.6.1 Extraction of trap parameters

Admittance spectroscopy can be performed by either varying ω at fixed temperatures or, as e^{th} is a function of temperature, applying a fixed set of ω during a temperature scan. At low temperatures the thermal emission rate of traps is low, which corresponds to the high frequency limits obtained above. Increased temperature leads to an increase in emission, resembling the low frequency limit. Figure 3.6.1 show the expected behavior of $G(\omega)$ and $C(\omega)$, but also show that G/ω peaks at $\omega = f_t$, a peak which has the convenient height of $\frac{1}{2}\Delta C$.

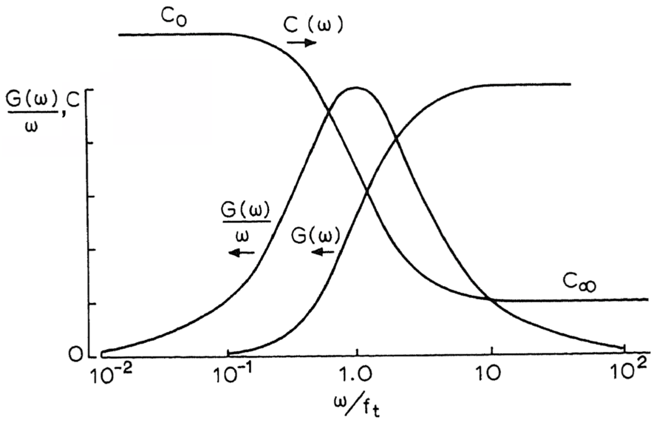

Figure 3.6.1: figure adapted from figure 9.12 in Blood [27].From equation 3.16 it is clear that $\Delta C = C_0 - C_\infty$.

The parameter ΔC is related to N_t. By assuming, $\frac{x_t}{x_p} \rightarrow 0$ and $N_t/N_a \leq 1$, ΔC simplifies to equation 3.18. Further, this enables a qualitative description of trap concentration. With this assumption, equation 3.14 also simplifies to $f_t = 2e_p^{th}$.

$$\frac{\Delta C}{C_\infty} = \frac{N_t}{N_a}\left(\frac{1 - x_t/x_a}{1 + x_t N_t/x_a N_a}\right) \underset{x_n >> x_t}{\simeq} \frac{N_t}{N_a} \tag{3.18}$$

During a thermal admittance spectroscopy (TAS) measurement with multiple frequencies, this results in several peaks of G/ω. These temperatures together with equation 2.22 enables a linear Arrhenius plot of f_t/T^2 v $\frac{1}{T}$, where the gradient reveals E_{na}.

Absence of interface states has been assumed during this discussion, an assumption not valid for hetereojunctions and $\frac{x_t}{x_p} \rightarrow 0$. Interface states are typically distributed in energy, which results in a broad peak of $G(\omega = f_t)/\omega$. Interference with deep bulk states can be mitigated by increasing the DC bias and thus moving the point where $E_t(x) = E_F$. High series resistance in the diode will also affect a measurement, resulting in decreasing conductance with increasing ω. At low temperatures, series resistance is expected to increase due to carrier freeze out.

3.7 Hall Measurements

The Hall effect allows for measurement of electrical properties of samples, including free carrier concentration, resistivity and mobility. Streetman [20] and Kittel [23] has provided the theoretical background.

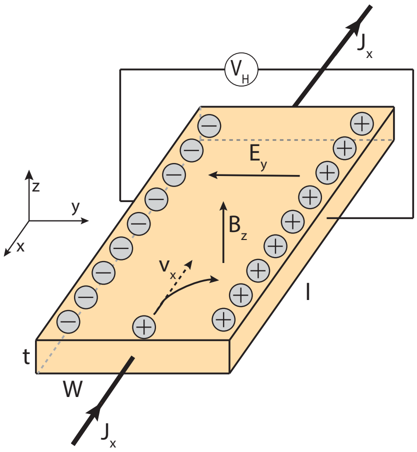

Figure 3.7.1: Hall effect in a p-type semiconductor.

This effect is caused by the interaction between electric charge and magnetic and electric fields. A mobile charge with velocity **v** and charge q experiences a Lorentz force when subjected to a magnetic (**B**) field, which acts perpendicular to both **v** and **B**. The resulting drift of carriers establishes an electric field **E** within the sample, illustrated in figure 3.7.1. The total force **F** experienced by a charge introduced to the sample is thus given by equation 3.19

$$\mathbf{F} = q(\mathbf{E} + \mathbf{v} \times \mathbf{B}) \tag{3.19}$$

where q is the charge of the mobile species. Steady flow of charges through the sample requires a net zero force in the x direction, ie. $E_y = v_x B_z$, with the corresponding electrical potential $V_H = E_y w$ termed the Hall voltage. By including the drift velocity of holes through the sample, $v_x = \frac{J_X}{qp}$ into this expression, the field becomes

$$E_y = \frac{J_x}{qp} B_z = R_H J_x B_z \tag{3.20}$$

The proportionality constant $R_H = (qp)^{-1}$ is the Hall coefficient, defined by the hole concentration p. By controlling the current flow and magnetic field while measuring the Hall voltage for a sample with dimensions w, t, l, the carrier concentration can be extracted

$$p = \frac{1}{qR_h} = \frac{B_z(I_x/wt)}{q(V_H/w)} = \frac{I_x B_z}{qtV_H} \tag{3.21}$$

Combining this result with a measurement of the sample resistance R, the sample resistivity ρ can be determined:

$$\rho = \frac{V_x}{I_x}\frac{wt}{l} = \frac{Rwt}{l} \tag{3.22}$$

The conductivity describes the ability of charges to move in a sample. It is consequently defined as both the inverse of resistivity and as a function of the mobility μ.

$$\sigma_p = \rho^{-1} = q\mu_p p \tag{3.23}$$

Throughout the above discussion, holes have been used as an example but by simply changing the sign of charge, this theory is also valid for electrons. As the sign of the Hall coefficient is determined by the charge, the value of R_H provides a simple way of determining whether the majority carriers are holes or electrons.

3.7.1 Temperature Dependent Hall

A non-degenerate, p-type semiconductor (i.e. $E_F - E_V \geq 3kT$) doped with N_a shallow acceptor states and N_d donors will show a characteristic temperature dependency. At high temperatures the acceptor concentration is simply equal to the compensated doping density. However, a measurement of carrier concentration with lowering temperature reveals more fundamental properties of the dopants. Hole concentration show a temperature dependency according to equation 2.11. The electroneutrality in equation 3.24, portraits a similar temperature dependency, as ionization of acceptor atoms depends on Fermi Dirac statistics.

$$p = N_a^- - N_d = N_a(1 - \frac{1}{1 + \beta \exp\left(\frac{E_F - E_a}{kT}\right)}) - N_d \tag{3.24}$$

where the plus and minus signs refers to the ionization of dopant atoms and β is a degeneracy factor equal to $\frac{1}{2}$ for simple acceptors. Combining equation 2.11 with 3.24 and solving for p yields the following expression:

$$\frac{p(p + N_d)}{N_a - N_d - p} = \beta N_V \exp\left(-\frac{E_a - E_V}{kT}\right) \tag{3.25}$$

A measurement of $p(T)$ can thus be fitted to this equation, revealing information about $E_V + E_a$, N_a and N_d.

3.8 Devices simulation

Physical simulation of semiconductor devices is a powerful tool to gain insight into the physics at varying bias and boundary conditions. The Technology Computer Aided Design (TCAD) software Silvaco Atlas has been utilized in this work. Simple analytical expressions do not adequately describe the effect of trap parameters on the complex structure of Cu_2O-Si heterostructure. This section is based on Maiti [59] and the Silvaco user manual [60].

3.8.1 Silvaco Atlas

Silvaco Atlas is a two and three dimensional simulator predicting electrical performance of a defined semiconductor device. The physical structure can either be obtained through the process simulator Silvaco Athena or by a theoretically defined device. A variety of external stimuli including optical, thermal and stress can also be applied. These definitions and more must be implemented in a rigid sequence in order for Atlas to compile:

1) **Definition of physical structure**.This includes a definition of mesh size and resolution, constituting a discrete set of datapoints at which the simulations are performed. Any material properties that is not given by predefined values, e.g. doping, defects and electrical, optical and thermal parameters must also be set. Additionally, contacts and regions containing variously defined materials are determined.

2) **Physical models specification**: Flags can activate equations describing phenomenas like temperature dependent band gap narrowing. different recombination processes and incomplete ionization of electrical states.

3) **Numerical methods specification**: Defining the iterative procedure for obtaining a converging result based on initial guesses.

4) **Solution statements**: Defining the parameter space in which the device will be solved. Bias conditions, including contact potential, illumination and small signal AC frequencies can be set according to the user's preference.

In contrast to the simple analytical expressions derived for a pn junction, Silvaco Atlas is not bound by the assumptions of the depletion approximation. This is done by numerically solving the foundational equations which govern all semiconductor physics. Although there are only four such equations, they are in the general case coupled differential equations which are only possible to solve analytically under strong assumptions. Linking electrical potential to electrical charge density, the Poisson equation 2.25 can be described individually for electrons and holes. As these charge densities varies with carrier flux J, recombination R and generation G rates as well as current flux, they need to be counted in the continuity equations:

$$\frac{\partial n}{\partial t} = \frac{1}{q}\nabla \cdot \mathbf{J}_n + G - R \tag{3.26}$$

$$\frac{\partial p}{\partial t} = -\frac{1}{q}\nabla \cdot \mathbf{J}_p + G - R \tag{3.27}$$

Although these four equations provide the fundamental physics, a description of current flow in the device **J** must be presented. Diverging further from the depletion approximation, Atlas is able to provide more advanced models than the drift-diffusion model. On the other hand, the software also contains several default settings for both materials and models. This makes trouble shooting difficult in some cases.

3.8.2 Previous simulations of Cu_2O

Some Silvaco simulation work has been performed on Cu_2O in litterature. Nordseth [49] investigated the ZnO/Cu_2O heterojunction with different buffer layers. By varying the defect concentration in both Cu_2O and the interface layer he found that the short circuit density were significantly affected by the trap density for densities $N_t > 1 \cdot 10^{16} cm^3$ in both the interface layer and bulk Cu_2O. Although this indicates a high tolerance for defect density, it is worth mentioning that he utilized a very deep defect at $E_t = E_v + 1.05$ and $\sigma = 1 \cdot 10^{-15} cm^{-3}$. He also found that a interface layer with an affinity of $3.7 eV$ yielded the highest solar cell efficiency, reducing the recombination at the ZnO/Cu_2O interface due to a large lattice mismatch. A similar structure were investigated by Takiguchi [61], with the goal of reproducing the performance of a ZnO/AlZnO/Cu_2O solar cell. Takiguchi found that a χ similar to that of Cu_2O resulted in the best solar cell performance.

3.8.3 Simulation parameters

Silvaco Atlas does not contain default parameters for Cu_2O. The constant and variable parameters employed in the simulations for this thesis is summarized in table 3.8.1. .

Table 3.8.1: Parameters space used in Silvaco Atlas simulations in this thesis. The asterisks indicates Silvaco standard values. Cu_2O parameters are taken from Takiguchi [61].

Parameter	Cu_2O	Si
Thickness (μm)	0.5	2
Dielectric constant	7.9	11.8
Bandgap at 300K (eV)	2.1	1.08 *
electron affinity (eV)	3.2	4.17 *
N_c (cm^{-3})	$2.43 \cdot 10^{19}$	$2.8 \cdot 10^{19}$ *
N_v (cm^{-3})	$1.34 \cdot 10^{19}$	$1.04 \cdot 10^{19}$ *
electron mobility(cm^2/Vs)	200	1000 *
hole mobility (cm^2/Vs)	100	500 *
doping (cm^{-3})	p=$1 \cdot 10^{12}$	$n = 1 \cdot 10^{15}$
E_t (eV)	0.14	
N_t cm^{-3}	variable	
trap type	variable	
capture cross section (cm^2)	variable	

Oba et.al. identified an interface layer between an electrodeposited, epitaxial grown Cu_2O and (001) single crystal Si substrate. However, the thickness of this layer were about 2nm and identified as mostly SiO_2. Takiguchi [62] found evidence for a 1 nm thick SiO_2 interface layer for a reactive sputtered cuprous oxide film on c-Si substrate. The thickness of this interface layer is expected to be sufficiently small to sustain a large tunneling current in a real sample. In order to simplify the numerical model, no interface layers are simulated. Despite neglecting the interface layer, the significant band discontinuity is expected to affect the results. No advanced models enabling quantum tunneling is deployed, as no experimental technique utilized in this thesis can indicate the parameters needed for such models to be accurate. Carrier mobility is assumed artificially high in the cuprous oxide and is not in accordance with the presented Hall data, for the simple reason of idealizing the parameters not varied in the simulations.

4 Experimental procedures

4.1 Equipment used

Laser cutter: Cutting the substrates were done with a Rofin laser cutter, with a speed of 200mm/s, 32A current and execution counts of 150 and 20 for quartz and silicon substrates respectively.
Sputtering: A Semicore TriAxis magnetron sputter was used to deposit thin films, using circular targets with a 3 inch diameter. All depositions were performed with 400°C substrate temperature and a minimum pressure of 10^{-6} torr prior to deposition.
Thermal evaporator: Resistive heating and evaporation of Au and Al contacts were performed with a Balzers BAE 250 coating system. Prior to deposition a vacuum of minimum vacuum of 10^{-5} torr were achieved.
Profilometer: For thickness measurement of non-transparent films a Veeco Dektak 8 stylus profilometer were utilized.
Ellipsometry: A Woolam Alpha SE ellipsometer using wavelengths between 380 - 900 nm were used for transparent Cu_2O films on Silicon substrates. Kristin Bergum, University of Oslo, has developed the theoretical model for transparent thin films on Si substrates.
XRD: For XRD characterization were done with a Bruker AXS D8 Discover system using a Cu K_α source with $\lambda 1.5406$nm. 2Θ scans were performed from $20°$ to $80°$ with intervals of $0.004°$.
SIMS: Performed by Christoph Seiffert and Alexander Azarov at University of Oslo, using a Cameca IMS-7f.
Hall measurements: Hall measurements were performed on a LakeShore 7604, measuring carrier concentration, Hall mobility and resistivity in the temperature range 60 to 500°C. Contacts where soldered using In in a square configuration.
Capacitance measurements: The Agilent 4280A LCR meter has been used for impedance measurements, i.e. capacitance and conductance, with probe frequencies between 1kHz to 1MHz and dark ambient.
Current-Voltage: A Keithley 6487voltage source/picoammeter was used to measure current-voltage between -3 and 2 V in dark ambient.

4.2 Sample preperations

All samples were deposited on both amorphous, fused silica UV grade quartz and n-type poly-Si with a doping of $N_d \simeq 10^{15} cm^{-3}$. Quartz substrates were, after laser cutting, cleaned with the RCA1 and RCA3 steps followed by 10 minutes in piranha solution. Silicon substrates were cleaned with the full RCA procedure. All substrates were then dried with N_2 gas and stored. Immediately prior to deposition, Si substrates were subjected to a 10 s dip in HF, 2 min washing in DI water and then dried with N_2 gas.

Films on quartz samples were mainly used for Hall and XRD-measurements, while the silicon substrates were used for IV, CV and TAS characterization. All depositions were conducted with a $400°C$ substrate temperature. Measured samples are as-deposited with no annealing step performed on any sample.

4.2.1 Batch A

Martin Nyborg at University of Oslo has deposited Cu_2O thin films by reactive co-sputtering with Cu and Li doped targets. Two different targets were used, doped with either 1% and 0.01% Li. Oxygen flow was individually optimized for each sample, but found to vary from week to week. The total flow of constituted of O_2 and Ar were kept at 50sccm. Table 4.2.1 summarizes the different samples. Samples are numbered according to assumed Li doping, starting with no intentional doping in A0.

Table 4.2.1: Overview of the key deposition parameters for the reactive sputtered films.

Sample	P_{Cu}	P_{CuLi} (1% Li)	P_{CuLi}(0.01% Li)
A0	100W, DC	0	0
A1	100W, DC	0	50W, RF
A2	0	0	100W, DC
A3	100W, DC	10W, RF	0
A4	100W, DC	50W, RF	0
A5	0	100W, DC	0

4.2.2 Deposition with ceramic target

In addition to the reactive co-sputtering performed with the A samples, sputtering from a Cu_2O target were also performed. Although O_2 flow was varied in order to optimize samples, the total gas consisting of Ar and O_2 were kept constant at 50 sccm. Power over the target was 100W RF with depositions lasting 60 minutes.

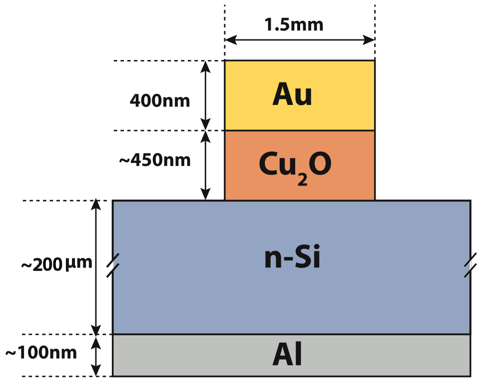

Figure 4.2.1: MESA diode of Cu_2O/n-Si, Au and Al contacts.

4.2.3 Diode processing

MESA contacts were created by depositing circular Au contacts, 1.5 mm in diameter and ~ 400nm thick, on Cu_2O. Samples were then etched for 10-15 s in a solution of 37% HCl 1:25 with DI water. 100nm thick Al contacts were then deposited by thermal evaporation, covering near the entire silicon back surface.

4.3 Error conciderations

Hall measurements

Two sources of error are considered in Hall measurements of carrier density, resistivity and mobility related to the relationship. Measurements are performed at varying field strengths, varying from 1-10 G. Results might vary with field strength. However, the relationship between contact size (c) and length between contacts l, i.e. the substrate length. The resistivity error is proportional to $(c/l)^2$, while carrier concentration and mobility shows contact errors proportional to c/l. Average size of contacts was found to be 1.1 mm, while the substrate was a square with diameter $10 \times 10mm$, which results in a error of 1.1% for ρ and 11% for μ and carrier density.

Elipsometry

Thickness of samples A0-A5 were measured with a theoretical model developed by Kristin Bergum for Cu_2O on Si substrates. This model also calculate error estimates based on the curve fitting to the theoretical model.

Profilometer

Thickness measurements with the stylus profilometer were performed on samples which were partly covered by Al foil during deposition. In order to get an error estimate, three measurements on different sections of the samples were performed.

IV, CV and TAS

Current-voltage were performed by averaging five measurements at each bias. Unless the current were near or under the detection limit, the relative error were found to be less than 0.02. Calculations of ideality factor, V_0, σ, E_t were performed from discrete data points through Arrhenius plots. The standard error from the linear fit of these points has provided the error estimates.

5 Results and discussion

5.1 XRD results

5.1.1 Batch A

Figure 5.1.1 show that the reactively sputtered films are polycrystalline. Further, the presence of the Cu_2O planes (111), (200), (220) and (311) is observed. Note the variation in preferred orientation of the different samples, with A0 and A1 showing a preference for (200) while A2, A3 and A5 is oriented more in the (111) direction. (220) is observed as a shoulder in A0-A4 and only visible as a distinct peak in A5. Furthermore, the XRD analysis show no evidence of any other phases or oxidation states of copper oxide other than Cu_2O. However, in samples A0, A1 and A3 a unidentified peak is present at $2\Theta = 33°$.

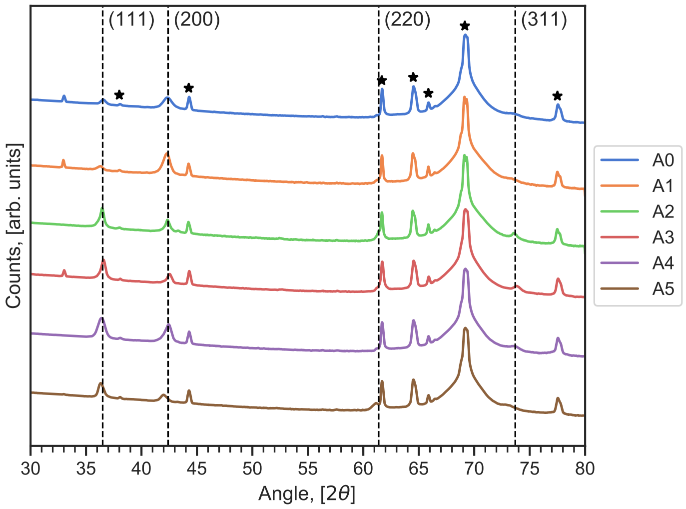

Figure 5.1.1: XRD results for thin films deposited by reactive sputtering on Si substrates. Background peaks (substrate and substrate holder) are marked with an asterisk.

5.1.2 Ceramic target

Optimalization of deposition parameters for thin films sputtered from the ceramic target were conducted by varying the O_2 flow, with increments of $0.1sccm$. All samples are polycrystalline Cu2O structure with the (111) and (200) planes dominating. O_2 flows $\geq 0.8sccm$ show the presence of Cupric Oxide (CuO) phase identified with the (-111) plane, while O_2 flows $\leq 0.3sccm$ contains grains of pure Cu (111) planes. Figure 5.1.2 show an increase in intensity for (200) Cu_2O planes with increasing O_2 flux, indicating a shift in preferred crystal orientation. At O_2 flux $\leq 0.4sccm$, (111) is observed to be dominant, but a small increase in intensity from (220) is also observed.

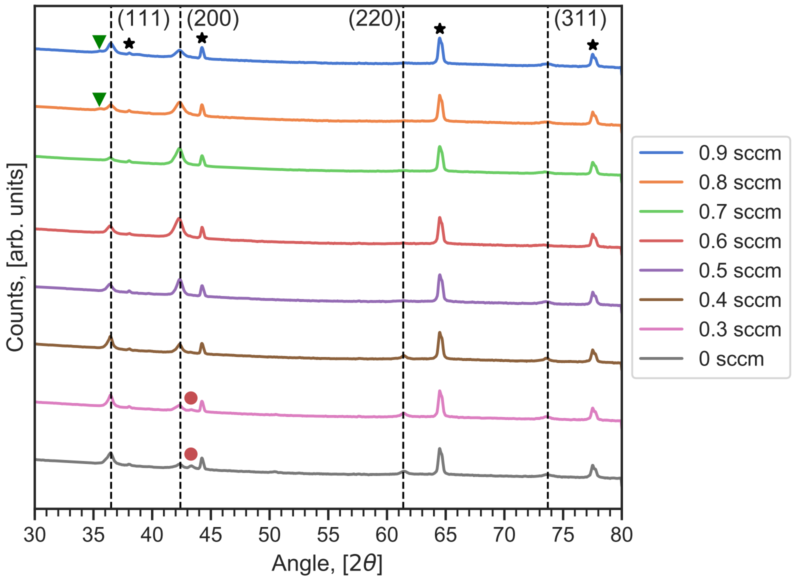

Figure 5.1.2: XRD results for the films sputtered from the ceramic target, measured on Quartz substrate. Asteriks indicate background signals. CuO (-111) is indicated by a green triangle, while Cu (111) is indicated with a red circle, y-axis is logarithmic.

5.2 SIMS results

5.2.1 Batch A

SIMS measurements show uniform concentration of Li in the samples deposited with a 1% Li doped target (A0,A3,A4 and A5). [Li] is found to increase with about one order of magnitude between each doped sample. The Li concentration of the un-doped sample A0 was below the detection limit of the system of about 10^{16} cm^{-3}.

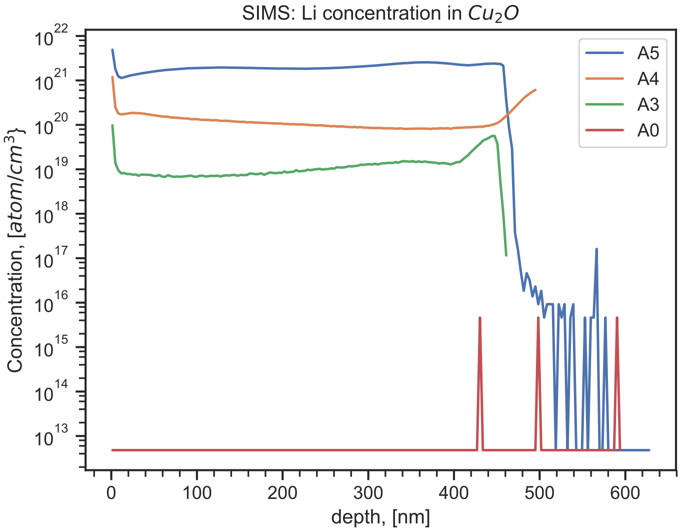

Figure 5.2.1: Li concentration in samples A0,A3,A4 and A5.

Samples A1 and A2 were measured at a later time than A0, A3, A4 and A5. This measurement is found to deviate from the expected values for A2 with over one order of magnitude. Furthermore, A0 and A3-A5 were re-measured together with A1 and A2. They show different Li concentrations compared to the original measurement, with up to one order of magnitude. The latest SIMS measurements, including the results for A1 and A2, are hence considered to be inaccurate. Due to the similarity in sputtering power with A4 and A5 described in table 4.2.1, A1 and A5 are expected to show Li concentrations around 10^{18} cm^{-3} and 10^{19} cm^{-3} respectively.

During the second SIMS measurement, concentrations of N,H and Al were also investigated. As mentioned above, the latter SIMS results appear unreliable. However, they do indicate a significant presence of impurities. A dominant concentration of H up to 10^{20} – 10^{21} cm^{-3} is suggested together with N concentrations of up to 10^{20} cm^{-3}. Aluminum concentrations are estimated between $10^{14} - 10^{18}$ cm^{-3}, while [Si] ~ 10^{18} cm^{-3}. The full results of these impurity concentration are found in appendix A.

5.2.2 Ceramic target

SIMS data acquired from a 300nm thick sample deposited with the ceramic target reveals a significant concentration of impurities, most notably a hydrogen concentration of 10^{20} cm^{-3}. Even though the target were not intentionally doped with Li, a uniform concentration of 10^{19} cm^{-3} is observed. Nitrogen and aluminum are both found to be present in concentrations ~ [Li].

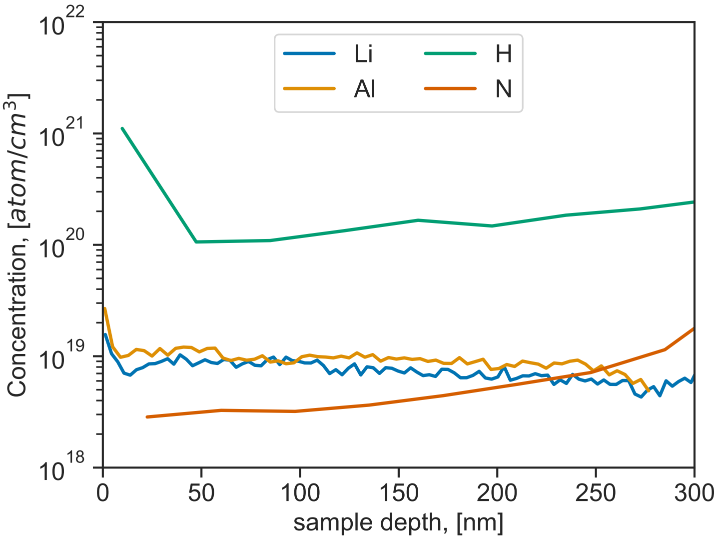

Figure 5.2.2: SIMS results for concentration of Li, N, H and Al in ceramic sputtered Cu_2O thin films.

5.3 Film thickness

Samples A0-A5 were deposited on 10×10mm Si substrates and the thicknesses deduced from ellipsometry are given in table 5.3.1. Not all samples created from ceramic target sputtering were transparent however, which is a requirement for the theoretical model used to fit the data. These samples were therefore measured with a profilometer. In the case of the sample deposited with O_2 of 0.4 sccm, a clear step between the substrate and film were not obtained.

Table 5.3.1: Cu_2O film thickness for batch A.

Sample	Film thickness (nm)
A0	470 ± 90
A1	500 ± 70
A2	485 ± 60
A3	550 ± 100
A4	560 ± 80
A5	530 ± 50

Table 5.3.2: Cu_2O film thickness for samples deposited from the ceramic target

Sample oxygen flow	Film thickness (nm)
0 sccm	763 ± 22
0.3 sccm	421 ± 23
0.5 sccm	420 ± 15
0.6 sccm	519 ± 20
0.7 sccm	412 ± 39
0.8 sccm	492 ± 16
0.9 sccm	436 ± 27

5.4 Room temperature Hall measurements

5.4.1 Batch A

Hall effect measurements prove that holes are the majority carrier in all samples. Li doping initially results in a lowering of carrier concentration compared to the undoped A0. By increasing Li doping, an increase in hole concentration is observed. In the case of A4 and A5, the increase in concentrations are 1 and 2 orders of magnitude compared to the undoped sample. On the other hand, Hall mobility is found to increas with doping, apart from A5.

Resistivity is a function of both mobility and carrier concentration. The change in carrier density is larger than the change in mobility for the various samples. Resistivity is hence found to increase as carrier concentration decrease. Worth noting is that A1 has a resistivity close to $10^4\ \Omega cm$, more than one order of magnitude larger than any other sample. This is a result of having both the lowest carrier concentration and Hall mobility.

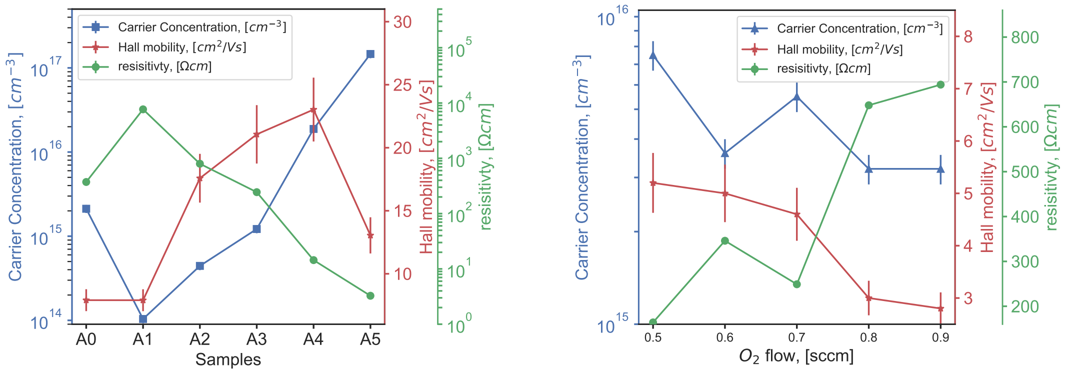

(a) Samples A0-A5, measured by Martin Nyborg.

(b) Samples deposited from ceramic target with O_2 flows ≥ 0.5 sccm.

Figure 5.4.1: Hall mobility, resistivity and carrier concentration. Comparing samples with various [Li] (a) and optimizing O_2 flow deposition for the ceramic Cu_2O target (b).

5.4.2 Ceramic target

Hall measurements were performed on films deposited from the ceramic target, in order to optimize sputtering conditions with regards to electrical properties. All samples are p-type, but at O_2 flows lower than $0.5 sccm$ the films were found to be highly resistive and Hall effects measurements were not possible. Majority carriers in these samples were not able to construct a hall voltage large enough to be detected when subjected to a variable magnetic field, either due to low mobility or low carrier density. With increasing O_2 flux, hall mobility is found to decline from 5.2 to 2.8 cm^2/Vs. Similar variation can be seen for hole concentration, where a drop from $7.5 \cdot 10^{15}$ to $3.2 \cdot 10^{15} cm^{-3}$ between 0.9 and 0.5 sccm can be observed. Due to high mobility and low resistivity, samples with O_2 flow of 0.5 sccm where chosen for further analysis and will be referred to as sample C for the remainder of the thesis.

5.4.3 Summary

Samples deposited with a ceramic Cu_2O target generally show a much lower mobility than the samples deposited from copper targets. Although expected to require less optimization, Hall measurements reveal that variations of 0.1 sccm O_2 flow in the sputtering from the ceramic target can significantly affect electrical properties. Carrier concentration in these samples varies with as much as 46%, revealing that carrier concentration, mobility and resistivity are dependent on the optimization process. Carrier concentrations in batch A are found to vary over 3 orders magnitude, with Li doping resulting in a an initial reduction of hole concentration. Whether the observed carrier concentration trends are due to increased compensation from donors or decreased acceptor state concentration is unclear.It is possible that not all samples A0-A5 are perfectly optimized, but this is not expected to have a significant impact on the observed trends in figure 5.4.1a.

5.5 Diode definition

Gold contacts with thickness ~ $100nm$ were initially deposited. These samples were subjected to JV, CV and TAS analysis. All samples show a high J_0, the highest doped sample two order of magnitudes higher than A3, the lightest doped sample at that time. In turn this resulted in rectification varying from 0.25 to 3.8 orders of magnitude. Furtermore, ideality factors of $n > 3$ were found for A0, A4 and A5.

A significant reduction in J_0 is found in all samples after the diode has been clearly defined to a MESA diode. Au contacts, ~ 400nm thick, where used as etching masks. Figure 5.5.1b provides further insight into the reason for this. Prior to the freeze out of carriers in Cu_2O, between 80 and 170K for the various frequencies, conductance is found to be very high and not close to 0 as is expected from theory. For diodes with a MESA structure as shown in figure 4.2.1, conductance is found to be near zero for temperatures related to C_0 and C_∞, as expected from the theory discussed in section 5.10. This indicates that carrier mobility in Cu_2O is sufficiently high to affect the diode area at elevated temperatures.

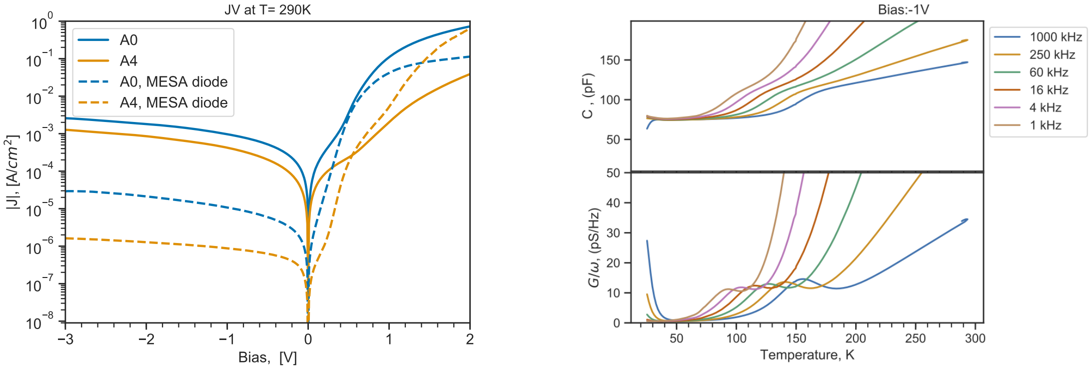

(a) JV for A0 and A4 comparing un-etched samples with MESA diodes. Note the significant decrease in J_0 and increase in linearity between 0 and 1V for the MESA diodes.

(b) Conductance and capacitance in A0 at -1V bias, showing a significant increase in G when acceptors are excited at high temperatures

Figure 5.5.1: Comparisson of J(V) (a) for un-etched samples and MESA diodes. TAS results for un-etched samples and MESA diode of A0.

5.6 IV

IV measurements were conducted on all samples at various temperatures in the dark. In the cases where multiple diodes survived the etching process, all diodes were measured with IV and the best selected for further analysis. The underlying parameters determining the selection criteria were low reverse current, the ideality factor and the degree of current rectification. Reverse current typically varied within 0.5 orders of magnitude. Some diodes showed a smaller ideal region in forward bias, resulting in variations of n of about ± 0.5. The aluminum back contact were coated with silver paste to ensure good electrical contact with the measurement stage. Comparison with measurements obtained without the silver paste revealed a significant reduction in series resistance effects on both reverse and forward bias current.

5.6.1 Silvaco simulations

Silvaco simulations were conducted employing an acceptor type defect with $\sigma = 10^{-16}\ cm^{-3}$ and a background doping of $10^{12}\ cm^{-3}$. All variations of N_t and E_t in figure 5.6.1 show the same ideality factor of $n = 0.9$. Although higher N_t results in a larger short current density, this effect is negligible as it varies in the range $1.1 - 0.9 \cdot 10^{-10} A/cm^2$. The effect of N_t is seen in the forward bias behaviour, as increasing N_t results in decreasing series resistance at $V > 0.5V$. By increasing E_t from $E_v + 0.14eV$ to $E_v + 0.2eV$ further lowers the current at forward bias. The IV curve for a defect free Cu$_2$O/Si heterojunction is identical to the lowest simulated trap density. Effect of doping trap density and trap energy level is thus expected to have a negligible effect on IV curves of real samples.

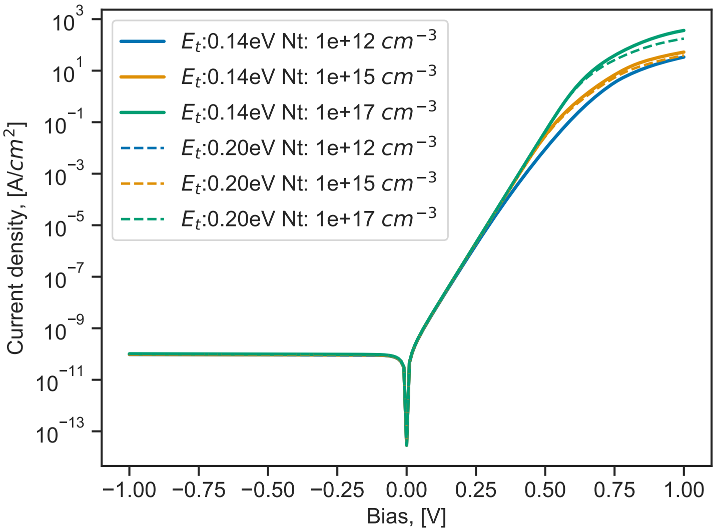

Figure 5.6.1: IV-simulations with Silvaco Atlas under dark conditions, T=290K and σ = $10^{-6}cm^{-3}$

5.6.2 Experimental results at 290K

Figure 5.6.2 reveal large variations in current-voltage behavior at temperatures close to room temperature. Highest reverse current density is observed in A5, with A0,A2 and C showing J_0 approximately one order of magnitude lower. Furthermore, reverse current in A1, A3 and A4 is significantly lower, indicating an reduction in recombination or shunting effects. No trend is observed in regards to Li doping levels.

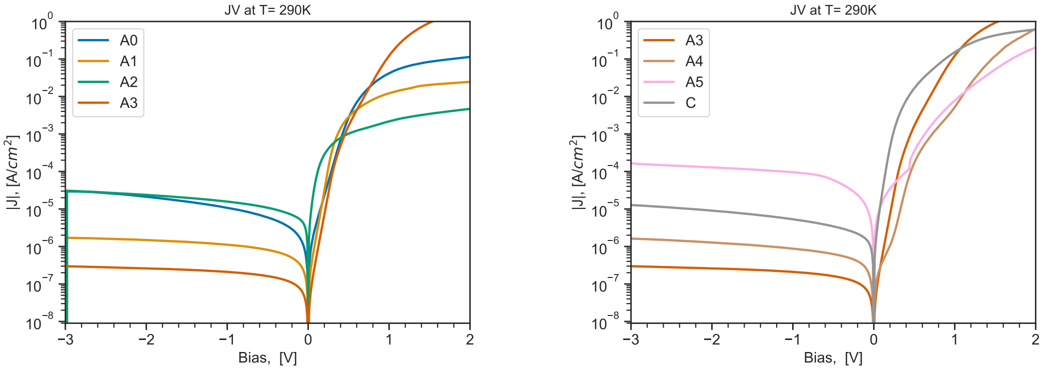

(a) Samples A0,A1,A2 and A3.

(b) Samples A3,A4,A5 and C.

Figure 5.6.2: IV-curves for all samples. As a reference, A3 is presented in both figures.

At bias>0.5V all samples are affected by series resistance and diverge from ideal behaviour. In addition to showing the two highest J_0, samples A2 and A5 is significantly affected by this resistance. Note that A5 is not showing a current density larger than J_0 before $V > 0.4V$, as compared to the more immediate rectification observed in the other samples. Similarly, A4 is also observed to show poor rectification at forward biases <0.1V. This effect is not observed in other samples, indicating that either optimization of deposition conditions or contact quality are dominating factors.

Ideality factors are calculated from linear fitting to the linear region at forward bias, with a minimum bias interval of 0.1V. Samples A1-A3 and C all show n<1.5 at 290K, while the higher doped A4 and A5 together with A0 show strongest deviation from ideal diode behaviour. Two linear regions are possible to discern for A4, indicating that two ideality factors dominate at different biases. At 200K these two samples are still less ideal compared to the lower doped samples, but to a lower extent. Ideality factors and rectification are both found to be less than reported by Lindberg, who reported rectification of 7 orders of magnitude and $n = 1.14$ for samples with similar fabrication and processing [63].

Table 5.6.1: Ideality factors and current rectification from IV at 290K. Rectification is measured between -1:1 V

Sample	n	rectification (orders of magnitude)
A0	1.9 ± 0.08	3.59
A1	1.3 ± 0.03	4.04
A2	1.6 ± 0.11	2.14
A3	1.4 ± 0.04	5.82
A4	2.0 ± 0.01	3.77
A5	2.8 ± 0.23	1.91
C	1.2 ± 0.03	4.46

5.6.3 Temperature dependence

In order to gain further insight into diode performance at lower temperatures, each diode were measured until the equipment accuracy limited further investigation. Figure 5.6.3 show the effect of temperature on selected samples. J_0 if found to decrease with temperature, indicating that mechanical shunt currents are not dominating. However, the various samples experience a reduction in J_0 at various rates. Both A3 and A1 show leakage currents $\leq 10^{-10} A/cm^2$ at 200K. On the other hand, A0, A2, A4 and C show a steady, but slower decrease in $J_0(T)$. However, A5 show little reduction in J_0 for temperatures < 200 and has a comparably high current leakage at all temperatures. These different responses of J_0 to a lowering of temperature could indicate that mechanisms leading to shunt currents influence the different samples in different ways. Variations in saturation current is also observed, although to a lesser degree. This results in a higher degree of rectification for all samples at lower temperatures.

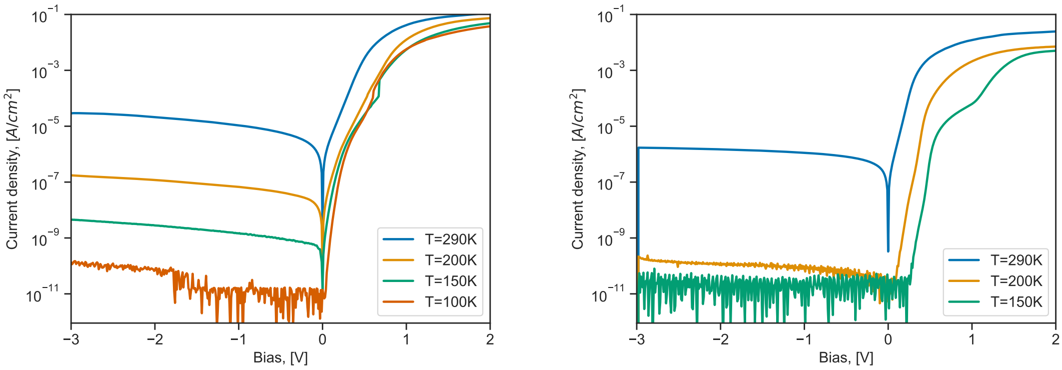

(a) Sample A0.

(b) Sample A1.

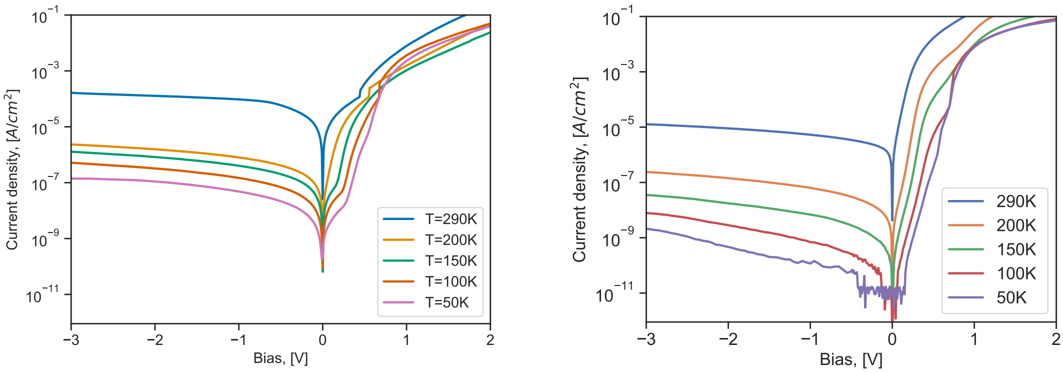

(c) Sample A5.

(d) Sample C.

Figure 5.6.3: IV curves performed at different temperatures. Samples A3 and A4 is found to behave similar to A1, while A2 is similar to A0 with regards to $J_0(T)$.

5.6.4 Au/n-Si Schottky Diode

For comparison, a Au/n-Si Schottky diode have been fabricated by depositing gold contacts on the same silicon substrate used for deposition of batch A. The Au/Si-Schottky diode is found to have an ideality factor of $n = 1.06$ at 290K and 1.12 at 200K. Rectification between -1:1V were found to be 5.7 and 7.9 orders of magnitude at the same temperatures. As temperature decreases, the presence of two linear regions with different gradients in forward bias is increasingly perceptible. This indicates that two different non-ideal mechanisms dominate at separate bias intervals. The simple, one diode model presented in equation 3.6 is hence inadequate to describe the current flow at lower temperatures.

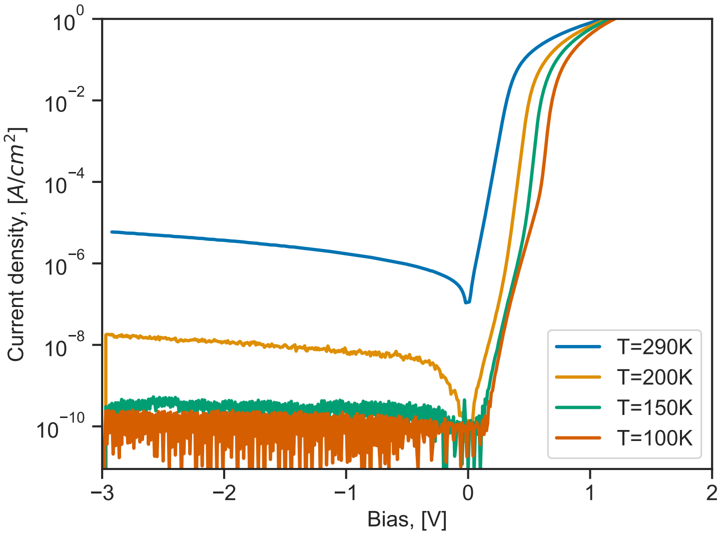

Figure 5.6.4: I(V) measurements for the Au/n-Si Schottky diode at 100-290K.

5.6.5 Summary

From the Silvaco simulations if was found that varying the trap density in the Cu_2O film have a negligible effect on the IV curve at room temperature. The variations observed for $I(V)$ in the physical samples are therefore not expected to be related to any eventual change in trap characteristics. The different reverse current densities are therefore predicted to be related to several different mechanisms not accounted for in the simulations. Whether this is related to interfaces, contacts or bulk properties is not possible to conclude.

Deposition conditions is indicated to play a role in diode quality. The ideality factors of A0 and A5 are two of the three highest observed at 290K. Simultaneously, A0, A2 and A5 have the lowest current rectification and the highest degree of current leakage at reverse bias. These samples were the only ones deposited exclusively with 100 W DC over the target, indicating that even co-sputtering with low RF power enhances the diode quality. At the same time, the presence of more than one linear region at lower temperatures indicate that several non-ideal mechanisms are present in A1 and C. No dependency of Li doping is observed in any of the trends.

5.7 CV

CV measurements were carried out on the same diodes as with IV, without moving the probe. All measured diodes were circular with a diameter of 1.5mm and simulated diodes has been scaled to the same area as the experimental diodes. Both simulations and experimental measurements were conducted with a 1MHz AC signal.

5.7.1 Simulations

Simulations were performed in order to gain insight into the effect of N_t, N_a, σ and E_t levels in Cu$_2$O. Silicon was simulated with no defects and $N_d = 10^{15}\ cm^{-3}$. The Cu$_2$O-layer included traps, specified to be acceptor type with an states close to the valence band. Their concentration, along with the acceptor doping concentration, were varied and found to have similar effect on both capacitance and band structure. The simulation model used is found in appendix E.

The highest concentrated state, either trap or acceptor, is found to dominate the electronic structure and capacitance measurements. As an example, acceptor doping of $10^{15}\ cm^{-3}$ does not affect the results if $N_t = 10^{17}\ cm^{-3}$. Therefore, the terminology of labeling Cu$_2$O as either p^+, p or p^- depends on the highest concentrated state. p^+ refers to either N_a or N_t equal to $10^{17}\ cm^{-3}$, p refers to the intermediate concentration of $10^{15}\ cm^{-3}$, while the concentrations p^- indicate acceptor state concentrations of $10^{12}\ cm^{-3}$. Exchanging the trap type from acceptor to donor resulted in C(V) data comparable to those from simulations with no traps.

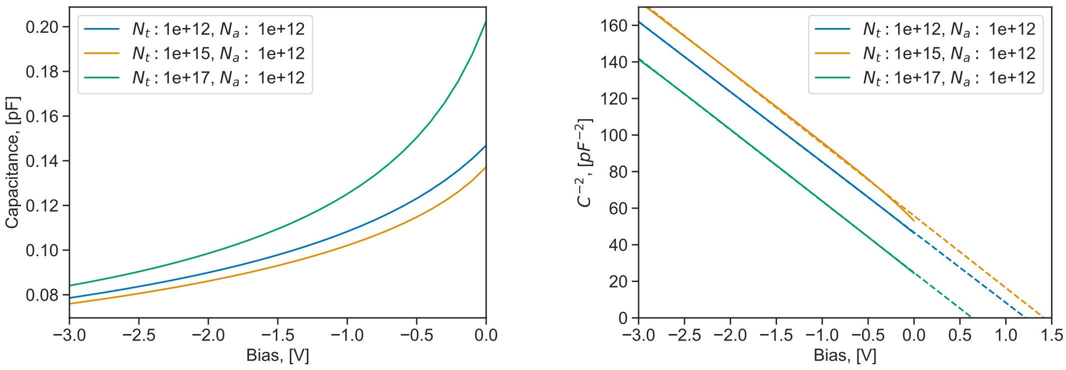

(a) C(V)

(b) $C^{-2}(V)$

Figure 5.7.1: C(V) and $C^{-2}(V)$ for $N_a = 10^{12}\ cm^{-3}$ and $N_t = 10^{12} - 10^{17}\ cm^{-3}$, showing effects of p^+,p and p^- characteristics for Cu$_2$O. Simulated at T= 290K and $E_t = E_V + 0.14eV$. The stipulated lines in (b) are extrapolated from the simulated data to reveal V_0.

Increasing the capture cross section was found to have a negligible effect on capacitance for $\sigma < 10^{-12}cm^2$. Thus, all other simulations were conducted with $\sigma = 10^{-16}cm^2$. Figure 5.7.1 illustrates the change with various degree of acceptor concentrations in cuprous oxide. Capacitance of the junction is observed to increase in the order of $p^+ > p^- > p$. Both Schottky-Mott and conventional C(V) plots reveal that capacitance observed from p and p^- diodes are closely related, while p^+ conditions yields noticeably different results. Both p and p^- show a noticeable higher built in voltage V_0, see table 5.7.1 and the stipulated lines in figure 5.7.1b. Similar trends are seen when E_t is increased to $E_v + 0.3eV$, but with less difference between p and p^-.

Table 5.7.1: Values of built in voltage found from simulations. Note that the built in voltage is largest when Cu_2O is fully depleted, as expected from theory.

diode characteristic	$V_0, E_t = 0.14,$	$V_0, E_t = 0.3,$
p^+n	0.6 V	0.6V
pn	1.4 V	1.4V
p^-n	1.4 V	1.1V

An explanation for these trends can be found in the band structure in figure 5.7.2. Both p and p^- conditions results in a fully depleted Cu_2O layer. This means that any response of charge carriers to the AC signal will come from the silicon layer, not from Cu_2O. On the other hand, p^+n diodes show a depletion region almost entirely in the silicon layer. The depletion region is also noticeably larger in Si in the case of a p^+n junction than p^-n.In either case, changing bias results in a growth in depletion region in Si and not in Cu_2O. Therefore, calculating effective carrier concentration from equation 2.38 for every combination of E_t, N_a and N_t returns the ionized donor concentration of Si.

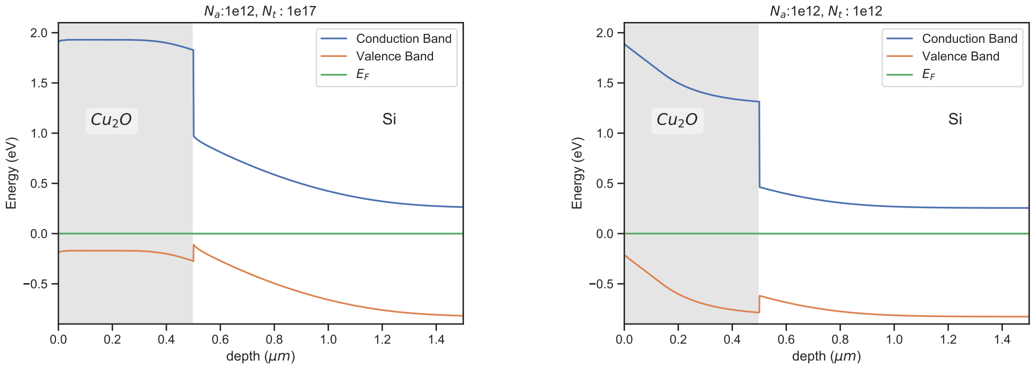

(a) Band diagram for $N_t = 10^{17}\ cm^{-3}$.

(b) Band diagram for $N_t = 10^{17}\ cm^{-3}$

Figure 5.7.2: Band diagrams at equilibrium conditions and 290K. The background doping of Cu_2O were $N_a = 10^{12}\ cm^{-3}$, with trap concentrations $N_t = 10^{17}\ cm^{-3}$ (a) and $N_t = 10^{12}\ cm^{-3}$ (b).

5.7.2 Experimental results at 290K

Figure 5.7.3 reveal little difference in capacitance between the samples. The undoped samples A0 and C, together with the highest doped sample A5, show the highest capacitance at -3V of 0.11pF. On the other hand, A3 is found to have the lowest capacitance at any reverse bias. If an abrupt p^+n junction is assumed, this relates to depletion layers of approximately $1.6\mu m$ for A0 and $3.1\mu m$ for A3 at -3V. Note that the C(V) curve for A5 increases far more rapidly than the other samples, even showing an inflection point around V=-0.5V.

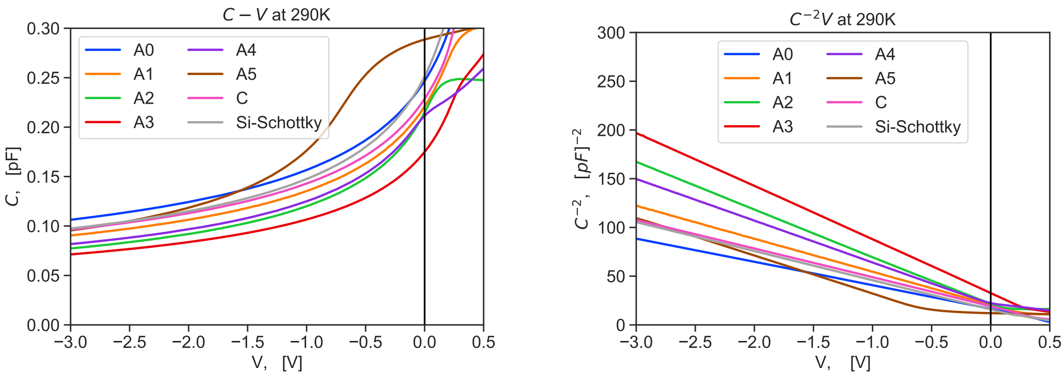

(a) C(V)

(b) $C^{-2}(V)$

Figure 5.7.3: C(V)(a) and Mott-Schottky plot (b) at 290K.

The Mott-Schottky plot show good linearity of $C^{-2}(V)$ in reverse bias, apart from the case of A5. This indicates a uniform doping concentration in the region(s) contributing to capacitance. Furthermore, the slope gradient of the Au/Si Schottky diode is similar to all other samples, again except for A5. Calculated values of N_{eff} were obtained from equation 3.8 by assuming an asymmetrical diode. N_{eff} is found to be uniform and in the range of $0.7 - 1.1 \cdot 10^{15}\ cm^{-3}$, which corresponds to the value of $N_{eff} = 1.1 \cdot 10^{15} cm^{-3}$ extrapolated from the Au/Si- Schottky diode.

Furthermore, the built in voltage at 290K is found to be <0.67V, see table 5.7.2. Due to the deviation from ideal behavior, extracting the built in potential for A5 is not possible.

Table 5.7.2: Built in voltage at 290 K. Extrapolating V_0 from A5 were not possible from the data.

Sample	Built in Voltage V_0, (V)	Sample	Built in Voltage V_0, (V)
A0	0.67	A4	0.48
A1	0.62	A5	NA
A2	0.39	C	0.47
A3	0.59	Si-Schottky	0.52

5.7.3 Low temperature measurements

By lowering temperatures to 200K and 150K, A5 shows linear behavior in Mott-Schottky-plots. A decrease in reverse bias capacitance is additionally observed in all samples. Apart from this, there is no significant change when decreasing temperature to 200K and 150K. The decrease in capacitance is further reflected in increased values of V_0. However, the gradient is largely unchanged and N_{eff} still correlates with the results obtained from the Au/Si Schottky diode. $C(V)$ and Mott-Schottky-plots for 200 and 100K is found in appendix C

The Au/Si Schottky diode does not experience a large increase in built in voltage, as is observed in samples A0-A4 and C. This large increase is therefore attributed to the a depleted Cu_2O layer and is observed to occur at different temperatures for the various samples. However, the built in voltage of A5 never exceeds that of the Schottky diode.

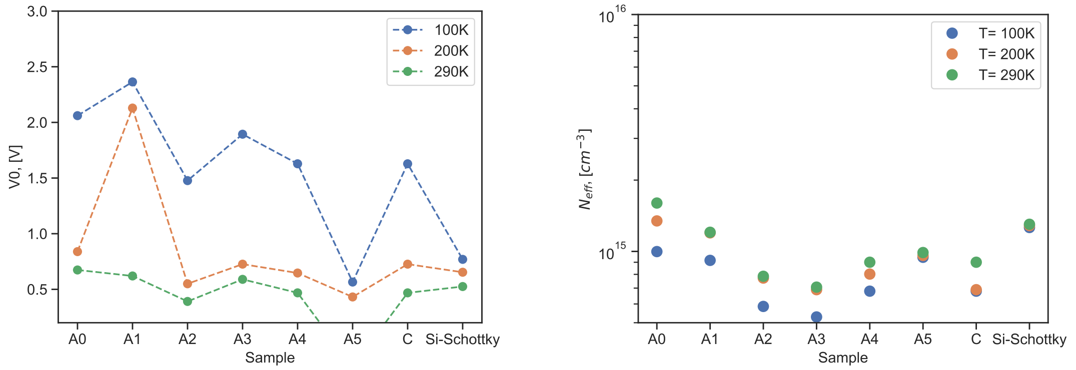

(a) Built in Voltage at 290K

(b) Apparent doping concentration, N_{eff}

Figure 5.7.4: Built in voltage (a) and N_{eff} (b) at 290, 200 and 150K.Overall V_0 increase with decreasing temperature, while the change in N_{eff} is negligible.

5.7.4 Summary

The simulated results is found to correspond with the data obtained experimentally, both with regards to capacitance at reverse bias, built in voltage and the calculations of effective doping concentration. On the other hand, non-ideal phenomenas like interface defects and leakage current are expected to influence the experimental data.

At 290K all samples show $V_0 \leq 0.67$ at 290K. Compared to the simulated values, this is expected to correspond to p^+n diodes. A shift to $V_0 > 1.5$V is observed at lower temperatures in all Cu_2O samples, except for A5. This is attributed to depleted Cu_2O layers. In accordance with trends from the simulations, no significant change where found in the slope of $C^{-2}(V)$, regardless off temperature and thus p^+ or p^- characteristics of Cu_2O. The calculated values for N_{eff} in the Cu_2O:Si diodes were found to correspond to N_{eff} in the Au/Si Schottky diode.

5.8 Discussion of diode characteristics from IV and CV

When temperature decrease, the saturation current density at forward bias decreases. This can in part be attributed to poorer conductivity of the metal contacts. However, the reduction in saturation current as temperature decrease is observed to be less severe in the Schottky diode. This indicates that the both the Cu_2O and Si layers experience higher series resistance. Reduced carrier mobility, as shown from Hall measurements, is expected to contribute to this.

The Schottky diode show a clear presence of two dominating ideality factors at lower temperatures, each dominating a small part of the ideal region in forward bias. Sample A5 and C in particular show the same tendency, while samples like A0 and A1 does not. Utilizing a diode equation with only one ideality factor is therefore a poor approximation. As the ideality factors of A4 and A5 are ≥ 2 and found at higher forward bias than in the other samples, it could be speculated that quantum mechanical tunneling affects these junctions to some degree. On the other hand, different mechanisms contributing to n>1 are expected to be present simultaneously. Another interpretation of n changing with V_a at lower temperatures could be linked to trap recombination within the junction and interface quality. Samples sputtered with 100W DC power and no yield from RF power sources, i.e. A0,A2 and A5, all show among the highest ideality factors.

The underlying physics giving rise to the variation in J_0 at 290K is unclear, but numerous effects may contribute. Although J_0 is expected to decrease with T even in the ideal case, due to the lower thermal energy of minority carriers, mechanisms not described by ideal theory are expected to contribute. A conductive edge circumventing the pn junction, conduction along grain boundaries and quantum mechanical tunneling are all examples of phenomenas expected to increase J_0. Conduction through the diode edges are expected to be negligible affected by temperature and can thus be ruled out as the dominant contributor to shunt currents in all samples. However, the high J_0 and low variation with temperature between 200 and 50 K in A5 indicate the presence of significant shunt currents, even allowing for the possibility of parallel conductance through grain boundaries or diode edges. All other samples show J_0 with more decisive dependency of temperature, although with varying degree of current leakage.

A5 is found to deviate from this trend. At 290K, the step behaviour of $C^{-2}(V)$ near 0 bias can be explained by deep interface states. As band bending is reduced, they are expected to be ionized. At lower temperatures, a significant leakage current is observed at both high and low temperatures. This could explain why, at 200 and 100K, V_0 values for A5 and Au-Si Schottky is comparable. It is speculated that the electrical potential of the Au contact is connected with the silicon substrate through this leakage current, resulting in the observed built in potentials.

5.9 Temperature Dependent Hall

Deep states can have profound effects on electrical performance of devices. The study of deep states and their effect on carrier concentrations and mobility is the focus for the Temperature Dependent Hall (TDH) measurements presented in the following section. Cuprous oxide films measured with TDH were deposited on quartz, simultaneously as the samples deposited on silicon substrates as described in section 4.2. All samples were measured in two separate temperature ranges, except for A1 which were only measured for low temperatures. First, low temperature Hall measurements were conducted while cooling from 300K. High temperature measurements between 300 and 500K were subsequently performed, thus avoiding annealing effects before the low temperature measurements. Martin Nyborg has performed all measurements. Sample C has not been subjected to TDH measurements.

Increasing temperature results in higher hole concentration, as evidenced by figure 5.9.1. From equation 2.12 and table 3.8.1 an intrinsic carrier concentration in Cu_2O of only $n_i \simeq 10\ cm^{-3}$ is expected at room temperature. The observed carrier concentrations are hence caused by ionized acceptor states.

A1 is found to have consistently the lowest $p(T)$ at the temperatures it was measured, a reduction of about one order of magnitude compared to A0. With increasing Li doping, carrier concentration is found to increase. However, A2 and A3 still show suppressed carrier concentrations compared to the undoped A0 sample at all temperatures. This indicating either a higher activation energy or lower acceptor concentrations. Note the particular large increase in carrier concentration from A4 to A5 at lower temperatures than 300K. On the other hand, increasing the temperature seemingly result in carrier densities of A2, A3, A4 and A5 converging towards the same density. Annealing effects are expected at high temperatures, which in turn is could influence carrier concentrations.

Hall mobility for all samples are found to decrease with decreasing temperature, from a peak at 230-250K. Peak mobility was found to be between 9 and $10.2 cm^2/Vs$ for all samples. Furthermore, a discrepancy between the sample regarding the lowest measurable temperature is also observed. This is seen in connection with both decreasing mobility and carrier concentration. Most noticeable is A1, which was only possible to measure down to 230K. As a consequence of this and instrumental limitations, further investigations of this sample at high temperatures were not conducted.

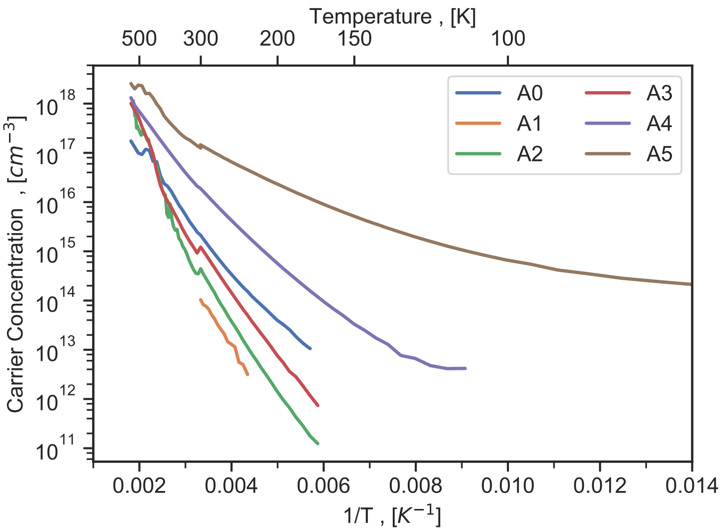

Figure 5.9.1: Hole concentration as a function of $1/T$.The abrupt change in $p(T)$ at 300K for A2, A3 and A5 is attributed to the transition between high and low temperature measurements.

Increasing temperature is expected to eventually produce a plateau where all acceptors are ionized and no further holes are excited. Without this, determining density of acceptor states is highly speculative. For A4 and A5 at low temperatures there seems to be an observable transition between two different linear regions. Extrapolating this for A4 yields an estimate concentration of the shallowest state of approximately $10^{13}-5\cdot 10^{14}\ cm^{-3}$. Correspondingly numbers for A5 is estimated at $10^{16}-10^{17}\ cm^{-3}$.

A theoretical model employing two different defects were used to calculate activation energy from the Arrhenius plot in figure 5.9.1. The slopes in the Arrhenius plot shown in figure 5.9.1 is observed to be non-linear for all samples measured over a larger temperature range than 100K, which could indicate the presence of more than one acceptor state. At

Activation energies higher than $E > E_v + 0.3$eV is observed in A0,A2,A3 and A5 and are categorized as E3. This category is not intended to refer to one singular state, but rather refers to deeper states that is not consistently observed across the samples. In the case of As the state both A2 and A5, E3 is close to E2 and it is somewhat unclear if this state should be classified as E3 or E2. Located between $E_v + 0.18$ and $E_v + 0.26$eV, E2 is observed in all samples except A5. This , together with A4 are the only samples where the presence of the shallow state E1 is observed. The limited data at low temperature for A0,A2 and A3 likely inhibit the observation of E1. Extracting reliable activation energies for A1 were not possible due to the limited temperature resolution of $p(T)$.

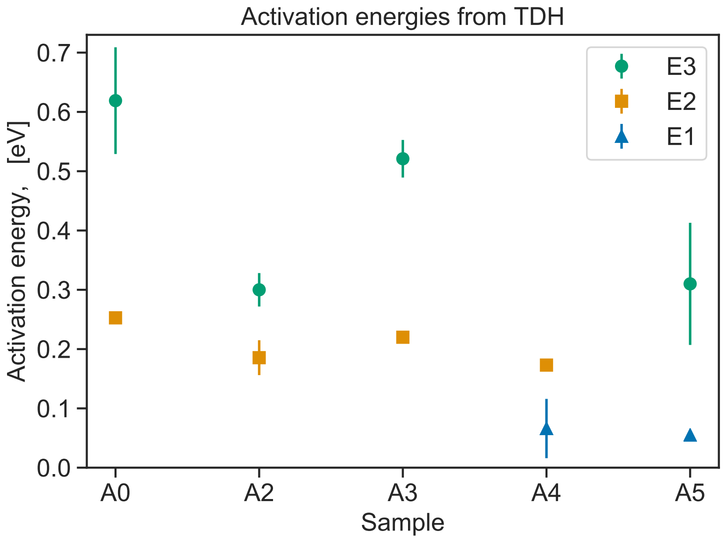

Figure 5.9.2: Activation energies from TDH measurements. Error margins are extracted from standard error of fitting.

Carrier concentrations from Hall measurements are a result of thermally excited carrier concentrations, compensated by donors. This limits the accuracy of the extrapolated values for activation energies and the density of the electrically active states, by affecting fitting parameters of the theoretical model. Additionally, low temperatures are required in order to observe low energy states if high temperature measurements are dominated by states with higher density and activation energy. Consequently, not all acceptor states are expected to be observe .

5.9.1 Effect of Li doping on carrier concentrations

Li doping with concentration $< 10^{19}\ cm^{-3}$ results in reduced hole concentration by one order of magnitude at temperatures between 300 and 200 K, This indicate the suppressing of acceptor states, possibly the v_{cu}^{split} expected from *ab inito* studies [19].

Increasing the [Li] concentration results in an increase of carrier concentration, which exceeds the concentration in pure Cu_2O when $[Li] \geq 10^{20}$. However, this increase is not linear with [Li]. This could indicate that one or several new states contribute to excitation of holes, assuming that lithium has subdued the main hole generation mechanism in undoped Cu_2O films. The chemistry of lithium atoms that do not compensate copper vacancies are largely unknown. Interstitial Li is expected to contribute to electron generation, but to what degree Li is found as a free interstitial is impossible to determine from measurements.

SIMS measurements indicate a significant presence of N in all samples, known to act as a shallow acceptor when it occupies an oxygen site [44]. However, Hall measurements does not reflect the high concentration of shallow acceptors. We attribute this to the high concentration of compensating donors, such as Al or H.

All samples display very high hydrogen concentrations, ~ $10^{20} - 10^{21}$ cm^{-3}, which increase the defect chemistry complexity . Hydrogen has potential to modify the structure by bonding to different sites. In many materials the stability of the bond is determined by E_F, expressing the amphoteric nature of H. This often leads to H compensating the majority carriers [39]. Interestingly, the observed increase of hole concentration in A4 and A5 than what is observed for A1-A3. SIMS assesses that both A4 and A5 have a Li concentrations comparable to or higher than [H]. It is only possible to speculate as to the mechanism, but if a Li bonds with H to form a(LiH) complex this is expected to reduce charge compensation from hydrogen. These samples are simultaneous the only samples were the shallowest acceptor states is observed, further indicating that these samples are less compensated. Additionally, the non-linear behavior found in the Arrhenius plot of figure 5.9.1 could be attributed to H changing configuration from donor to acceptor sites. The E_F is expected to control the amphoteric nature of H, but higher kinetics at elevated temperatures could also influence an eventual configuration change.

5.10 Thermal admittance spectroscopy

Thermal admittance spectroscopy measurements were conducted to categorize deep states in Cu_2O. To help understand the results and the effect of E_t, N_t and σ, Silvaco simulations were conducted. During simulations a temperature independent σ was assumed, along with a defect free n-type Silicon layer and ohmic back contact. Unless otherwise stated, the acceptor trap was located at $E = E_v + 0.14eV$ and the background doping of Cu_2O were 10^{12} cm^{-3}. Due to convergence issues during the numerical iteration process, most simulations were not able to go lower in temperature than 70K.

5.10.1 Silvaco simulations

Effect of capture cross section

Figure 5.10.1 show the effect of varying σ between 10^{-12} and 10^{18} cm^2, while N_t is kept at 10^{18} cm^{-3}. As expected from theory, the inflection point of the capacitance v temperature slope corresponds to the peaks in conductance. A smaller capture cross section is found to result in a higher temperature where these conductance maximums are observed, as can be observed in figure 5.10.1b. At the higher temperatures, the peak is broader and lower, resulting in a less abrupt transition from C_0 to C_∞ at high and low temperatures respectively. It is further observed that decreasing σ below $10^{-16} cm^2$ has little effect , but this is likely related to the resolution limitations in the numerical model. A shoulder is observed between 130 and 140K in the conductance of samples with $\sigma = 10^{-12}$ and $10^{-14} cm^2$. Numerical resolution of the model is believed to cause this, as it is not present in simulations were the defect free layer is redefined from Si to Cu_2O.

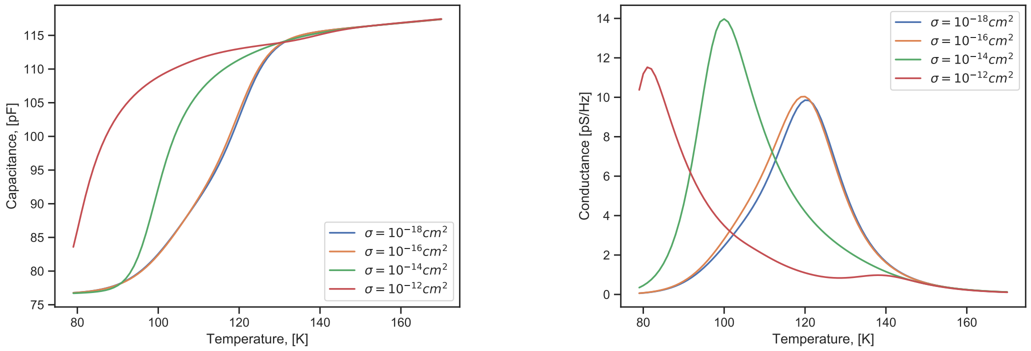

(a) Capacitance.

(b) Conductance

Figure 5.10.1: Comparing 1Mhz frequencies from TAS simulations with various σ-values and $N_t = 10^{18}\ cm^{-3}$. Numerical convergence were not obtained for temperatures<77K.

Effect of trap density

The same trends observed for increasing σ is seen for N_t: freeze out temperature increase at high N_t, simultaneously as the conductance peaks widens. A widening of G/ω peaks is equivalent to increasing the temperature range needed to transition from C_0 to C_∞. Trap concentrations $\leq 10^{15}\ cm^{-3}$ are found to return values capacitance and conductance values corresponding to the results from simulations of trap free Cu_2O layers.

Although the trap concentration varies with several orders of magnitude, the drop in capacitance,ΔC, is the same across iterations. This is because all simulated values for N_t are high enough for an abrupt p^+n junction at high temperatures, while the SCR streches all of the Cu_2O layer at temperatures where carriers have frozen out. In contrast to varying σ, the lowest doped sampled show a marginally higher conductance peak.

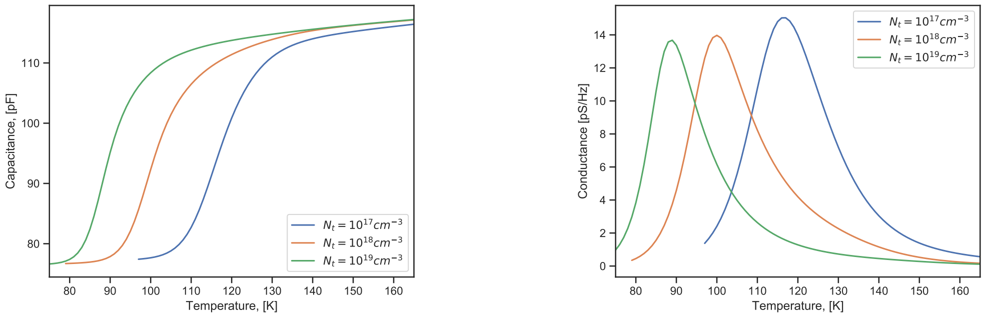

(a) Capacitance.

(b) Conductance

Figure 5.10.2: Comparing 1Mhz frequencies from TAS simulations with various N_t-values and $\sigma = 10^{-14} cm^2$

Simulations with higher background Cu$_2$O doping were also performed. They show that if $N_a << N_t$, any increase in background doping leads only to a minor increase in the width of conduction peaks.

Effect of energy level

Varying the trap energy level resulted not surprisingly in a significant increase in inflection temperature. Keeping trap concentration and capture cross section constant at $N_t = 1e19\ cm^{-3}$ and $\sigma = 1e-16\ cm^2$, a shift in inflection temperature for the 1MHz AC signal is observed. For traps with activation energies of $E_t = E_v + 0.1$ and $E_t = E_v + 0.3$, this temperature shift is from 64K for to 176K. Further, ΔC was observed to be the same, as well as the values of C_∞ and C_0. The depletion region in Cu$_2$O at temperatures well below the freeze out temperature, is however observed to be different. Due to a mismatch between the work function of the Au top contact and Cu$_2$O, a depletion region in Cu$_2$O is found to originate from both the Au:Cu$_2$O and Cu$_2$O:Si junctions when $E_t < E_v + 0.3$. In figure 5.10.3 this is reflected by an initial increase in conduction band energy between 0 and 0.1 μm at 63K. However, the subsequent decrease in energy suggests that the entire Cu$_2$O layer is depleted. This reveals a limitation of the simulation model, as it does not account for quantum mechanical tunneling assumed to occur at the Au/Cu$_2$O junction.

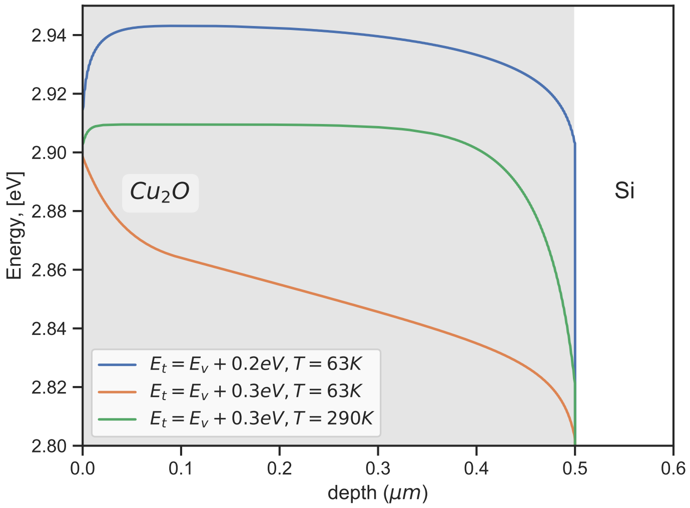

Figure 5.10.3: Simulated conduction band in Cu$_2$O at 290K and 63K, at -1V bias. Cu$_2$O is fully depleted at 63K for both $E_t = E_v + 0.2$ and $E_t = E_v + 0.3$eV. The simulated structure is with $N_t 1e19\ cm^{-3}$ and $\sigma = 1e - 16\ cm^2$. Note that neither bands at 63K show a energy with depth, while at 290K the band is flat until $0.35\mu m$.

5.10.2 Experimental results

All experimental measurements were conducted while heating the sample with a rate of 4K/min and at constant reverse bias of $-1V$. The AC test frequency superimposed on this DC bias had an amplitude of 30mV and frequencies were varied from 1kHz to 1MHz. Slower heating rates were found to have little to no effect on the results. Attempting to probe deeper into the Cu$_2$O layer with a bias of up to $-5V$ resulted only in lower values for capacitance and conductance, which can be related to an increase of SCR width primary in the substrate.

During the etching process, several of the diodes on a sample were often either damaged or destroyed. However, four diodes on a single A4 sample survived the etching. These have been measured in order to gain insight into eventual uniformity issues across the sample. Furthermore, these diodes provide information about variation in data related to specific diodes and not different samples. Freeze out temperatures were the same for all diodes on A4 . Trap activation energies and σ were thus found to deviation within uncertainties from the standard error of linear fitting. While ΔC remained unchanged , values of C_∞ and C_0 were found to vary with 37 and 44pF respectively. This deviation is equivalent to a relative increase of 56% and 38% for the diode with lowest capacitance. Measurements of conductance is found coinciding with this trend, where the diode with highest capacity show an overall higher conductance at any temperature. Hence, diodes with the highest capacitance also had the largest degree of leakage.

Figure 5.10.4 showcase both conductance and capacitance for A2 and A0. For the higher frequencies, A0 is found to have a profound shoulder at high temperatures on the G/ω peak, indicating the presence of an additional state. This shoulder is observed as a less abrupt change in capacitance .As the shoulder diminishes at lower frequencies, it is suspected that the two traps show similar values for f_t at lower temperatures.

Differences in capacitance between the difference frequencies, at both the C_0 and C_∞ plateau, are observed to be negligible in A1,A2 and A3, but not in A0 and A4. This is attributed to higher conductance at these temperature intervals. All samples show either a constant values or a decrease in $\frac{G}{\omega}\Big|_{max}$ with decreasing frequency, suggesting series resistance has little influence on the results. Furthermore, conductance is observed to increase significantly for the low frequencies as temperature is elevated beyond 220K.

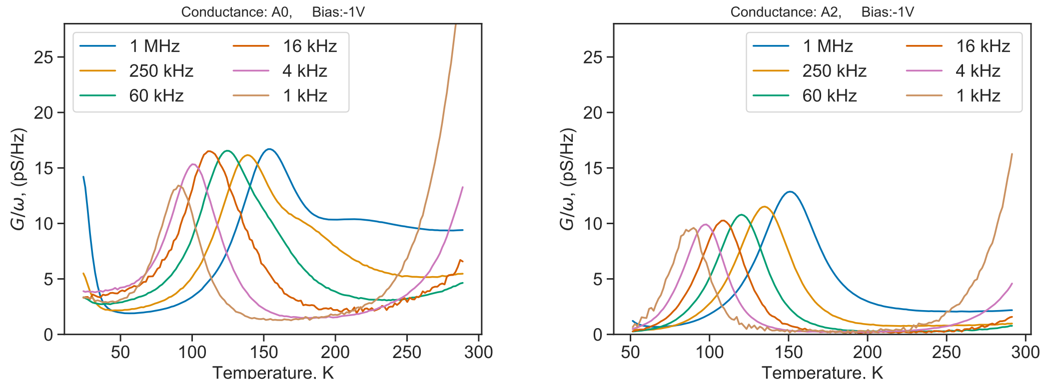

(a) G/ω for A0 (b) G/ω for A2

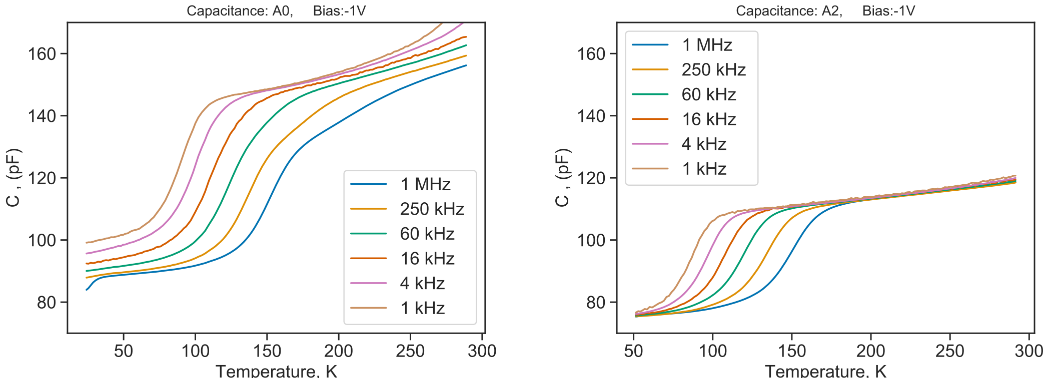

(c) Capacitance as a function of T for A0 (d) Capacitance as a function of T for A2

Figure 5.10.4: TAS measurements. The conductance per angular frequency reveals a shoulder in A0 (a) at high frequencies, a behavior not observed in A2. Capacitance in A0 (c) is higher than in A2(d) at all temperatures. Similar figures for samples A1,A3,A4,A5, C and the Au/n-Si Schottky diode is found in appendix D.

Comparison of samples

A comparison of capacitance and G/ω at 1MHz frequencies for all samples is shown in figure 5.10.5. Worth noting is the exception of A5. While measuring this sample, no plateaus in $C(T)$ where found and a consistent leakage conductance was observed. A5 is thus exempt from further discussions. The Au/Si Schottky diode was also measured and found to have a consistent capacitance plateau at 140 pF, before carriers freezing out between 30 and 20K for the various frequencies. The sharp decrease in capacitance for the Cu$_2$O samples $T < 30K$ is therefore attributed to donor freeze out in silicon. Substrates for A0-A5 samples were from the same wafer, but in the case of sample C a different wafer was used, although from the same batch.

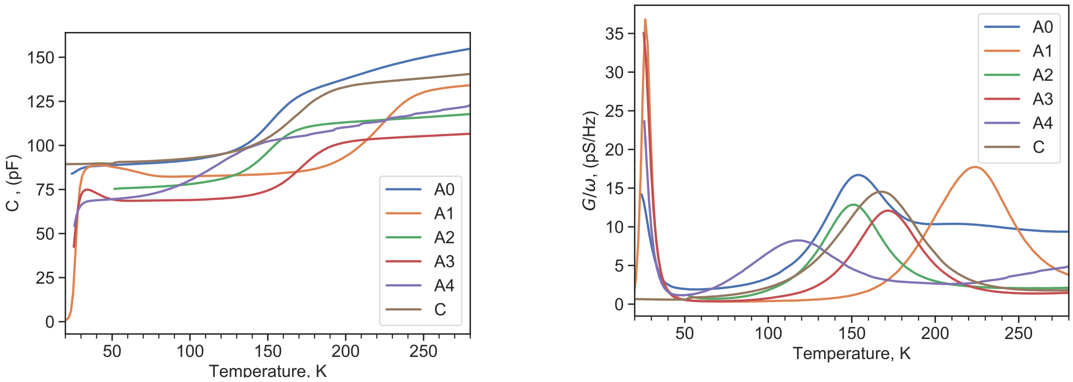

(a) (b)

Figure 5.10.5: Comparing capacitance (a) and conductance per ω (b) of the various samples found at 1MHz frequencies.

The two undoped samples A0 an C show similar freeze out temperatures as in A2 and A3. The highest doped sample that were possible to measure, A4, has a significantly lower inflection temperature for capacitance at 110 K, while A1 inflicts already at 225K. A4 further shows a higher conductance at temperature>225K than the samples showing comparable $C(T)$ profiles. This has been linked to a second trap, which will be discussed in section 5.10.3.

Variations in capacitance at the plateaus for C_0 and C_∞ were found to vary with 35 and 24 pF respectively. Interface states are suspected to contribute to this variation, but altogether this variation is less than what is observed between the different four diodes on A4. Despite this, $\frac{\Delta C}{C_\infty}$ is found to be 0.6 for A1 and $\simeq 0.5 \pm 0.02$ for all other samples. Apart from the second state in A4 at T>200K, only one trap that is unambiguously related to Cu$_2$Ois observed to freeze out . From this Cu$_2$O is expected to be completely depleted after the freeze out and accurate knowledge of N_a is not possible.

The width of a $\left.\frac{G}{\omega}\right|_{max}$ is expected to increase naturally if the peak is observed at higher temperatures, due to a higher thermal energy and thus higher probability of carrier excitation. Therefore, the width of the conductance peaks of samples C and A0-A3 indicates a similar energy distribution for the observed defect. However, the peak of A4 is considerably wider and found at a lower temperature, indicating that several defects of similar energy and capture cross section is present.

Arrhenius analysis

Arrhenius analysis has been performed with the assumption $f_t = 2e^{th}$. Figure 5.10.6 show that a plot of $\ln e^{th}/T^2_{inflection}$ v $1/T_{inflection}$ is not a perfect straight line in all cases. This deviation from linearity is most notable for C and A4. This indicate a more complex model for Cu_2O than a simple, ideal defect state and that $f_t = 2e^{th}$ could be an imprecise presumption. Only σ is affected by this assumption, as it shifts all values on the y-axis in figure 5.10.6.

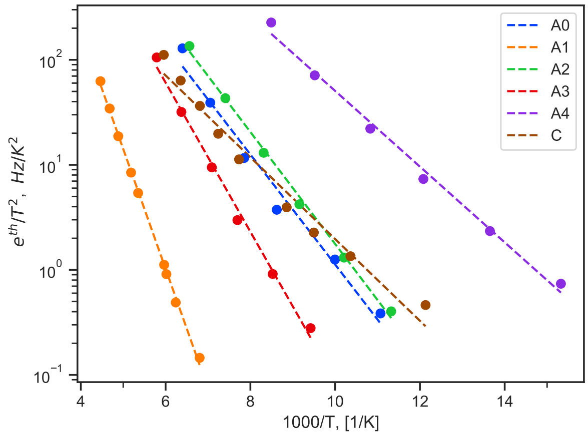

Figure 5.10.6: Arrhenius plot of inflection temperatures from C(T).

Both activation energy and capture cross section can be extracted from the Arrhenius analysis. An activation energy at $E = E_v + 0.1 \pm 0.04$eV is found in all samples apart from A1. Differing from A0,A2,A3 and A4, sample C is observed to have a σ one order of magnitude smaller at $\sim 10^{-17}\ cm^2$. The trap signature of A1 is found to differ significantly from the rest of the samples as it shows a different activation energy at $E_v + 0.22$eV and larger capture cross section of $\sim 10^{-15}\ cm^2$.

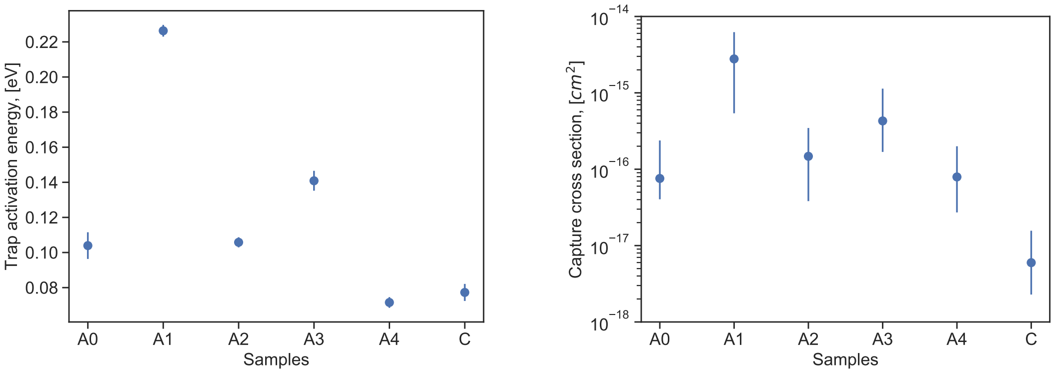

(a) Activation energy

(b) Capture cross section

Figure 5.10.7: Activation energy (a) and capture cross sections (b) are ascertained from Arrhenius analysis and by assuming $f_t = 2e^{th}$.

5.10.3 Change in trap signature over time

Samples A0,A3 and A4 were created several months prior to A1, A2 and C. They were measured shortly after being deposited and processed into mesa diodes. After being measured they were packaged in Al-foil and stored within a closed plastic bag. TAS measurements were conducted on these diodes after four months show a decrease in freeze out temperature, capture cross section and apparent activation energy for all samples. Although the decrease observed for σ in A3 is within the standard error, both A0 and A4 show capture cross sections lowered by approximately 1 order of magnitude. Furthermore, trap activation energies are also found to decrease. From these observations it appears that the defect chemistry of the E1 state observed in TAS changes with time. However, the physical process behind this is not possible to determine within the scope of this thesis.

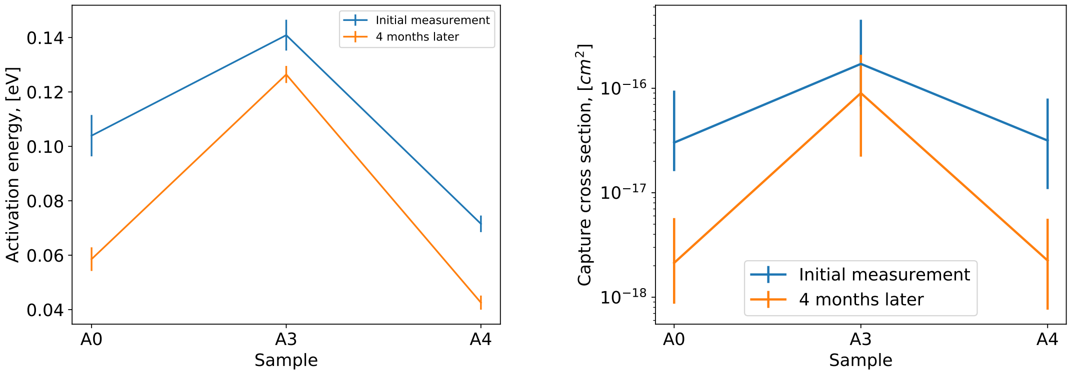

(a) Apparent activation energy

(b) σ.

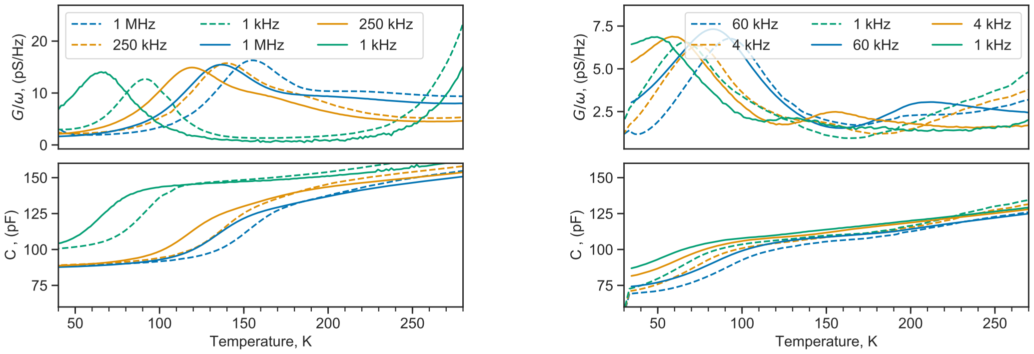

(c) C and G/ω for A0. The dotted line show the initial measurement.

(d) A3. The dotted line show the initial measurement. Not the difference in y-scale for G/ω compared to (c)

Figure 5.10.8: Evolution of apparent trap activation energy (a) and capture cross section (b). Note the decrease in freeze out temperature in A0 for all frequencies in (c). The change in freeze out temperature is not constant and the freeze out temperature increases as the the AC-frequencies decrease. Note also that in the case of A4 (d) a second inflection peak between 150 and 220K is clearly visible in the last measurement.

The measurement of A4 4 months after the initial measurement reveal the presence of another state, freezing out at high temperatures. This state is found to have an activation energy of $E_a = 0.097 \pm 0.007$ and a capture cross section of $\sigma(3.5 \pm 2e-19)$. Although the extrapolated activation energy is low, σ is more than one order of magnitude smaller than any other capture cross section observed in this work.

5.10.4 Summary and discussion

Throughout the thesis, no clear evidence has been found to accurately determine the relationships x_t/x_a or N_t/N_a. Both simulations and experimental results indicate that N_t/N_a is not possible to determine accurately from admittance measurements.

Further, determining x_a from CV measurements by utilizing the known doping concentration of Si is not possible, due to both the Debye length and instrumental accuracy. Thus, it is only possible to speculate about $N_t x_t / N_a x_a$. The inflection frequency f_t has been hence assumed to be described by $f_t = 0.5e^{th}$, in order to calculate values for E_a and σ and compare samples. Changing f_t with a constant has the effect of altering the y-intercept of the Arrhenius plot, which in turn is used to determine σ. Extrapolated values of σ is thus not expected to be precise.

Simulations show a increase in freeze out temperature with increasing σ, N_t and trap activation energy. Although two separate depletion regions are observed in Cu_2O for trap levels $E_t < E_v + 0.3$, this has little effect on the simulated freeze out temperatures. The effect of mismatch between the gold workfunction and electron affinity of Cu_2O, results in a depletion layer in Cu_2O in the simulations. This effect is expected to diminish in physical samples, due to the lack of quantum mechanical tunneling effects in simulations. Furthermore, simulations indicate that Cu_2O is fully depleted of free carriers after freeze out of the trap.

Apart from A1, all samples were found to have activation energies $E_a \leq 0.14$eV. The un-doped sample deposited from the ceramic sputtering target showed similar freeze out temperatues and activation energy, but with a capture cross section one order of magnitude lower than A0. The simulated values, employing σ and E_a extrapolated from experiments, predicts that the experimental freeze out temperatures of A0,A2,A3 and C are only comparable with simulations if N_t is low.

Values of $\Delta C / C_\infty$ is shown to differ little between the samples. If the assumption of $f_t = \frac{1}{2} e^{th}$ is valid, this indicates that the relation N_t / N_a is close to constant across the all samples. However, simulations indicate that 500nm thick Cu_2O films is fully depleted after freeze out. Change in depletion region is thus expected to be limited by the film thickness and is thus not expected to accurately reflect the relationship N_t / N_a. The near constant value of $\Delta C / C_\infty$ testify thus to a fully depleted Cu_2O layer after carrier freeze out. TAS measurements are thus unable to indicate trap concentrations in Cu_2O.

5.11 Trap identification

If A1 is excluded however, all activation energies reported from TAS is found at $E_v + 0.1 \pm 0.03eV$. Due to the small energy variation, it is speculated that it is the same state which is identified in these diodes. If capture cross section is assumed to be temperature independent, i.e. $E_\sigma = 0$, this activation energy corresponds to E1 from TDH measurements. Although the TDH results only indicate this state in A4 and A5, E1 is assumed to be compensated in the other samples. According to literature, this activation energy correlates with the N_O defect presented in table 2.6.2a. Additionally, the similar capture cross sections of E1 for A0,A2, A3 and A4 bear further witness that these energies refer to the same state. The lower σ found in sample C indicates that this state is less effective at capturing carriers when samples are deposited from a ceramic target. It is unknown why E1 is not observed in TAS measurements of A1, either as a shoulder or separate G/ω maximum.

Estimating the concentration of traps with acceptor energi for E1 from TDH measurements, reveals significantly different concentrations in the two samples where this state is observable. On the other hand, TAS yields no accurate estimate of N_t. SIMS measurements show nitrogen concentrations 3 times larger in A5 compared to A4, but this does not adequately describe the two order of magnitude increase in $p(T)$ at 150K. Such a trend is more reasonable if heavy Li doping simultaneously results in suppression of compensating states, speculated to be related to (Li-H) complexes.

Temperature dependent Hall measurements imply an activation energy at $E_v + 0.21 \pm 0.03$ eV, which corresponds well to the trap activation energy in A1 found from TAS. Although this energy is consistently observed in A0-A4, it is debatable whether it is observed in A5. Worth mentioning is the assumption of two acceptor states employed by the theoretical model used for fitting Arrhenius plots of the TDH data. The large uncertainties for the deep state observed in A5 at $E_v + 0.3 \pm 0.1$eV is likely a reflection of this. Literature report v_{Cu} to have a similar activation energy as E2, as described in table 2.6.2a. The observed variation of E2 energies further corresponds to the two states Bergum et.al. [11] attributed to v_{Cu} from TDH measurements of Cu_2O thin films.

The observed change in trap signature after a period of 4 months can be attributed to numerous mechanisms, but is ultimately unknown. Chemical change related to defects, for instance formation and dissociation of defect complexes is expected to contribute to signature changes. Formation and dissociation of copper vacancies and fixed donors is a model that has already been proposed for metastability issues related to series resistance, V_{oc} and J_{sc} [31] in Cu_2O. In this case, the possibility of hydrogen dissociating, migrating or forming complexes on different sites must also be included in the speculations.

6 Summary

The effect of Li doping in Cu_2O thin films deposited by magnetron sputtering has been investigated. Furthermore, films sputtered from a ceramic Cu_2O were optimized with respect to oxygen flow and compared to samples deposited from metallic Cu sputter targets. .

6.1 Conclusion

Optimization of oxygen flow for RF magnetron sputtering of a ceramic Cu_2O targets is found to influence the phase purity of Cu_2O films. Evidence of both Cu and CuO phases is found at low and high oxygen flow during deposition. Hall mobility, carrier concentration and resistivity of the thin films are also found to be strongly dependent on this optimization. Hence, control of oxygen flow during sputter deposition is of paramount importance. Furthermore, films deposited from a ceramic target is found to have lower mobility than films deposited by sputtering Cu-target while the carrier concentration appears to be similar. The un-doped films sputtered from the ceramic target were found to have significantly higher concentrations of certain impurities.

Li doping in the range of $10^{18} - 10^{21}\ cm^{-3}$ is achieved and found to influence hole concentrations. The lower doping concentration results in one order of magnitude reduction in hole concentrations, from $p(T = 300K) \sim 10^{15}$ to $10^{14}\ cm^{-3}$. Further doping is found to increase the observed hole concentration. For samples with [Li] $\geq 10^{20}\ cm^{-3}$, particular high carrier concentrations are observed. On the other hand, high concentrations of impurities are observed in all samples. Most notably the amphoteric $[H] \sim 10^{20} - 10^{21}\ cm^{-3}$, $N \sim 10^{18} - 10^{20}\ cm^{-3}$ and Al up to $10^{17} - 10^{18}\ cm^{-3}$. Impurities like Al and H are expected to compensate the hole concentration. It is speculated that the increase in hole concentration with increasing Li doping could be related to interaction of Li with the compensating impurity hydrogen.

Diodes have been fabricated with rectification between 2.1 and 5.8 orders of magnitude and ideality factors from 1.2 to 2.8 at 290K. Leakage current is found to vary among samples. CV measurements indicate that at room temperatures the Cu_2O/Si Schottky diode behaves as an abrupt p^+n. At temperatures <150K, the built in voltage indicates a fully depleted Cu_2O layer. Neither IV nor CV measurements where found to show dependency on Li doping.

TAS measurements identify an energy state at $E_v + 100 \pm 30meV$ with a capture cross section of $\sigma \sim 10^{-17} - 10^{-16}$ in all samples, expect for the lowest doped. This level is attributed to N_O and are also deduced from TDH measurements. Additional, a deeper level is identified at $E_v + 200 - 300$meV in all samples. A change in trap characteristic for the shallow state is observed from TAS after 4 months, with a measured reduction in both E_t and σ.

6.2 Further work

A more comprehensive study of changes in trap characteristics, including all samples being characterized with TAS, TDH and SIMS is expected to reveal more of the nature of the shallow acceptor state. Furthermore, deposition of Li doped samples from metallic targets utilizing purely RF sputter power, is expected to increase the ideality factor and current rectification. On the other hand, TAS measurements of a films with both Cu_2O and Cu phases could provide insight into the observed trap states, as such films are expected to have low $[v_{Cu}]$ without significant [Li] doping.

Thermal oxidation of Li doped Cu_2O thin films, with good atmospheric control, could provide more insight and understanding of the effect of Li doping. To investigate the effect of H impurities in these samples, varying the flow of H_2 would be ideal. Co-sputtering of Li doped Cu targets with the ceramic Cu_2O could further reveal new aspects of Li doping.

Simulations of temperature dependent Hall effect could reveal insight into the balance between deep donors and various acceptor states. As a start, simulating with one deep donor and two acceptor of various concentration and activation energy could help interpret hall measurements more accurately. If this is successful, a natural second step is the introduction of these states into the model for TAS simulations.

Bibliography

[1] V. Krey, G. Luderer, L. Clarke, and E. Kriegler, "Getting from here to there - energy technology transformation pathways in the EMF27 scenarios," *Clim. Change*, vol. 123, no. 3-4, pp. 369–382, 2014.

[2] Frankfurt School-UNEP Collaborating Centre for Climate & Sustainable Energy Finance, "Global Trends in Renewable Energy Investment 2018," *Bloom. New Energy Financ.*, pp. 1 – 60, 2018.

[3] F. Creutzig, P. Agoston, J. C. Goldschmidt, G. Luderer, G. Nemet, and R. C. Pietzcker, "The underestimated potential of solar energy to mitigate climate change," *Nat. Energy*, vol. 2, p. 17140, sep 2017.

[4] B. N. E. Finance, "New Energy Outlook 2018." Report, 2018.

[5] S. Philipps and W. Warmuth, "PHOTOVOLTAICS REPORT," 2019.

[6] F. Haase, C. Hollemann, S. Schäfer, A. Merkle, M. Rienäcker, J. Krügener, R. Brendel, and R. Peibst, "Laser contact openings for local poly-Si-metal contacts enabling 26.1%-efficient POLO-IBC solar cells," *Sol. Energy Mater. Sol. Cells*, vol. 186, no. March, pp. 184–193, 2018.

[7] "A decade of perovskite photovoltaics," *Nat. Energy*, vol. 4, pp. 1–1, jan 2019.

[8] R. Wang, M. Mujahid, Y. Duan, Z. K. Wang, J. Xue, and Y. Yang, "A Review of Perovskites Solar Cell Stability," *Adv. Funct. Mater.*, vol. 1808843, pp. 1–25, 2019.

[9] Y. L. Liu, Y. C. Liu, R. Mu, H. Yang, C. L. Shao, J. Y. Zhang, Y. M. Lu, D. Z. Shen, and X. W. Fan, "The structural and optical properties of Cu 2 O films electrodeposited on different substrates," *Semicond. Sci. Technol.*, vol. 20, no. 1, pp. 44–49, 2005.

[10] T. Minami, T. Miyata, K. Ihara, Y. Minamino, and S. Tsukada, "Effect of ZnO film deposition methods on the photovoltaic properties of ZnO-Cu2O heterojunction devices," *Thin Solid Films*, vol. 494, no. 1-2, pp. 47–52, 2006.

[11] K. Bergum, H. N. Riise, S. M. Gorantla, E. Monakhov, and B. G. Svensson, "Thin film Cu2O for solar cell applications," in *Conf. Rec. IEEE Photovolt. Spec. Conf.*, vol. 2016-Novem, pp. 2770–2773, 2016.

[12] A. D. Vos, "Detailed balance limit of the efficiency of tandem solar cells," *J. Phys. D. Appl. Phys.*, vol. 13, no. 5, pp. 839–846, 1980.

[13] A. Mittiga, E. Salza, F. Sarto, M. Tucci, and R. Vasanthi, "Heterojunction solar cell with 2% efficiency based on a Cu2O substrate," *Appl. Phys. Lett.*, 2006.

[14] M. Tadatsugu, N. Yuki, and M. Toshihiro, "Efficiency enhancement using a Zn 1-x Ge x -O thin film as an n-type window layer in Cu 2 O-based heterojunction solar cells," *Appl. Phys. Express*, vol. 9, no. 5, p. 52301, 2016.

[15] Y. S. Lee, D. Chua, R. E. Brandt, S. C. Siah, J. V. Li, J. P. Mailoa, S. W. Lee, R. G. Gordon, and T. Buonassisi, "Atomic layer deposited gallium oxide buffer layer enables 1.2 v open-circuit voltage in cuprous oxide solar cells," *Adv. Mater.*, vol. 26, no. 27, pp. 4704–4710, 2014.

[16] O. Porat and I. Riess, "Defect chemistry of Cu2-yO at elevated temperatures. Part II: Electrical conductivity, thermoelectric power and charged point defects," *Solid State Ionics*, vol. 81, no. 1-2, pp. 29–41, 1995.

[17] D. O. Scanlon, B. J. Morgan, and G. W. Watson, "Modeling the polaronic nature of p -type defects in Cu2 O: The failure of GGA and GGA+U," *J. Chem. Phys.*, vol. 131, no. 12, 2009.

[18] T. Minami, Y. Nishi, T. Miyata, and J. I. Nomoto, "High-efficiency oxide solar cells with ZnO/Cu2O heterojunction fabricated on thermally oxidized Cu2O sheets," *Appl. Phys. Express*, vol. 4, no. 6, pp. 2–5, 2011.

[19] L. Y. Isseroff and E. A. Carter, "Electronic structure of pure and doped cuprous oxide with copper vacancies: Suppression of trap states," *Chem. Mater.*, vol. 25, no. 3, pp. 253–265, 2013.

[20] B. Streetman, *Solid State Electronic Devices*. Pearson, 7 ed., 2016.

[21] R. J. D. Tilley, *Understanding Solids*. Wiley, 2 ed., 2013.

[22] T. Nordby, "Defects and Transport in Crystalline Materials," 2018.

[23] C. Kittel, *Introduction to Solid State Physics*. Wiley, 8 ed., 2004.

[24] A. Smets, K. Jäger, O. Isabella, R. van Swaaij, and M. Zeman, *Solar Energy: The Physics and Engineering of Photovoltaic Conversion, Technologies and Systems*. UIT Cambridge, 2016.

[25] J. Nelson, *The Physics of Solar Cells*. PUBLISHED BY IMPERIAL COLLEGE PRESS AND DISTRIBUTED BY WORLD SCIENTIFIC PUBLISHING CO., may 2003.

[26] M. Heinemann, B. Eifert, and C. Heiliger, "Band structure and phase stability of the copper oxides Cu2O, CuO, and Cu4O3," *Phys. Rev. B*, vol. 87, no. 11, p. 115111, 2013.

[27] P. Blood and J. W. Orton, *The electrical characterization of semiconductors: Majority carriers and electron states*. Academic press, 14 ed., 1992.

[28] S. Rühle, "Tabulated values of the Shockley-Queisser limit for single junction solar cells," *Sol. Energy*, vol. 130, pp. 139–147, 2016.

[29] W. Mönch, *Electronic Properties of Semiconductor Interfaces*, vol. 43 of *Springer Series in Surface Sciences*. Berlin, Heidelberg: Springer Berlin Heidelberg, 2004.

[30] B. K. Meyer, A. Polity, D. Reppin, M. Becker, P. Hering, P. J. Klar, T. Sander, C. Reindl, J. Benz, M. Eickhoff, C. Heiliger, M. Heinemann, J. Bläsing, A. Krost, S. Shokovets, C. Müller, and C. Ronning, "Binary copper oxide semiconductors: From materials towards devices," *Phys. Status Solidi*, vol. 249, no. 8, pp. 1487–1509, 2012.

[31] F. Biccari, "Defects and Doping in Cu₂O," *PhD Thesis*, no. 688774, p. 262, 2009.

[32] T. Kazimierczuk, D. Fröhlich, S. Scheel, H. Stolz, and M. Bayer, "Giant Rydberg excitons in the copper oxide Cu2O," *Nature*, vol. 514, pp. 343–347, oct 2014.

[33] F. K. Momma, "VESTA 3 for three-dimensional visualization of crystal, volumetric and morphology data," 2011.

[34] B. K. Meyer, A. Polity, D. Reppin, M. Becker, P. Hering, B. Kramm, P. J. Klar, T. Sander, C. Reindl, C. Heiliger, M. Heinemann, C. Müller, and C. Ronning, "The Physics of Copper Oxide (Cu2O)," in *Semicond. Semimetals*, ch. 6, pp. 201–226, 88 ed., 2013.

[35] A. S. Zoolfakar, R. A. Rani, A. J. Morfa, A. P. O'Mullane, and K. Kalantar-Zadeh, "Nanostructured copper oxide semiconductors: A perspective on materials, synthesis methods and applications," *J. Mater. Chem. C*, vol. 2, no. 27, pp. 5247–5270, 2014.

[36] G. K. Paul, Y. Nawa, H. Sato, T. Sakurai, and K. Akimoto, "Defects in Cu2 O studied by deep level transient spectroscopy," *Appl. Phys. Lett.*, vol. 88, no. 14, pp. 2–5, 2006.

[37] H. Raebiger, S. Lany, and A. Zunger, "Origins of the p-type nature and cation deficiency in Cu2 O and related materials," *Phys. Rev. B - Condens. Matter Mater. Phys.*, vol. 76, no. 4, pp. 1–5, 2007.

[38] R.-f. M. Sputtering, S. Ishizuka, T. Maruyama, K. Akimoto, Y. S. Jung, H. W. Choi, K. H. Kim, C. O. Cu, N. Tabuchi, and H. Matsumura, "Nitrogen Doping into Cu 2 O Thin Films Deposited by Reactive Radio-Frequency Magnetron Sputtering," *Jpn. J. Appl. Phys.*, vol. 40, pp. 2765–2768, 2001.

[39] C. G. V. D. Walle and J. Neugebauer, "Universal alignment of hydrogen levels in semiconductors, insulators and solutions," *Nature*, vol. 423, no. June, pp. 626–628, 2003.

[40] D. O. Scanlon and G. W. Watson, "Uncovering the complex behavior of hydrogen in Cu2O," *Phys. Rev. Lett.*, vol. 106, no. 18, pp. 1–4, 2011.

[41] S. Ishizuka, S. Kato, Y. Okamoto, and K. Akimoto, "Hydrogen treatment for polycrystalline nitrogen-doped Cu2O thin film," *J. Cryst. Growth*, vol. 237-239, no. 1-4 I, pp. 616–620, 2002.

[42] N. Tabuchi and H. Matsumura, "Control of Carrier Concentration in Thin Cuprous Oxide Cu ₂ O Films by Atomic Hydrogen," *Jpn. J. Appl. Phys.*, vol. 41, no. Part 1, No. 8, pp. 5060–5063, 2002.

[43] K. P. Hering, C. Kandzia, J. Benz, B. G. Kramm, M. Eickhoff, and P. J. Klar, "Hydrogen induced mobility enhancement in RF sputtered Cu2O thin films," *J. Appl. Phys.*, vol. 120, no. 18, 2016.

[44] M. Zouaghi, "Near Infrared Optical and Photoelectric Properties (II)," *Phys. Status Solidi*, vol. 11, no. 11, p. 219, 1972.

[45] N. Kikuchi, K. Tonooka, and E. Kusano, "Mechanisms of carrier generation and transport in Ni-doped Cu2O," *Vacuum*, vol. 80, no. 7 SPEC. ISS., pp. 756–760, 2006.

[46] C. Malerba, F. Biccari, C. Leonor Azanza Ricardo, M. D'Incau, P. Scardi, and A. Mittiga, "Absorption coefficient of bulk and thin film Cu2O," *Sol. Energy Mater. Sol. Cells*, vol. 95, no. 10, pp. 2848–2854, 2011.

[47] T. O. M. Tiedje, E. L. I. Yablonovitch, G. D. G. Cody, and B. G. B. B. G. Brooks, "Limiting Efficiency of Silicon," *IEEE Trans. Electron Devices*, vol. 31, no. 5, pp. 711–716, 1984.

[48] A. A. Istratov, C. Flink, H. Hieslmair, S. A. McHugo, and E. R. Weber, "Diffusion, solubility and gettering of copper in silicon," *Mater. Sci. Eng. B Solid-State Mater. Adv. Technol.*, vol. 72, no. 2, pp. 99–104, 2000.

[49] Ø. Nordseth, R. Kumar, K. Bergum, L. Fara, C. Dumitru, D. Craciunescu, F. Dragan, I. Chilibon, E. Monakhov, S. Foss, and B. Svensson, "Metal Oxide Thin-Film Heterojunctions for Photovoltaic Applications," *Materials (Basel).*, vol. 11, no. 12, p. 2593, 2018.

[50] M. Izaki, T. Shinagawa, K. T. Mizuno, Y. Ida, M. Inaba, and A. Tasaka, "Electrochemically constructed p-Cu2O/n-ZnO heterojunction diode for photovoltaic device," *J. Phys. D. Appl. Phys.*, vol. 40, no. 11, pp. 3326–3329, 2007.

[51] N. G. Elfadill, M. R. Hashim, K. M. Chahrour, and S. A. Mohammed, "Preparation of p-type Na-doped Cu2O by electrodeposition for a p-n homojunction thin film solar cell," *Semicond. Sci. Technol.*, vol. 31, no. 6, 2016.

[52] S. A. Campbell, *Fabrication Engineering at the Micro- and Nanoscale*. Oxford University Press, fourth edi ed., 2013.

[53] H. Frey and H. R. Khan, *Handbook of Thin-Film Technology*. 2015.

[54] M. Birkholz, *Principles of X-ray Diffraction*. Weinheim, FRG: Wiley-VCH Verlag GmbH & Co. KGaA, may 2006.

[55] Y. Leng, "X-Ray Diffraction Methods," in *Mater. Charact.*, pp. 45–77, Chichester, UK: John Wiley & Sons, Ltd.

[56] Y. Leng, *Related Titles Characterization of Surfaces and Nanostructures Basic Concepts of X-Ray Diffraction Characterization of Solid Materials and Heterogeneous Catalysts Advanced Characterization Techniques for Thin Film Solar Cells Characterization Techniques f*. 2013.

[57] L. C. Kimerling, "Influence of deep traps on the measurement of free-carrier distributions in semiconductors by junction capacitance techniques," *J. Appl. Phys.*, vol. 45, no. 4, pp. 1839–1845, 1974.

[58] D. K. Schroeder, *Semiconductor Material and Device Characterization*. 3rd ed ed., 2006.

[59] C. K. Maiti, *Computer Aided Design of Micro- and Nanoelectronic Devices*. WORLD SCIENTIFIC, jan 2017.

[60] S. International, *Silvaco Atlas User's Manual: Device Simulation Software*.

[61] Y. Takiguchi and S. Miyajima, "Device simulation of cuprous oxide heterojunction solar cells," *Jpn. J. Appl. Phys.*, vol. 54, no. 11, 2015.

[62] Y. Takiguchi, Y. Takei, K. Nakada, and S. Miyajima, "Fabrication and characterization of sputtered Cu2O:N/c-Si heterojunction diode," *Appl. Phys. Lett.*, vol. 111, no. 9, pp. 2–6, 2017.

[63] P. F. Lindberg, H. N. Riise, K. Bergum, B. G. Svensson, and E. V. Monakhov, "Electronic properties of Au/Cu2O/n-type Si heterojunction for energy conversion," *2017 IEEE 44th Photovolt. Spec. Conf. PVSC 2017*, pp. 1–4, 2018.

Appendices

A SIMS results for H, N, and Al

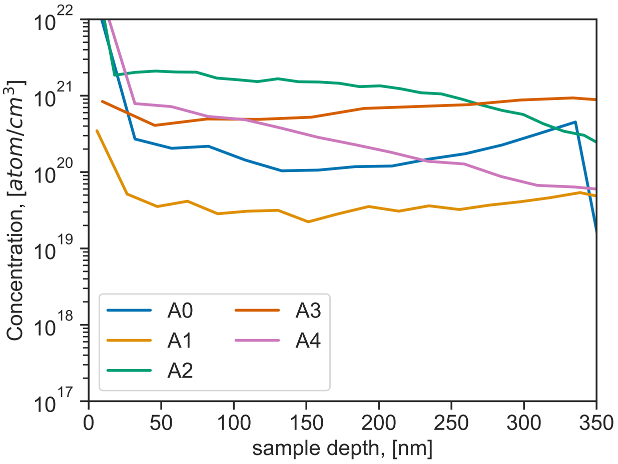

Figure A.0.1: Hydrogen concentration. The measurement of A5 is several orders of magnitude higher than the other results and is categorized as an unreliable result

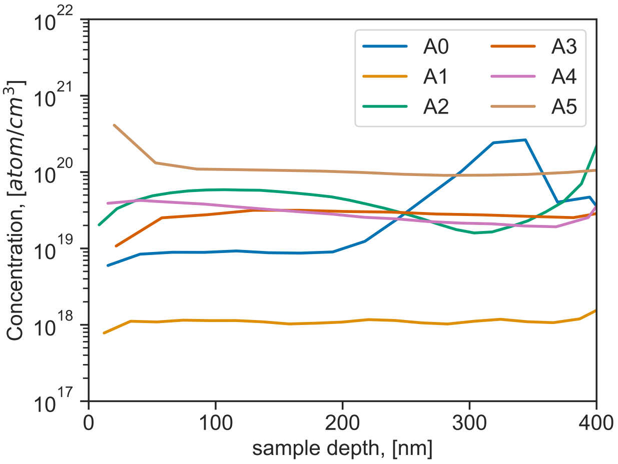

Figure A.0.2: Nitrogen concentration in A0-A5.

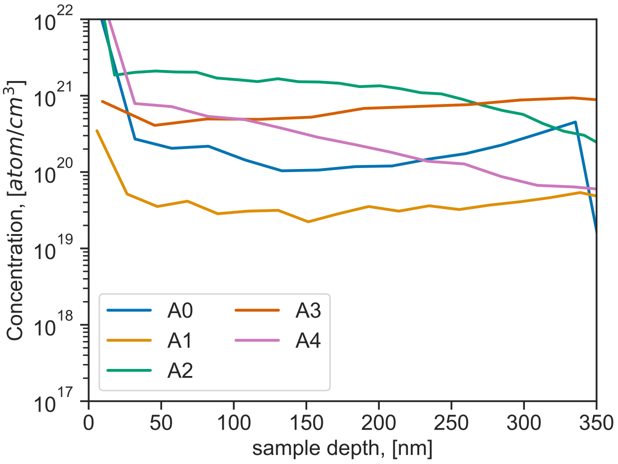

Figure A.0.3: Aluminium concentration in A0-A5.

B CV for Au:n-Si Schottky diode

Figure B.0.1 show both C(V) and Mott-Schottky plots for the Au/Si Schottky diode. Both $C(V)$ and $C^{-2}(V)$ is shown to vary a little with temperature in reverse bias, with near zero change in the slope $C^{-2}(V)$.

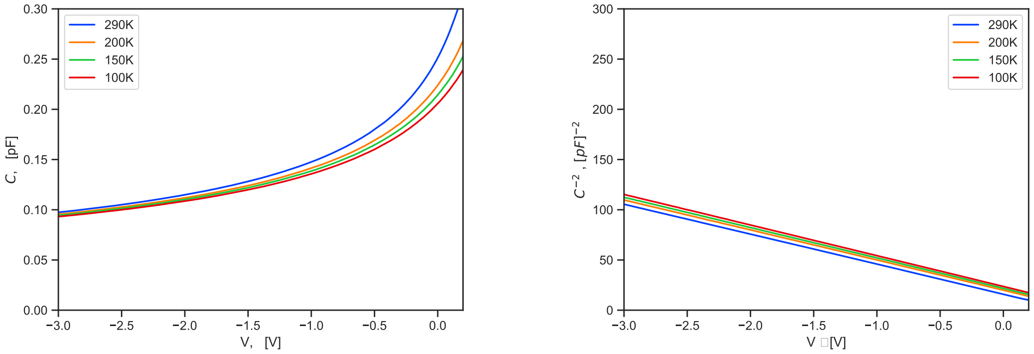

(a)

(b)

Figure B.0.1: C(V)(a) and Mott-Schottky plot (b) for Au:n-Si Schottky diode.

C Capacitance measurements at low temperatures

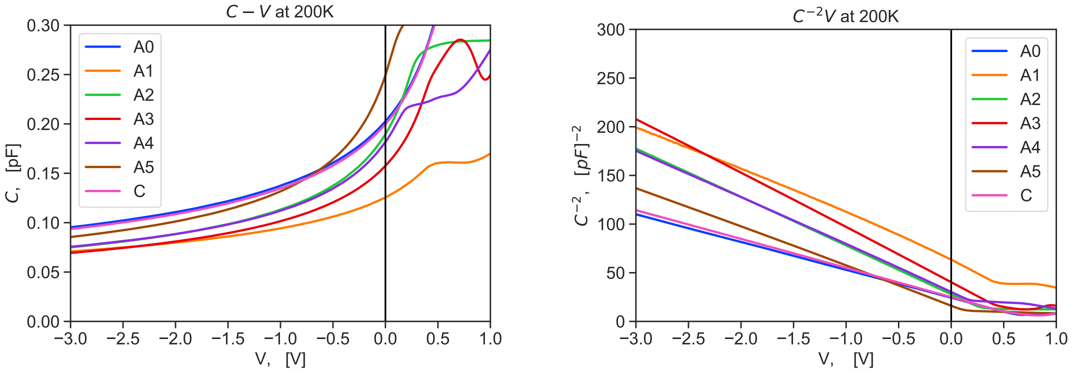

(a) CV .

(b) $C^{-2}(V)$

Figure C.0.1: (a) $C(V)$ and (b) $C^{-2}(V)$ at 200K.

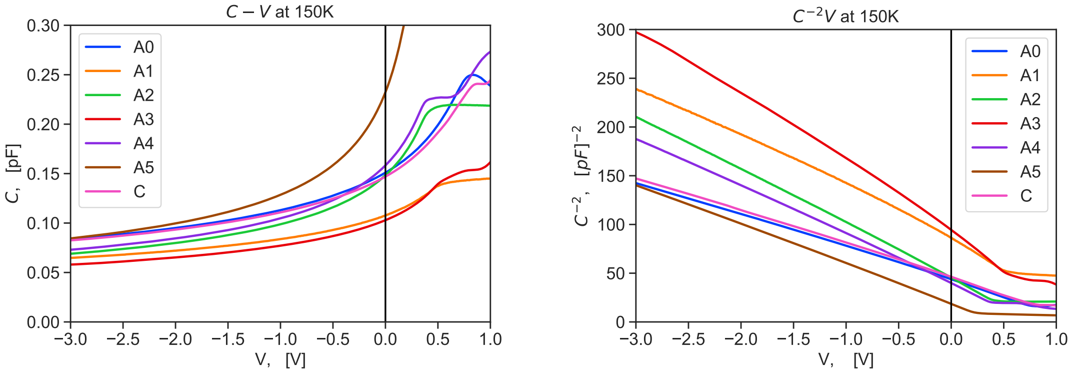

(a) CV at 150K.

(b) $C^{-2}(V)$ at 150K.

Figure C.0.2: (a) $C(V)$ and (b) $C^{-2}(V)$ at 150K.

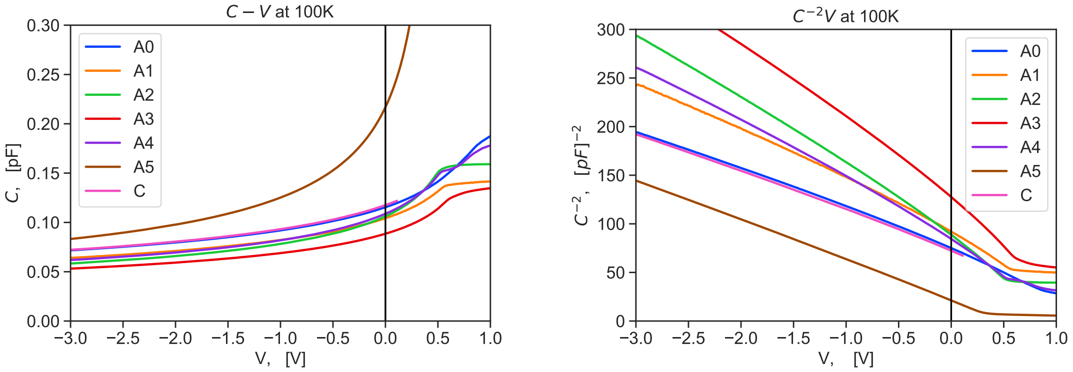

(a) CV at 100K.

(b) $C^{-2}(V)$ at 100K.

Figure C.0.3: (a) $C(V)$ and (b) $C^{-2}(V)$ at 100K.

D TAS measurements

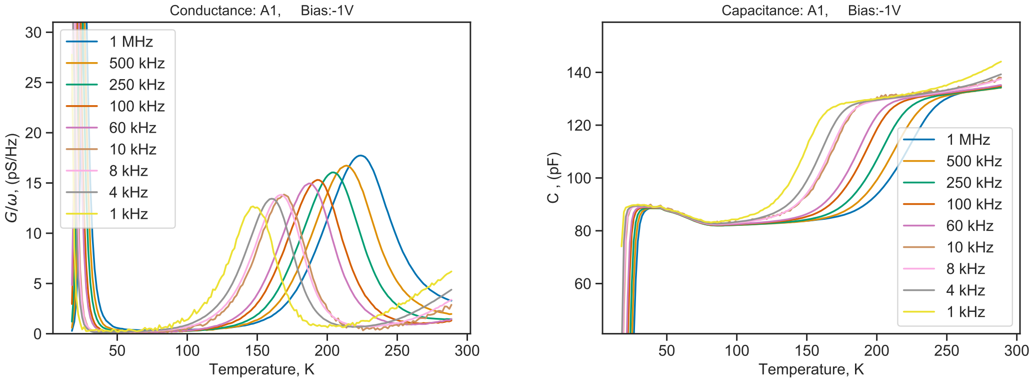

(a) G/ω

(b) Capacitance v T

Figure D.0.1: TAS results for A1.

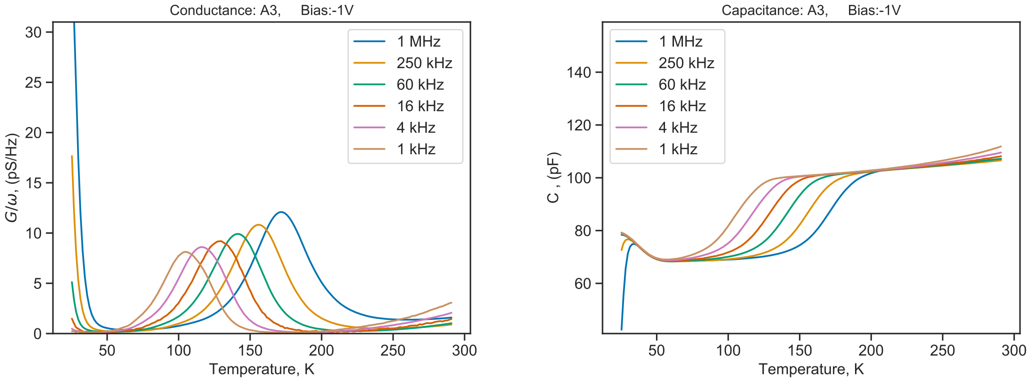

(a) G/ω

(b) Capacitance v T

Figure D.0.2: TAS results for A3.

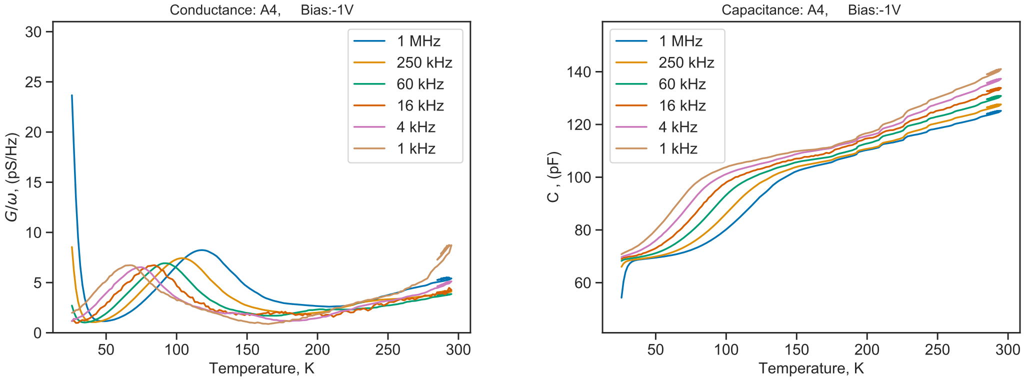

(a) G/ω

(b) Capacitance v T

Figure D.0.3: TAS results for A4.

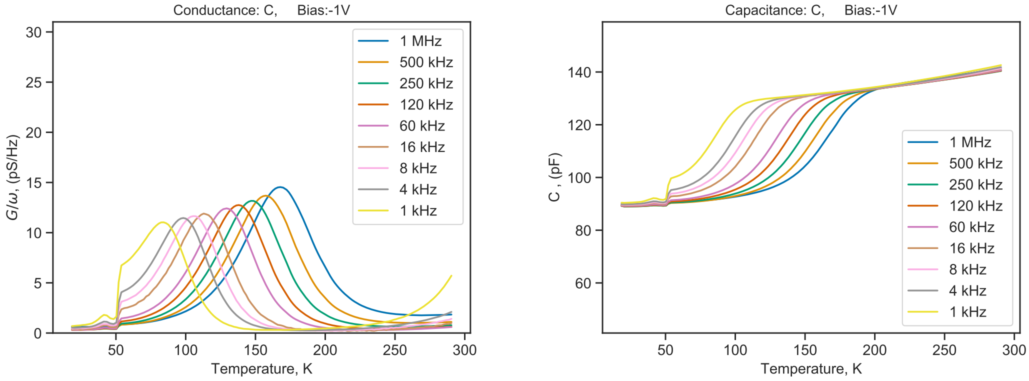

(a) G/ω

(b) Capacitance v T

Figure D.0.4: TAS results for C.

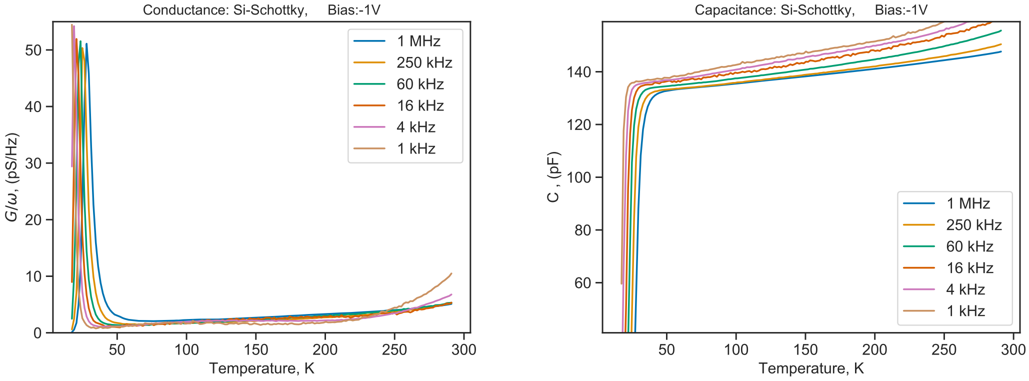

(a) G/ω for Au/Si Schottky diode

(b) Capacitance v T for Au/Si Schottky diode

Figure D.0.5: TAS results for the Au/Si Schottky diode.

E Silvaco Code

```
loop steps =150
stmt T = 200:-1
go atlas

set temp = $T
set Cu2O_dop=1e12
set trpElev =0.1
set donDens = 1e19
set sigma_p = 1e-16
set Cu2O_thick=0.5
set Si_thick = 10
###################  MESH  ###################

mesh
x.m loc=0       s=1
x.m loc=1       s=1

y.m loc = 0                                    s=0.01
y.m loc = $Cu2O_thick *0.5                     s=0.001
y.m loc = $Cu2O_thick                          s=0.001
y.m loc = $Cu2O_thick*2                        s=0.01
y.m loc = $Cu2O_thick*5                        s=0.1
y.m loc = $Cu2O_thick*10                       s=1
y.m loc = $Si_thick +$Cu2O_thick               s=1
############### Regions + el.trode      ####################
region num=1 user.material=Cu2O y.min = 0.0            y.max  =
    $Cu2O_thick
region num=2 material=Silicon   y.min= $Cu2O_thick      y.max =
    $Cu2O_thick + $Si_thick

elec num=1 name=anode           top
elec num=2 name=cathode         bottom
################## Material specs  #####################
material mat=Cu2O user.group=semiconductor user.default=ZnO EG300=2.1
    PERMITTIVITY=7.6 AFFINITY=3.2 MUN=200 MUP=100 NC300=2.43e19 NV300
    =1.34e19 taup0=1e-9 taun0=1e-9 index.file=Cu2o2.nk
```

```
material mat=Silicon user.group=semiconductor affinity = 4.05 user.
   default=Silicon

doping region=1 p.type concentration= $Cu2O_dop         uniform
   direction=y
doping region=2 n.type concentration=1e15               uniform
   direction=y

TRAP region=1 ACCEPTOR E.LEVEL=2.1-$trpElev DENSITY=$donDens DEGEN=20
   SIGN = $sigma_p SIGP = $sigma_p

contact  name=anode workfun=5.1
###################### Models ########################
models region=1         SRH
models region=2         AUGER

output con.band val.band opt.int recomb u.srh u.auger u.radiative band.
   param
models print temperature= $temp incomplete bgn fldmob TRAP.AUGER TRAP.
   COULOMBIC
method newton trap
############### TAS     ###################
solve init
save outf = "Ev+$trpElev Nt_$donDens sigma_ $sigma_p dop_$Cu2O_dop
   T_$temp.str"

solve VANODE = 0
solve VANODE = -0.1
solve VANODE = -0.2
solve VANODE = -0.3
solve VANODE = -0.4
solve VANODE = -0.5
solve VANODE = -0.6
solve VANODE = -0.7
solve VANODE = -0.8
solve VANODE = -0.9
solve VANODE = -1.0

log outf = "Ev+$trpElev Nt_$donDens sigma_$sigma_p dop_$Cu2O_dop T_$temp
   .log"

solve VANODE= -1.0 name = ANODE AC FREQ = 1.0e3 FSTEP = 4 MULT.F NFSTEPS
   =9

log off
l.end
quit
```